The Alliance of Laboratories in Europe for Education, Research and Technology

ALERT Doctoral School 2025

The Role of Geomechanics in the Energy Transition

Editors:

Anne-Catherine Dieudonné

Martin Lesueur

Jean-Michel Pereira

Hadrien Rattez

Manolis Veveakis

Preface

This volume emerges from the ALERT Geomaterials 2025 doctoral school which focuses on the role of geomechanics for the energy transition.

Geomechanics provides the quantitative, key framework to model ground behavior under changing mechanical loads and multiphysics. Its insights are essential to scaling low-carbon technologies without compromising safety, reliability, or cost.

The aim of the volume is to establish a link between fundamentals and practice across rapidly evolving low-carbon technologies. Chapters span offshore foundations, subsurface storage, geostructures, and adjacent applications. Multiphysics couplings provide a common language across these topics. Methods range from laboratory experiments and field measurements to theoretical modeling and numerical simulations.

Although each chapter stands on its own, the collection forms a continuous path. The intended readers are doctoral candidates, researchers, and practicing engineers.

As always, the PDF of this book can be downloaded free of charge from the ALERT Geomaterials website. ALERT Geomaterials thanks all contributors for the time, materials, and effort invested in crafting this volume.

Ioannis Stefanou
Director of ALERT Geomaterials
ENSTA — IP Paris

Contents

Foreword

The contributions assembled in this volume stem from the lectures delivered at the 2025 ALERT Doctoral School, devoted to *The Role of Geomechanics in the Energy Transition*.

The 2025 edition of the school addresses a timely and critical theme: how the fundamental principles of geomechanics underpin the successful deployment of energy technologies and subsurface solutions central to the global energy transition. This discussion takes place against the backdrop of pressing societal challenges: the combined effects of climate change, environmental pollution, and population growth are reshaping our demand for energy, while waste management and the reduction of greenhouse gas emissions have become urgent priorities. At the same time, the expansion of megacities and the increasing exposure to natural hazards require resilient and sustainable infrastructure.

As illustrated in Figure 1, traditional fossil-based energy sources such as oil, gas, coal, and nuclear have finite lifespans, with sustainability estimates ranging from only a few decades to two centuries. In contrast, renewable sources such as solar, wind, and geothermal hold the potential to meet global annual energy demand—provided that the outstanding scientific and technical challenges can be resolved to allow for efficient production, storage, and transport.

Traditionally, subsurface engineering has been associated with hydrocarbon production and classical geotechnical practice. Today, however, new applications such as shallow and deep geothermal energy, offshore wind energy, nuclear waste disposal, and CO_2 and hydrogen storage rely on the subsurface as a secure and controlled environment. These technologies present a different set of challenges, often involving extreme conditions of pressure, temperature, chemical reactivity, or long timescales. Understanding their impact on the mechanical response of geomaterials is crucial for ensuring performance, safety, and sustainability.

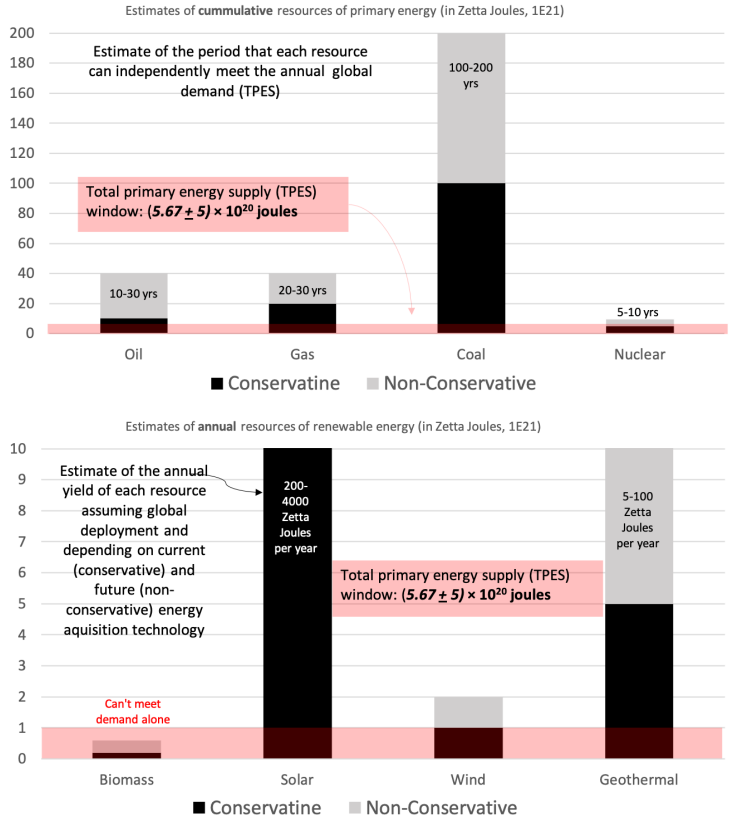

Figure 1: Estimates of the sustainability of fossil fuel (left) and renewable (right) forms of energy[1].

The learning objectives of the school are threefold. First, to present the state of key energy technologies, situating their contribution to the energy transition within broader historical and societal developments. Second, to clarify the specific geomechanical principles and challenges associated with each technology, including issues of multiphysics interactions, scaling, and uncertainty. Third, to provide participants with conceptual and methodological tools–both numerical and experimental–for modeling these complex problems across multiple scales and timespans.

[1]Turner, G. M. (2008). A comparison of The Limits to Growth with 30 years of reality. Global environmental change, 18(3), 397-411.

Robins, J. C., Kolker, A., Flores-Espino, F., Pettitt, W., Schmidt, B., Beckers, K., Pauling, H., Anderson, B. (2021). 2021 U.S. geothermal power production and district heating market report. National Renewable Energy Laboratory.

Center for Sustainable Systems, University of Michigan (2024). Geothermal Energy Factsheet. Pub. No. CSS10-10.

The design of the school reflects this vision. Each session combined a technology-focused introduction given by a domain expert with lectures emphasizing the geomechanical aspects of that technology. Themes common across applications–multiphysics couplings, scaling issues, and data uncertainties–were integrated throughout, enabling participants to build a coherent foundation for addressing the challenges of the energy transition.

This volume collects the core contributions from the school. Together, they provide postgraduate students and researchers with a consolidated view of how geomechanics supports safe, reliable, and sustainable energy solutions. Beyond technical insights, the school sought to highlight the societal relevance of geomechanics: in mitigating risks to urban areas and natural environments, in ensuring the sustainability of energy resources, and in contributing to the urgent global need for decarbonization.

We hope that these lecture notes will serve both as a reference on the state of the art in geomechanics for energy and as a source of inspiration for future research at the interface of scientific excellence and societal impact.

Anne-Catherine Dieudonné (Delft University of Technology)
Martin Lesueur (Delft University of Technology)
Jean-Michel Pereira (Ecole Nationale des Ponts et Chaussées)
Hadrien Rattez (Université Catholique de Louvain)
Manolis Veveakis (Duke University)

Geotechnical challenges for offshore wind turbine foundations

Benjamin Cerfontaine, Jamie Crispin, Susan Gourvenec

University of Southampton

Offshore wind energy must scale rapidly to meet global climate goals, presenting significant geotechnical challenges. This chapter explores how current foundation and anchor design practices—largely inherited from the oil and gas sector—are insufficient for the scale, pace, and complexity of offshore wind developments. Key issues include sparse and uncertain site data, complex cyclic loading, installation constraints, and long-term soil behaviour. This chapter sets the scene of the offshore wind context, and the resulting geotechnical challenges. These highlight the need to move beyond conservative drained/undrained assumptions and practice inherited from the oil and gas industry. A better understanding of underlying mechanisms will unlock innovation in the geotechnical practice, by relying on fundamental soil mechanics and physics-based approaches and design methods. In particular, this chapter emphasises the importance of: integrating geophysical and geotechnical data, developing silent installation methods, better understanding the cyclic behaviour of foundations and the multiphysical interactions for power cables, developing efficient surrogate models for design purposes and accounting for loading of foundations over their entire lifetime.

1 Introduction

1.1 Offshore wind context

Installed offshore wind power capacity must reach 2,000GW by 2050 to meet the objectives of the Paris Agreement [IRE21]. This requires a twentyfold increase of the current capacity (83GW), which only represents 1% of the total installed power worldwide, and an acceleration of the rate of installation of new turbines (Figure 1). This acceleration and upscaling is incompatible with current design and installation practice, and require innovation and evolution to meet the climate change challenges. So far, Europe and China are at the forefront of those developments, but other markets are opening up worldwide, such as the US and Japan.

Offshore wind turbines offer the advantages of stronger winds, a higher capacity factor and more available space when compared to onshore wind turbines. However, the harsh offshore environment makes their installation and maintenance more complex. The first 450kW and 35m diameter offshore wind turbine (OWT) was installed in 1991 in 4m water depth in the Danish North Sea, and founded on concrete gravity bases. Since then, the power, size and water depth of installed wind OWT have continuously increased (Figure 1). Hornsea 2 (UK), commissioned in 2022, is currently the largest wind farm worldwide (1.32GW), with 168 8MW OWT with 167m rotor

diameter installed at 30-40m water depth over an area of 400km^2. The Seagreen wind farm, commissioned one year later, used 10MW OWT in up to 59m water depth, and 236m rotor diameter 14MW wind OWT are currently produced.

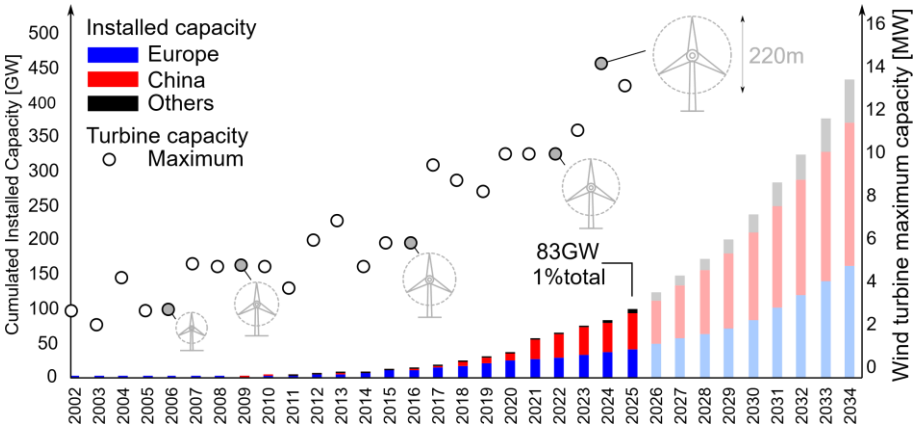

Figure 1: Evolution of the installed offshore wind capacity and maximum capacity of the installed wind turbine on any year.

1.2 Structures and Foundations

Most OWT are supported by bottom-fixed substructures, which maintain the OWT stability over their lifetime. Concrete gravity-based structured and foundations have been used in shallow waters (up to 30m), but monopiles, large steel tubular piles embedded into the seabed are currently the most installed substructure type. Beyond 60m water depths, jacket structures, steel lattice frameworks with multiple legs, become more economical. In even deeper waters, bottom-fixed structures are not viable and floating OWT are required. These are composed of a floater secured by mooring lines anchored into the seabed [CER23a]. Commercial floating wind farms only represent 0.2% of the currently installed capacity, but the potential for floating wind farms is huge, as 70% of the technical offshore potential in the EU/EEA is in water depth larger than 100m. The shallowest waters with a high potential have already been developed or are used by other activities [PUT23].

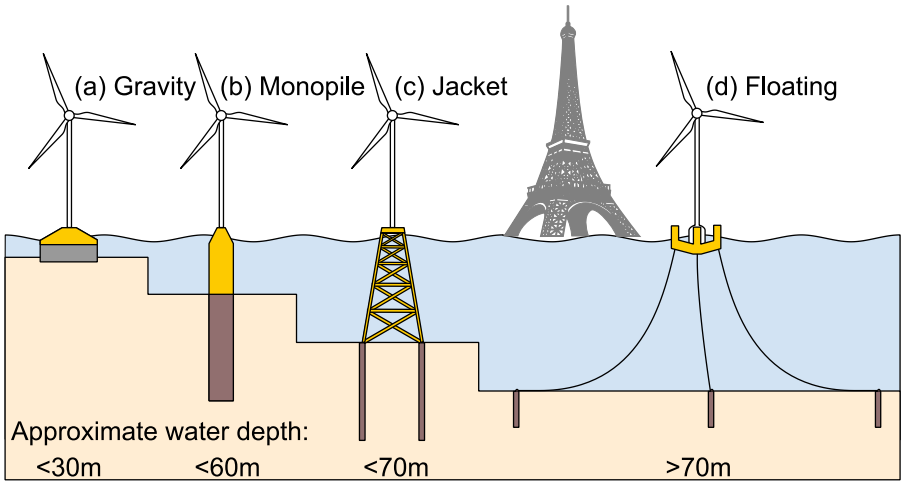

Figure 2: Main types of substructures used to support OWT.

The design of bottom-fixed structures and their foundations is heavily influenced by serviceability conditions, where the permanent tilting of the wind turbine over its lifetime must be limited to low values (e.g. 0.5° in early design) and the natural frequency of the turbine-structure-foundation must remain outside of the rotor rotation and wave frequencies [ARA17]. In particular, this has resulted in low slenderness (length/diameter) ratios for monopile foundations, which has challenged traditional pile design methods originally intended for slender piles. Conversely, the design of anchors for floating OWT is dominated by the ultimate limit state, because the flexibility of most mooring lines is such that any displacement of the anchor does not really affect the floater stability. In both cases, the foundations/anchors can be classified as a function of how they resist the load applied to them and how they are installed. The most relevant loads for bottom-fixed foundations are lateral and moment loads due to wind and waves, with the addition of self-weight vertical compression. Anchor loading is dominated by lateral and inclined loading due to tension in the mooring lines.

Anchors and foundations resist loads applied to them by mobilising soil strength at the soil-foundation interface or by mobilising a large volume of material (Figure 3). For instance, three anchor types can be identified: gravity, piles and plates [CER23a]. Their efficiency, defined as the ratio of the foundation resistance to the amount of material necessary for its construction, is the lowest for gravity and the highest for plate foundations. The same type of classification can be applied to foundations for bottom-fixed structures. Similarly, installation methods can be classified in three categories (Figure 4), which require the foundation self-weight, an external mechanical load, either dynamic or static, or hydro-mechanical mechanisms such as suction to install the foundation to the desired depth. Different types of foundations can be combined together and installed in different ways. For instance, a pile can be installed by suction or driving, but the selected installation method will affect their maximum dimensions. The selection of a foundation type and installation methods depend on the geological and geotechnical conditions, but also on logistical criteria, such as:

a) The existing chain of supply and capacity to pre-fabricate foundations at scale onshore. Steel monopiles are the most common foundations, which can reach up to 10m in diameter, are tens of meters long and weigh up to 1,900t. The pile type anchors for the first floating wind farm Hywind Scotland were 5m, in diameter and 16m in length. The gravity-based foundations for the Fécamp wind farm had a 31m diameter base, a height of up to 54m and weigh approximately 5,000t.
b) The reliability and rapidity of the installation method, crane capacity and availability of installation vessels which can cost hundreds of thousands of dollars per day. Pile driving is the most favoured method, while suction installation has also gained some traction recently (e.g. Seagreen wind farm). Drag and suction anchors are also used in addition to driven piles to secure floating structures.

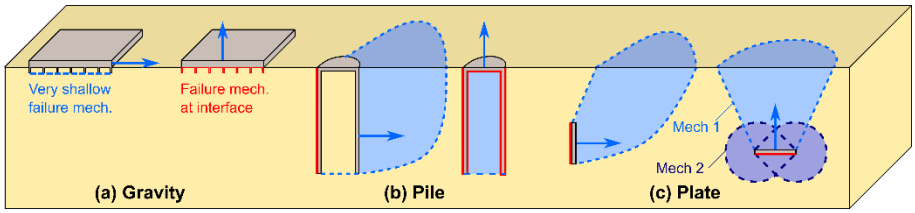

Figure 3: Summary of the different types of anchors, showing the mobilisation of interface strength and the volume of soil they mobilise at failure [CER23a].

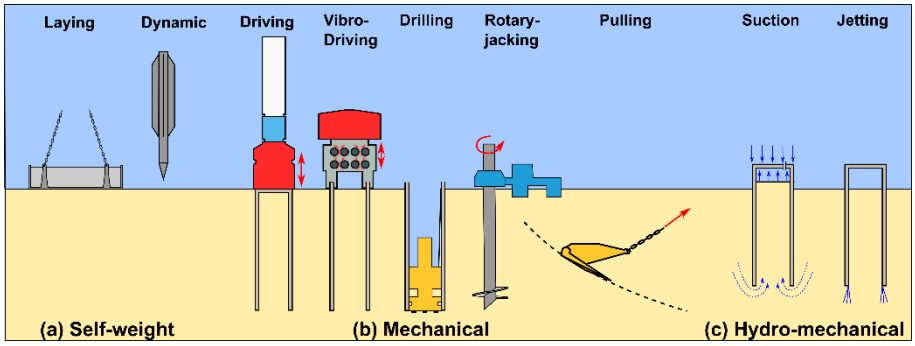

Figure 4: Foundation installation methods [TAI24].

1.3 Geotechnical challenges

The overarching goal of the offshore wind industry is to deliver bigger operational turbines faster and at lower cost to achieve the net-zero objectives. This translates into multiple geotechnical challenges at all stages of the development of offshore wind farms, as summarised in Figure 5. The design of offshore renewable infrastructures still relies on the more established oil and gas practice, especially for floating OWT. The design practice is often based on conservative empirical methods, which consider only drained and undrained scenarios, while partial drainage may occur in many

applications. However, the urgency of delivering clean energy, the much higher number of structures to be installed and the reduced consequences of failure of a wind turbine create a lot of room for innovation and evolution of the practice. Geotechnical challenges can be separated into two categories: a) knowledge and b) design challenges, although improvement in knowledge often leads to an improved design methodology.

2 Knowledge challenges

Knowledge challenges encompass all physical mechanisms and techniques involved in modelling geotechnical behaviours that are not well understood. These can arise because of the OWT specificities, such as the evolution of the turbine-soil stiffness, or because not enough data is available for situations that were rare in the oil and gas industry where much of our existing offshore geotechnically knowledge was obtained.

2.1 Site investigation

The site investigation comprises geophysical surveys, in-situ tests, borehole drilling and laboratory element tests of retrieved samples. These operations are particularly complex and costly, as they all take place in a harsh offshore environment and must be undertaken by specialised vessels. Advanced foundation design requires more and more data to quantify soil strength and stiffness through DSS (Direct Simple Shear) or triaxial tests, as well as how these vary under different cyclic load paths. However, only a limited number of tests can be undertaken due to their cost. It is usual to undertake one in-situ cone penetration test (CPT) per OWT location. Boreholes are required to retrieve samples for laboratory testing, the number of which depends on the complexity of geology and foundation or anchor type intended, and can range from one at each turbine location to one in 10 [SUT22]. The diameter of a CPT is between 36-44mm and the diameter of retrieved borehole samples is around 70mm, which is small when compared with the diameter of monopiles (e.g. 10m) and the scale of the wind farm (several hundred km^2). In addition to site characterisation for foundations and anchors, seabed properties between turbines for inter-array cables, and beyond the wind farm to shore are required. Cable investigations target shallower depth (typically < 5 m), but are required over long distances, often several hundred kilometres. Spacing of geotechnical testing can be between 1 km and 10 km depending on complexity and variability of the seabed, indicated by the geophysical survey. Overall, there are large uncertainties on the properties that can be used for design and their spatial variability. In addition, the overall duration of various stages of site investigation can take over several years, with often long lead times due to limited availability of specialised vessels or onshore lab facilities to test samples. Fortunately, some strategies already exist to alleviate the sparsity and time issues.

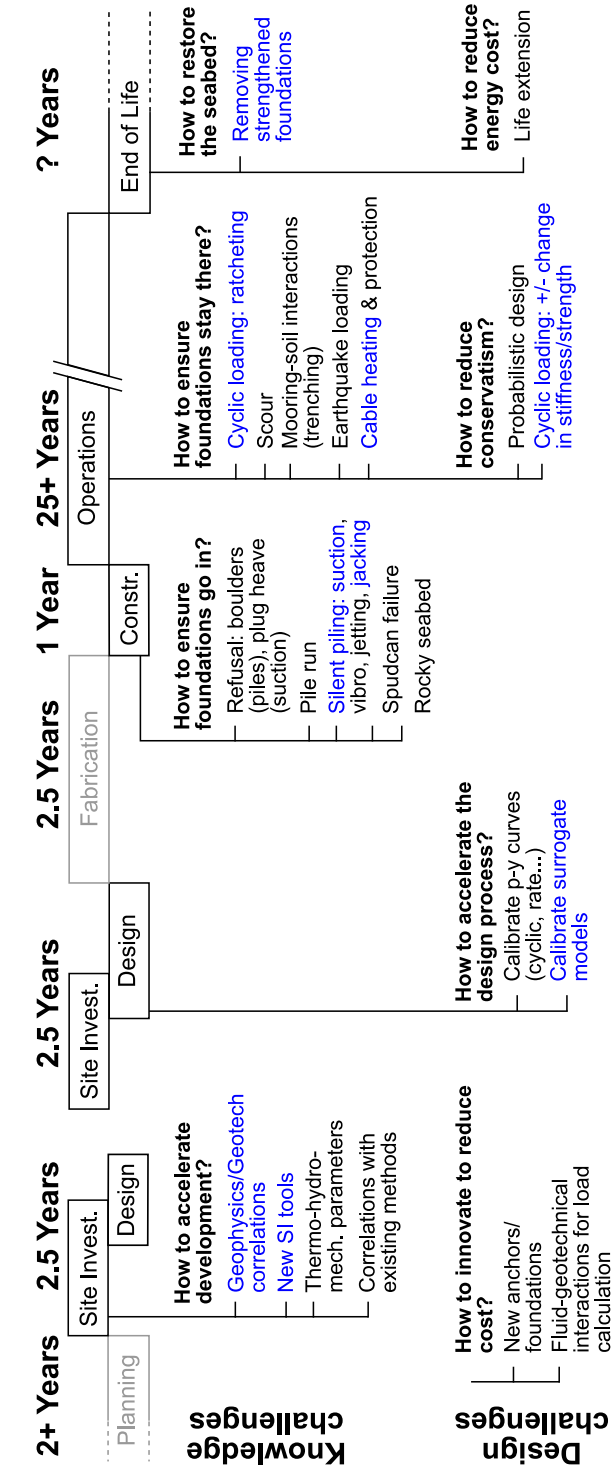

Figure 5: Geotechnical challenges for the offshore wind industry. Typical timeline for an offshore wind farm describing infrastructure /geotechnical steps. Geotechnical challenges addressed in this chapter are shown in blue.

The sparsity of geotechnical data can be reduced by better integrating geophysical data and other existing tests to derive soil mechanical properties. Geophysical site survey is an established phase of site characterisation for an offshore development, involving acoustic methods to identify facies boundaries, obstructions and geohazards. Geophysical surveys are non-intrusive/non-destructive, using travel time of reflected and refracted acoustic waves to provide continuous 2D or 3D maps of geological structures and properties. Statistical and, more recently, machine learning approaches have been applied to link the acoustic properties from the geophysical survey to geotechnical properties that can be used in engineering design (e.g. [SAU19]). Such an approach enables a synthetic geotechnical CPT profile to be predicted at any location across a proposed development site. This offers reduction of schedule in geotechnical site investigation and greater versatility to finalise the turbine layout and cable routes after the site investigation.

The time necessary to undertake site investigation can also be reduced by obtaining more meaningful information from in-situ testing, thus reducing the need for onshore laboratory tests. This can be achieved by developing new site investigation tools that can obtain measure more meaningful data from the ground, for instance by applying different (cyclic) load paths, better replicating the kinematic mechanisms of offshore foundations. For instance, the p-y module of the ROBOCONE [WEN25] can be fitted to a CPT shaft and moves laterally to directly measure p-y curves used for monopile design, hence reducing the overall site investigate phase.

2.2 Silent piling

Pile driving, though the most used installation method, is increasingly restricted by national regulations because of the underwater noise it creates, which can be detrimental to marine fauna [KNA22]. Mitigation measures such as bubble curtains can be deployed, but they are expensive and lead to additional carbon emissions. Pile free-fall, or pile run, is another potential hazard of pile driving, which can result in damage or loss of installation equipment [ERB25]. Therefore, alternative foundations or installation methods have been developed.

Suction installation, which consists of pumping water out of a closed pile to create a differential of pressure between the inside and the outside. This pressure differential creates a static resultant which “silently” pushes the pile into the ground [BIE25]. While this approach is appealing, suction installation does constrain the slenderness ratio (length to diameter) to values less than 1 in sand and 7 in clay, due to the potential instability of the soil plug – the mass of soil inside the foundation, which depends on a combination of the soil strength and permeability. Refusal during suction installation can be mitigated by suction cycling [MAL25], which combines the complexity of cyclic loading and hydro-mechanical couplings, but these phenomena remain to be explored in greater details. The suction effect could also be leveraged in design against cyclic loading, where a large fraction of the applied load is balanced by transient changes in pore water pressure, reducing the changes in effective stress, hence deformation [CER16].

Vibratory-driving is another promising technique to install pile foundations, which has much lower noise emissions [HOL17]. The installation force is provided by an eccentric rotating mass, which vibrate at frequencies in the range 10-30Hz. Vibro-installation is faster than regular pile driving, but the underlying physical mechanisms of pile penetration reduction are still not fully understood, especially in complex offshore ground profiles, and the effect on the resistance of the installed pile still has to be demonstrated. Centrifuge pile hammers have recently been developed to investigate this method (e.g., [MAZ24]), but scaling down this process is particularly complicated to the multiphysical and multiscale phenomena which have to be reproduced. Further innovations include the combination of axial and torsional vibration [TSE23] to improve the method efficiency in stiffer ground layers. These methods are still at the frontier of development and the underlying mechanisms remain to be explored.

While pile jacking would be a silent method to install pile-type foundations, the necessary reaction force to jack piles is equal to the pile static resistance and can be larger than the reaction force that can be provided by installation vessels. The largest component of open-ended jacked piles penetration resistance is due to the progressive accumulation of material on the inside, which is progressively compressed and forms a plug. The base resistance of the pile then becomes similar to a closed-ended pile. This plug formation can be disrupted by rotary installation, which perturbs the plug formation and reduces the shaft axial resistance to enable installation [CER23b], but this phenomenon cannot be adequately predicted yet. Other rotary installation methods include screw piles [DAV22], which are composed of a helical plate attached to a straight shaft to reduce the vertical reaction force required for installation. The large-deformation complex load-path installation is now better understood, but their behaviour in complex layered soils is still to be investigated.

2.3 Cyclic response

Loading on offshore structures is inherently cyclic, due to the repeated action of wind, waves and currents. This cyclic loading occurs at different time scales; the duration of one load cycle is typically 5-15s, and one design storm may last several days. Multiple storms are experienced by a structure over its lifetime, and many millions of lower amplitude cycles are experienced during the OWT operation. This loading can be biased in one direction and, as a consequence, the foundations of offshore structures tend to accumulate displacement (ratcheting) after each cycle. The magnitude of displacement accumulation depends on both the cyclic amplitude and bias, and the rate may decrease with number of cycles as the soil structure changes [LEB10]. This is particularly detrimental for bottom-fixed foundations, as the tilt angle at the top of an OWT foundation must be limited (e.g. to 0.5° in early designs) to maintain its performance. Furthermore, the cyclic secant stiffness of a foundation can evolve with cyclic loading, with both hardening and softening being observed in different soils. This can change the natural frequency of the structure turbine-structure-foundation system, putting it at risk of resonance.

The cyclic loading of soils is a particularly complex problem, as it involves phenomena at multiple time and geometric scales. At the microscopic scale, the cyclic loading mechanisms are governed by progressive densification/loosening, grain crushing, anisotropy or strength degradation [AND15], which lead to progressive settlement accumulation. Those mechanisms are difficult to characterise and model even at the element scale (e.g., DSS tests), where the combination of soil initial properties, stress amplitude and potential consolidation may complicate the prediction of accumulated deformation in clay [LAH25] or sand [WIC14]. Testing for tens of thousands or millions of cycles is also particularly time consuming, costly, and requires specialised equipment, which limits the amount of available data.

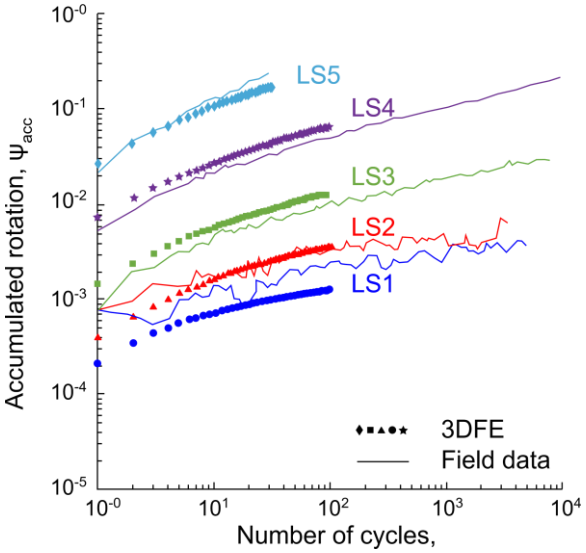

Figure 6 Accumulated pile head rotation at the ground surface, comparison of field tests [BEU17] and numerical simulations [PIS24]. Diameter 0.762m, Length 4m.

Modelling cyclic soil-foundation interaction is even more challenging [PUE13], as the cyclic foundation behaviour is the convolution of a large volume of soil, which is subjected to a range of stress paths and cyclic amplitudes, which vary with depth and distance to the foundation. A range of small-scale physical models have been tested at both 1g [LEB10] or in a geotechnical centrifuge [MAA23], and exhibit a continuously increasing level of sophistication., For example, the development of small-scale hammer for use in-flight, which enable the generation of high-quality results to better understand pile ratcheting. However small-scale models are prone to some scaling issues, for instance due to the relative size of pile models and sand grains, even if centrifuge modelling can better capture realistic stress profiles. Field testing is recognised as the gold standard for the offshore industry, but full-scale testing of large monopiles is not cost effective. Medium-size onshore tests have been undertaken on up to 2.5m diameter piles in order to advance the understanding of pile cyclic behaviour, e.g. in the projects PISA (see Figure 3, [BEU17]), MIDAS [2025], PICASO [BYR25] or SAGE-SAND [LET24]. However, only a limited number of tests can be

undertaken, and they are also prone to some scaling or different ground conditions (e.g. suction due to low water table level). Furthermore, to simplify interpretation, loading is often idealised to packets of constant amplitude sinusoidal cycles which do not reflect realistic storm loading observed in practice. Complex constitutive models can be used to complement these experimental results (e.g. [STA20], [PIS24] in Figure 3), but face the challenging issues of calibration of their numerous parameters, the requirement to simulate the installation phase of the studied foundation and impractically long analysis times for realistic numbers of cycles.

2.4 Power cables

Power cables are another important part of offshore wind farms. Tens of km must be built to connect each OWT to a substation, and then a substation to shore. Interconnection cables also connect several countries and have a very large capacity (>1GW). Cables may be buried into the seabed to protect them from (un-)intentional damage, which leads to several geotechnical challenges [MAC25]. Firstly, the seabed shallow surface must be characterised over km to design the cable burial process, which requires the development of cheap site characterisation methods such as dynamic penetration [SAR25] or the use of autonomous robots. Secondly, buried power cables generate heat during operation, which needs to be dissipated fast enough to avoid the damage of the cable [CAL21]. This is a complex thermo-hydro-mechanically coupled problem, where the dissipation rate strongly depends on thermal soil properties (e.g. conductivity), which need to be characterised in-situ. Thirdly, power cables for floating OWT are “dynamic” as they follow the floater displacement. This results in soil-cable interactions, similar to catenary risers or pipelines [RAN09], where the cable is buried into the seabed. The changes in soil strength and stiffness must be better characterised to make sure that the cable integrity will be maintained over the lifetime of the cable.

3 Design challenges

Design challenges relate to the invention of new design tools or the development of faster design tools that can be used in sparse data environment to optimise foundation and design processes. Improvements are feasible and necessary at all stages of a wind farm construction, from the site investigation to the decommissioning or life extension.

3.1 Surrogate models for design optimisation and cyclic loads

The response of monopile foundations to monotonic loads are relatively well understood. Medium scale field testing campaigns such as the PISA project have been accurately modelled using 3D finite element (FE) approaches [TAB20] that can be applied to new sites where the constitutive behaviour is calibrated with routine tests.

However, wind farms consist of large numbers of turbines installed across a wide are with varying geology. The foundation optimisation process requires numerous time-consuming analyses be conducted, often at each location. Furthermore, even where cyclic field tests are available, suitable constitutive models are complex to calibrate, lack sufficient validation against field tests in a range of materials, and are prohibitively time consuming to run for sufficient cycle numbers. To resolve this, surrogate models are currently used extensively in design.

Surrogate models are simpler 1D (beam, e.g. the PISA model [BUR20], Figure 7(a)) or 0D (macro-element, e.g. the REDWIN model [PAG18]) approaches that significantly simplify the problem by removing the need to directly model the soil constitutive behaviour for each case. Instead, this is captured in the overall macro-element response or 1D soil reaction curves, both of which can be calibrated directly against a limited number of 3D FE analyses. These analyses cover a range of geometry and geological conditions to ensure that the surrogate model captures the required behaviour, and simple functions are fit to this synthetic data to describe each curve. More recently, novel machine learning approaches have been employed to improve the fit achieved in this step [KAM25]. Once calibrated, these efficient models allow optimisation approaches to be employed to minimise the foundation size and therefore cost and installation complexity.

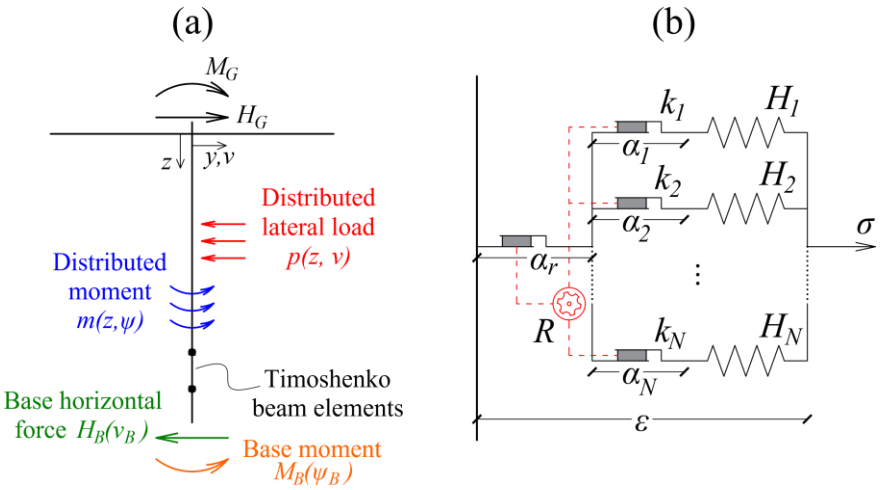

Figure 7: (a) 1D PISA model with soil reaction curves. (b) HARM model

There is currently no consensus in the literature on how to design monopiles for cyclic loading, and recommended approaches are absent from the design standards. However, the model efficiency makes 1D and 0D approaches more suitable that 3D FE for extension to cyclic loading. For example, [LAP25] implemented a version of UDCAM [JOS23] into a 1D pile model. This is a phenomenological cyclic model that is calibrated using contour diagrams based on a number of cyclic DSS tests, each carried out with different average stress and cycle amplitude. This approach requires a cycle counting method that idealises a realistic storm in to packets of sinusoidal cycles, the model then provides a prediction of the displacements at the end of cycling. However,

an ideal modelling approach would allow predictions of the response to realistic storm loading in the time domain. To do this, the Hyperplastic Accelerated Ratcheting Model (HARM, [HOU17], Figure 7(b)) can instead be applied as an extension to a 0D model or 1D soil reaction curve to introduce ratcheting and softening/hardening behaviours. This allows predictions of the accumulated rotation and cyclic secant stiffness changes at any point during a storm. These HARM type approaches have undergone significant development in recent years, transitioning from a research tool into something suitable as a design method. In particular, designers require a model that can be calibrated from routine cyclic soil tests, allowing the method to be applied to a new geology with confidence. Finally, while applications related to monopiles are well studied, there is opportunity to apply the knowledge obtained from these developments to other foundation types.

3.2 Long-term changes in soil properties – Whole-life design

The undrained strength of foundations embedded in soft clays is used for their design, because the time needed for consolidation is much longer than the duration of a storm. Cyclic loading during a storm induces a progressive reduction in undrained strength, due to the accumulation of excess pore water pressure, and any foundation can experience multiple storms over their lifetime. In traditional design, the undrained strength is assumed to continuously decrease storm after storm [AND07]. However, stormy winter seasons alternate with quieter summer seasons, allowing pore water pressure to dissipate and the undrained strength to recover around offshore foundations due to the ensuing consolidation (Figure 8). Accounting for those hydro-mechanical couplings in design has been termed “whole-life design” [GOU22].

The rationale of whole-life design is to ensure that the design resistance at any instant must exceed the design action at that instant, so that changes in design resistance with time can be incorporated. Using this approach, simulations of whole-life loading and geotechnical capacity evolution can be performed, allowing the system reliability over the lifetime to be assessed, incorporating beneficial whole-life geotechnical effects. For instance, it was demonstrated that at 40-50% reduction in a plate anchor area could be achieved at constant probability of failure by accounting for changing soil strength [KWA23]. A similar methodology could be applied to a range of other foundation type, especially monopiles.

Accounting for changes in soil stiffness alters the natural frequency of the foundation-turbine system, especially for monopiles, which can have a detrimental effect on its fatigue life or change it too close to the loading frequency (wave, rotor) [MA23]. In addition, while retrieving foundation will be made arduous by increasing soil strength (decommissioning), this can be leveraged to extend the design life of an existing OWT [DIN23], or to install a new more powerful OWT using the same existing foundation [SPY21].

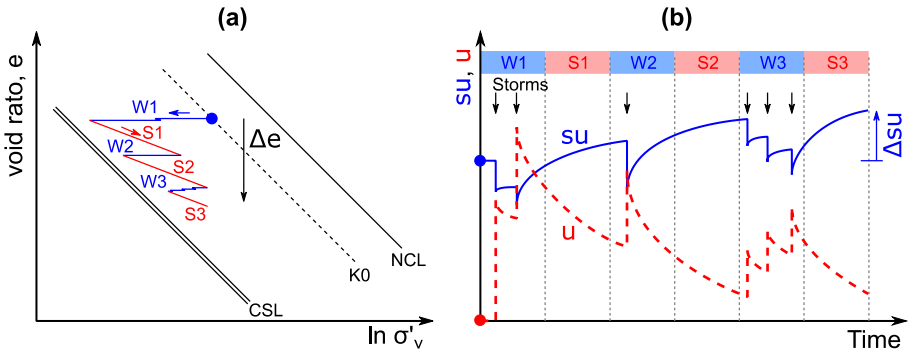

Figure 8: (a) Change in void ratio/vertical effective stress for a representative clay soil element during several winter/summer seasons. (b) Change in undrained strength and dissipation of pore water pressure with time. W = winter, S = summer.

4 Conclusions

The rapid expansion of offshore wind energy, driven by global climate targets, presents a unique opportunity – and necessity – for innovation in geotechnical engineering. The scale, pace, and complexity of offshore wind developments challenge traditional design paradigms inherited from the oil and gas sector, particularly in the context of foundation and anchor systems. This chapter has highlighted how the offshore geotechnical practice must evolve or innovate to become more efficient and include more physics-based models, interpretation and design methods.

Offshore wind foundations are built in a harsh environment and subject to complex cyclic loading over a long period of time. Key knowledge gaps remain, among others, in the characterisation of cyclic soil and foundation behaviour, the integration of geophysical and geotechnical data for site investigation, and the understanding of installation effects on their long-term performance. Bridging those gaps requires to identify complex underlying physical mechanisms by combining physics-informed numerical and physical modelling methods, combined with data rich field-testing campaigns.

Similarly, design challenges persist in the calibration and validation of simplified (e.g., 1D, 0D) models that can be used efficiently across large wind farms with sparse data. Innovations such as silent installation methods, machine learning-based surrogate models, and whole-life reliability frameworks offer promising pathways forward.

5 References

[AND07] Andersen. Bearing capacity under cyclic loading — offshore , along the coast , and on land. The 21st Bjerrum Lecture presented in Oslo, 23 November 2007. *Canadian geotechnical Journal, 46(5): 513-535.* 2009. https://doi.org/10.1139/T09-003

[AND15] Andersen. Cyclic soil parameters for offshore foundation design. *Proceedings of Frontiers in offshore geotechnics III, Oslo.* 2015.

[ARA17] Arany, Bhattacharya, Macdonald, Hogan. Design of monopiles for offshore wind turbines in 10 steps. *Soil Dynamics and Earthquake Engineering*, *92: 126–152,* 2017. https://doi.org/10.1016/j.soildyn.2016.09.024

[BEU17] Beuckelaers. *Numerical modelling of laterally loaded piles for offshore wind turbines*. PhD thesis, University of Oxford. 2017.

[BIE25] Bienen, Shonberg, O'Loughlin, Watson, Bransby. Suction bucket foundations for offshore wind turbines: research and practice. *Proceedings of the 5th International Symposium on frontiers in offshore geotechnics (ISFOG), Nantes, France, 145-160.* 2025. https://doi.org/10.53243/ISFOG2025-658.

[BUR20] Burd, Taborda, Zdravković, Abadie, Byrne, Houlsby, Gavin, Igoe, Jardine, Martin, McAdam, Pedro, Potts, PISA design model for monopiles for offshore wind turbines: application to a marine sand. *Géotechnique, 70(11): 1048–1066*. 2020. https://doi.org/10.1680/jgeot.18.p.277.

[BYR25] Byrne, Buckley, Burd, Crispin, Houlsby, Kamas, Keane, Malhotra, Martin, Nardelli, Qiu, Rasmussen, Shonberg, Simonin, Cunha, Vaitkune, Wen, Wu. PICASO: Cyclic loading of wind turbine monopiles. *Proceedings of the 5th International Symposium on frontiers in offshore geotechnics (ISFOG), Nantes, France, 1773-1779.* 2025. https://doi.org/10.53243/ISFOG2025-506.

[CAL21] Callender, Ellis, Goddard, Dix, Pilgrim, Erdmann. Low computational cost model for convective heat transfer from submarine cables. *IEEE Transactions on Power Delivery, 36(2), 760–768.* 2021. https://doi.org/10.1109/TPWRD.2020.2991783.

[CER16] Cerfontaine, Collin, Charlier. Numerical modelling of transient cyclic vertical loading of suction caissons in sand. *Géotechnique, 66(2): 121-136.* 2016. https: doi.org/10.1680/jgeot.15.P.061.

[CER23b] Cerfontaine, Ciantia, Brown, White, Sharif. DEM study of particle scale effect on plain and rotary jacked pile behaviour in granular materials. *Computers and Geotechnics, 161, 105559, 2023.* https://doi.org/10.1016/j.compgeo.2023.105559.

[CER23a] Cerfontaine, White, Kwa, Gourvenec, Knappett, Brown. Anchor geotechnics for floating offshore wind: Current technologies and future innovations. *Ocean Engineering, 279: 114327*. 2023. https://doi.org/10.1016/j.oceaneng.2023.114327.

[DAV22] Davidson, Brown, Cerfontaine, Al-Baghdadi, Knappett, Brennan, Augarde, Coombs, Wang, Blake, Richards, Ball. Physical modelling to demonstrate the feasibility of screw piles for offshore jacket-supported wind energy structures. *Géotechnique, 72(2): 108-126.* 2022. https://doi.org/10.1680/jgeot.18.P.311.

[DIN23] Dingle, Price, Vega Kurson, Walker. Geotechnical considerations for assessing the life extension of offshore wind foundations. *Ocean Engineering, 284(9): 115074.* 2023.

https://doi.org/10.1016/j.oceaneng.2023.115074

[ERB25] Erbrich, Randolph. Modelling and Avoiding Pile Free-Fall in Offshore Design, *Proceedings of the 5th International Symposium on frontiers in offshore geotechnics (ISFOG), Nantes, France, 179-194.* 2025. https://doi.org/10.53243/ISFOG2025-660.

[GOU22] Gourvenec. Whole Life Design: Theory and Applications of This New Approach to Offshore Geotechnics, *Indian Geotechnical Journal, 52: 11291154.* 2022. https://doi.org/10.1007/s40098-022-00627-x

[GWE25] GWEC. *Global Offshore Wind Report*, 2025. Available at [accessed 18/07/2025]: https://www.gwec.net/gwec-news/offshore-wind-installed-capacity-reaches-83-gw-as-new-report-finds-2024-a-record-year-for-construction-and-auctions

[HOL17] Holeyman, Whenham. Critical Review of the Hypervib1 Model to Assess Pile Vibro-Drivability. *Geotechnical and Geological Engineering, 35(5): 1933-1951.* 2017. https://doi.org/10.1007/s10706-017-0218-8

[HOU17] Houlsby, Abadie, Beuckelaers, Byrne. A model for nonlinear hysteretic and ratcheting behaviour. *International Journal of Solids and Structures, 120: 67–80.* 2017. https://doi.org/10.1016/j.ijsolstr.2017.04.031.

[IEA19] International Energy Agency (IEA). *Offshore Wind Outlook*. 2019. Available at [accessed 18/07/2025]: https://www.iea.org/reports/offshore-wind-outlook-2019

[IRE21] IRENA, GWEC. *A next Decade Action Agenda to advance SDG7 on sustainable energy for all, in line with the goals of the Paris Agreement on Climate Change*. Available at [accessed 18/07/2025]: https://www.un.org/sites/un2.un.org/files/2021/09/irena_and_gwec_offshore_wind_energy_compact_-_final_1.pdf

[JOS23] Jostad, Liu, Sivasithamparam. Accounting for effects of cyclic loading in design of offshore wind turbine foundations. *Proceedings of the 10th European Conference on Numerical Methods in Geotechnical Engineering*, *London, UK*, 2023. https://doi.org/10.53243/NUMGE2023-438.

[KAM25] Kamas, Burd, Byrne. Comparison of machine learning models in a data-driven method for design of laterally loaded monopiles embedded in layered clay sites, *Proceedings of the 5th International Symposium on frontiers in offshore geotechnics (ISFOG), Nantes, France, 865-194*. 2025. https://doi.org/10.53243/ISFOG2025-458.

[KNA22] Van der Knaap, Slabbekoorn, Moens, Van den Eynde, Reubens. Effects of pile driving sound on local movement of free-ranging Atlantic cod in the Belgian North Sea. *Environmental Pollution, 300, 118913.* 2022. https://doi.org/10.1016/j.envpol.2022.118913.

[KWA23] Kwa, White, Tosdevin, Jin, Whole-life modelling of anchor capacity for floating systems: The RSN–CSI approach. *Applied Ocean Research, 138, 103671.* 2023. https://doi.org/10.1016/j.apor.2023.103671.

[LAH25] Laham, Kwa, White, Gourvenec. A surrogate model to efficiently predict changing strength and stiffness of soft soils through whole-life episodic cyclic loading. *Computers and Geotechnics, 177: 106895.* 2025. https://doi.org/10.1016/j.compgeo.2024.106895.

[LAP25] Lapastoure, Jalilvand, Igoe. Validation of a contour diagram-based model for monopile cyclic design in sand and clay. *Acta Geotechnica, 20: 2873-2887*. 2025. https://doi.org/10.1007/s11440-025-02546-6.

[LEB10] Leblanc, Houlsby, Byrne. Response of stiff piles in sand to long-term cyclic lateral loading. *Géotechnique*, *60(2): 79–90*. 2010. https://doi.org/10.1680/geot.7.00196.

[LET24] Letizia, Anoyatis, Simonin, Rattez, Collin, François, Claes, Soete. Geotechnical characterization of a test site in Zeebrugge for large scale tests of monopiles in the framework of the SAGE-SAND project. *Proceedings of the XVIII ECSMGE 2024*, *Lisbon, Portugal, 3088-3093*. 2024. https://doi.org/10.1201/9781003431749-606.

[MA23] Ma, Deng, Chang. Effect of long-term lateral cyclic loading on the dynamic response and fatigue life of monopile-supported offshore wind turbines. *Marine Structures, 93, 103521*. 2024. https://doi.org/10.1016/j.marstruc.2023.103521.

[MAA23] Maatouk, Blanc, Thorel. Impact driving of monopiles in centrifuge : effect on the lateral response in sand. *International Journal of Physical Modelling in Geotechnics, 22(6): 318-331*. 2023. https://doi.org/10.1680/jphmg.21.00035.

[MAC25] MacDonald, Stevens, Arnhardt, Carted, Johnson, Coombs, Bird, Augarde, brown, Sharif. Regional analysis of layered soils in the shallow subsurface across the North Sea for offshore cable burial. *Proceedings of the 5th International Symposium on frontiers in offshore geotechnics (ISFOG), Nantes, France, 808-813*. 2025. https://doi.org/10.53243/ISFOG2025-383.

[MAL25] Mallikarachchi, Joseph, Gütz, Hamdan, Powell, Jones. Two-way pressure cycling during installation of suction buckets in cohesive soil. *Ground Engineering Magazine,* 2025. Available at [accessed 18/07/2025]: https://www.geplus.co.uk/technical-paper/technical-paper-two-way-pressure-cycling-during-installation-of-suction-buckets-in-cohesive-soil-09-04-2025/

[MAZ24] Mazutti, Bienen, Bransby, Randolph, Wager. Development of a mini vibrodriver for pile testing in the centrifuge. *International Journal of Physical Modelling in Geotechnics, 25(1): 34-48*. 2022. https://doi.org/10.1680/jphmg.23.00056.

[PAG18] Page, Grimstad, Eiksund, and Jostad. A macro-element pile foundation model for integrated analyses of monopile-based offshore wind turbines. *Ocean Engineering, 167: 23–35*. 2018. https://doi.org/10.1016/j.oceaneng.2018.08.019.

[PIS24] Pisanò, del Brocco, Ho, Brasile. 3D FE simulation of PISA monopile field tests at Dunkirk using SANISAND-MS. *Géotechnique Letters, 14(2): 1–11*. 2024. https://doi.org/10.1680/jgele.23.00073.

[PIS25] Pisanò, Kementzetzidis, Wang, Marino, Zwaan, Peccin da Silva, Konstadinou, Elkadi, Liu, Askarinejad, Testing and modelling of cyclic monopile behaviour in sand: highlights and insights from the MIDAS project. *Proceedings of the 5th International Symposium on frontiers in offshore geotechnics (ISFOG), Nantes, France, 1592-1598*. 2025. https://doi.org/10.53243/ISFOG2025-76.

[PUE13] Pueche. *Design for cyclic loading*. Proceedings of TC209 workshop 18th ICSMGE, Paris, 2013. Available at [accessed 18/07/2025]: https://www.issmge.org/filemanager/technical_committees/20/Workshop_TC_209_at_18th_ICSMGE_-_Design_for_cyclic_loading_-_piles_and_other_foundations.pdf.

[PUT23] Putuhena, White, Gourvenec, Sturt. Finding space for offshore wind to support net zero: A methodology to assess spatial constraints and future scenarios, illustrated by a UK case study, *Renewable and Sustainable Energy Reviews, 182: 113358.* 2023. https://doi.org/10.1016/j.rser.2023.113358.

[RAN09] Randolph, Quiggin. Non-linear hysteretic seabed model for catenary pipeline contact. *Proceedings of the 28th International Conference on Ocean, Offshore and Arctic Engineering (OMAE) Honolulu, 2009.*

[SAR25] Saresma, White, Mohapatra, Mohammadi, Solowski, Korkoala-Tanttu, Virtasalo, Gourvenec. Assessment of near-surface undrained shear strength of soft seabeds with free fall cone penetrometer testing in the northern Baltic Sea. *Engineering Geology, 346: 107906.* 2025. https://doi.org/10.1016/j.enggeo.2025.107906.

[SAU19] Sauvin, Vanneste, Vardy, Klinkvort, Forsberg. Machine Learning and Quantitative Ground Models for Improving Offshore Wind Site Characterization. *Offshore Technology Conference, 2019.* https://doi.org/10.4043/29351-MS.

[SPY21] Spyroudi. *End-of-life planning in offshore wind*. 2021. Available at [accessed 18/07/2025]: https://cms.ore.catapult.org.uk/wp-content/uploads/2021/04/End-of-Life-decision-planning-in-offshore-wind_FINAL_AS-1.pdf

[STA20] Staubach, Machachek, Moscoso, Wichtmann. Impact of the installation on the long-term cyclic behaviour of piles in sand: A numerical study. *Soil Dynamics and Earthquake Engineering, 138(11): 106223.* 2020. https://doi.org/10.1016/j.soildyn.2020.106223.

[SUT22] SUT OSIG. *Guidance notes for the planning and execution of geophysical and geotechnical ground investigations for offshore renewable energy developments*. 2022. Available at [accessed 18/07/2025]: https://sut.org/123-osig-gn2022/

[TAB20] Taborda, Zdravković, Potts, Burd, Byrne, Gavin, Houlsby, Jardine, Liu, Martin, McAdam, Finite-element modelling of laterally loaded piles in a dense marine sand at Dunkirk. *Géotechnique, 70(11): 1014–1029*. 2020. https://doi.org/10.1680/jgeot.18.pisa.006.

[TAI24] TAILWIND. *Deliverable 3.1 – Sustainable anchor*. 2024

[TSE23] Tsetas, Tsouvalas, Gómez, Pisanò, Kementzetzidis, Molenkamp, Elkadi, Metrikine. Gentle Driving of Piles (GDP) at a sandy site combining axial and torsional vibrations: Part I - installation tests. *Ocean Engineering, 270: 113453.* 2023. https://doi.org/10.1016/j.oceaneng.2022.113453.

[WEN25] Wen, White, Cerfontaine, Gourvenec, Diambra. Interpretative framework for CPT p-y module tests in drained sands: a practical model for end effect elimination considering sand relative density and surcharge pressure. *Computers and Geotechnics, 183(7): 107205.* 2025. https://doi.org/10.1016/j.compgeo.2025.107205.

[WIC14] Wichtmann, Niemunis, Triantafyllidis. Flow rule in a high-cycle accumulation model backed by cyclic test data of 22 sands. *Acta Geotechnica, 9: 965-709.* 2014. https://doi.org/10.1007/s11440-014-0302-7.

Geomechanical challenges in the context of radioactive waste disposal

Anne-Catherine Dieudonné

Delft University of Technology, Faculty of Civil Engineering and Geosciences

Deep geological disposal is widely regarded as the only viable solution for the long-term isolation of radioactive waste. The safe isolation of radioactive waste relies on a multi-barrier concept, whereby safety is ensured through a combination of natural and engineered barriers. Over the lifetime of a disposal facility, these barriers will be subjected to thermo-hydro-mechanical and chemical loads that could impact their integrity and performance. This chapter outlines the geomechanical challenges that arise in this context. Key issues include understanding and predicting the development and evolution of the excavation-damaged zone, the behaviour of backfills and seals, the influence of thermal loads and gas generation on the system and the very long-term behaviour of the repository system. Particular emphasis is placed on the need to integrate fundamental understanding with uncertainty management, and to combine laboratory and field testing (across scales) with robust numerical modelling.

1 Introduction

Since the discovery of nuclear fission in the early 20th century, radioactivity has become a cornerstone of modern technological and scientific progress. Today, nuclear energy provides a substantial portion of the world's low-carbon electricity[1], while radioactive substances and ionising radiation are widely used in medicine, industry, agriculture and scientific research.

Alongside these benefits comes the inevitable production of radioactive waste. Radioactive waste is classified into different categories depending on its activity and the half-life period of its radioactive isotopes [IAE09]. In general, radioactive waste exhibits an inverse relationship between activity and volume. According to [IAE22], very low-level waste (VLLW) and low-level waste (LLW) comprise globally more

[1] According to [EI:25], in 2024, nuclear energy represents about 9% of the world electricity production and 23% of the EU electricity production.

than 92% of the total radioactive waste volume. On the other hand, while representing less than 8% of the waste volume[2], intermediate-level waste (ILW) and high-level waste (HLW), which mostly arise from the nuclear power industry and related research activities, comprise more than 95% of the total radioactivity. Accordingly, this waste is the most harmful to the human health and the environment. It contains long-lived radionuclides whose decay is extremely slow, and they remain therefore toxic over long time periods. As a consequence, the long-term management of this waste is of concern.

In this context, deep geological disposal constitutes one of the most promising solutions for the safe isolation of high-level and intermediate-level radioactive waste [OEC95, NEA08]. It consists in disposing the waste in deep and stable geological formations with good confining conditions in order to remove radioactive waste from the human and natural environment and ensure that the rate of any radionuclide release remains below some prescribed limits [CM87].

This chapter examines the key geomechanical challenges involved in the geological disposal of radioactive waste. It begins by outlining the general concepts underpinning deep disposal repositories. It then explores the thermo-hydro-mechanical and chemical (THMC) loads that affect both the natural and engineered barriers throughout the lifetime of a repository. Building on this, the chapter discusses specific geomechanical challenges, including the development and evolution of the excavation-damaged zone, the behaviour of backfills and seals, the influence of thermal loads and gas generation on the system, and the very long-term behaviour of the repository system.

2 Radioactive waste disposal: general concepts

A geological disposal facility (GDF) is an underground facility constructed at several hundred meters' depth and used to permanently dispose radioactive waste by isolating it from the biosphere. Depending on the country, different geological disposal concepts exist [see SL13, OS22, for reviews]. Yet, in all cases, the safe isolation of the radioactive waste relies on a multi-barrier concept, whereby safety is ensured through a combination of natural and engineered barriers. Figure 1 presents a conceptual scheme of a deep geological repository for radioactive waste.

The natural barrier corresponds to the host and overlying geological formations. Three broad families of geological formations have been considered as potential host formations for the siting of a GDF, namely crystalline rocks (e.g., granite, gneiss), clay-rich formations (e.g., poorly indurated clays, claystones, shales, marls) and salt rock. The choice of host formation is mainly governed by the availability of suitable geological formations with the required thickness and geological setting [IAE09].

The engineered barriers, sometimes termed engineered barrier system or EBS, include different manufactured components, such as the canisters, buffers, and backfilling ma-

[2] According to [IAE22], intermediate-level and high-level waste represents respectively 7.72% and 0.13% of the waste volume.

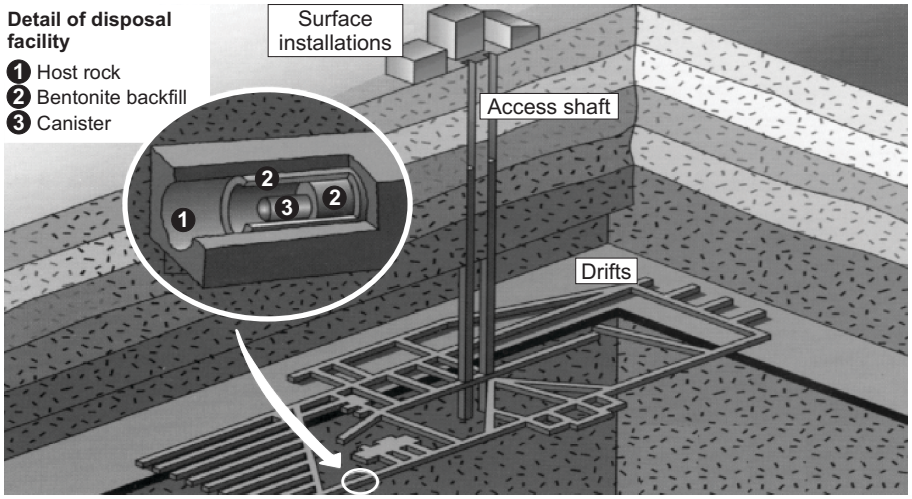

Figure 1: Conceptual scheme of deep geological repository for radioactive waste [GSG+09].

terials. The first engineered barrier is the waste package, which includes the waste form and the waste container (canister), generally made of steel or copper. The canister is designed to retain the radionuclides for thousands of years [SL13]. Depending on the specific concept, canisters are meant to be emplaced in horizontal drifts or in vertical boreholes.

The space between the canisters and the geological formation is usually meant to be filled with concrete or bentonite-based materials, especially in concepts involving crystalline formations. These materials are supplied in the form of compacted blocks or granular bentonite. Crushed host rock, bentonite-based materials, or a mixture of these, are envisaged for backfilling the excavations of the disposal facility. Whether they are used as a buffer, sealing or backfilling material, bentonite-based materials have been selected for their swelling capacity, very low water permeability and high radionuclide sorption capacity.

Geological disposal facilities are developed in several stages, each stage generally requiring a decision and validation by the regulatory body. These include site selection, construction (starting with a so-called pilot), operation and closure. In most cases, the period during which disposal facilities will be operated prior to closure will extend over decades. Accordingly, continuous optimisation of the disposal facility is of paramount importance until closure. This multi-criteria optimisation is possible thanks to scientific research.

3 Multi-physics processes

The multi-barrier system will be affected by multiple mechanical, hydraulic, thermal, chemical and radiological loads throughout the different phases of the radioactive waste repository, including construction, operation and post-closure (Figure 2). Consequently, the properties of the multi-barrier system will evolve over time in response to these loads and the interaction between its components.

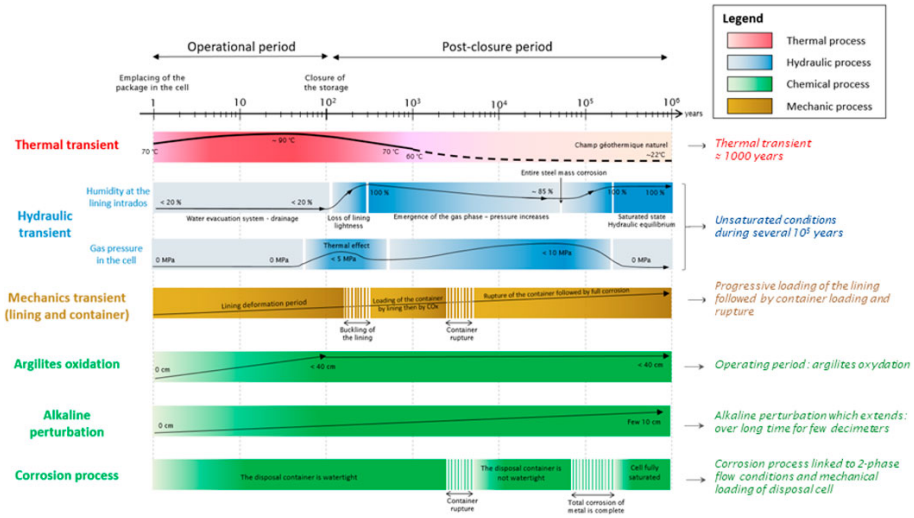

Figure 2: Multi-physics processes affecting the repository and the geological environment during the operational and post-closure phases of a geological disposal facility [CPB+24].

The construction of a geological disposal repository involves the excavation of access shafts, tunnels, and disposal galleries. As a result of the excavation, the host rock experiences significant stress redistribution, leading to local failure of the material and the creation of an excavation damaged zone (EDZ) with modified hydraulic properties [TBD05, BBLDM07]. In disposal concepts relaying on a clay-rich host formation, a concrete support will generally be emplaced to limit the tunnel convergence, ensure tunnel stability and/or guarantee operational safety. After construction and during the operational phase, the tunnels will be ventilated. As a result, the excavations will play a drainage role, and a consolidation process will occur in the surrounding host formation. Ventilation of the tunnels may further lead to partial desaturation of the host formation, possibly modifying the thermo-hydro-mechanical properties of the EDZ [see for instance MSC].

Once heat emitting high-level waste is emplaced, the engineered barrier system and near-field host formation will be subjected to both heating from the waste canister and hydration from the surrounding host material. Accordingly, the closure and early post-

closure phases are marked by progressive saturation of the engineered barrier system and EDZ, while temperatures reach their peak. Strong thermo-hydro-mechanical coupling occurs. Initially unsaturated, bentonite-based buffers and seals will expand and fill technological gaps. Once in contact with the host rock, they will develop swelling stresses, close fractures of the excavation damaged zone, and form a tight contact with the surrounding geological formation in order to limit preferential pathways. Creep and stress relaxation will further affect the host formation. This phase defines the transient hydraulic and mechanical boundary conditions of the repository.

In the long-term post-closure phase, thermal output will decline and the system will gradually approach hydro-mechanical equilibrium. Self-sealing of fractures, chemical equilibration between engineered and natural materials, and long-term creep of the host rock is expected to reduce permeability and porosity. On the other hand, metal corrosion, water radiolysis and bio-degradation will lead to the production of gas, which can create transient overpressures affecting local hydraulic conditions [OVM02].

Throughout all phases, the interplay of coupled processes at different spatial and temporal scales governs radionuclide containment: mechanical evolution controls barrier integrity, hydraulic and thermal fields drive advective/diffusive transport, and chemical conditions dictate sorption and solubility. Predictive performance assessment therefore requires fully coupled, time-dependent thermo-hydro-mechanical and chemical models that integrate these phase-specific processes and their feedbacks to assess repository evolution over very long timescales.

4 Geomechanical challenges

The design of a geological disposal facility for the safe and long-term isolation of radioactive waste raises a number of geomechanical challenges. These are associated with the strongly coupled multi-physics and multi-scale processes affecting the disposal facility, the large space and time scales involved, and the associated uncertainty. Challenges related to understanding and predicting the development and evolution of the excavation-damaged zone, the behaviour of seals and backfills, the influence of thermal loads and gas generation on the system and the very long-term behaviour of the repository system, are described in the following sections.

4.1 Excavation damaged zone (EDZ) and clay host formation - support interaction

As discussed in section 3, the excavation of tunnels and drifts significantly alters the stress field around the excavation, leading to local failure of the material and the creation of an excavation damaged zone [TBD05, BBLDM07]. As a result of both material and stress anisotropy, the EDZ can present different patterns, extent and properties depending on the tunnel orientation (Figure 3) and construction method. Fractures can occur in different modes: tension (opening) fractures, shear fractures, and mixed-mode fractures, which involve a combination of tensile and shear mechanisms. The

long-term isolation of radioactive waste relies on the (very) hydraulic conductivity of the host formation. Therefore, the hydro-mechanical behaviour of the EDZ is a major issue because it may constitute a preferential flow path for radionuclide migration.

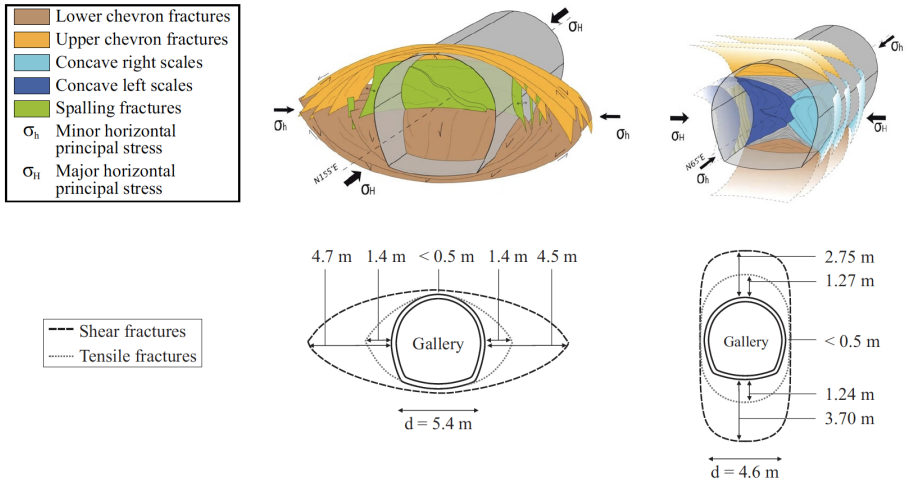

Figure 3: Conceptual model of the induced fractures in Callovo-Oxfordian claystone around drifts parallel to the major (left) and minor (right) horizontal principal stresses ([Par15], after [ALN+14])

Significant efforts have been dedicated to modelling the development of the excavation damaged zone. The representation of strain localisation using classical finite element methods leads to mesh dependency, both in terms of element size and orientation. For this reason, a regularisation technique, either through enrichment of the constitutive model or through enhancement of the continuum kinematics, is required. Such techniques affect computation cost. Accordingly, most simulations continue to be performed primarily in two dimensions. Accurately modelling the three-dimensional development of the EDZ, and capturing the evolution of its properties along the tunnel axis (including fracture connectivity), remains therefore a major challenge. Recent advances in high-performance computing, together with the integration of multi-physics and machine learning approaches, offer promising avenues to address these challenges and to enable more realistic three-dimensional modelling of the EDZ and the repository system.

Several field studies have reported that the hydraulic properties of the EDZ are altered. Although numerical models are capable of reproducing these experimental observations, fully predicting the evolution of hydraulic properties as the EDZ develops remains challenging.

Thermal loading from heat-emitting waste can affect the excavation damaged zone through processes such as water pressurisation and drying. Conversely, time-dependent

mechanisms including creep, stress relaxation, and self-sealing tend to gradually reduce its permeability. Although considerable attention has been given to modelling the initial development of the EDZ, most models do not account for its time-dependent evolution.

Finally, when clays are the host formation, a concrete liner is required to keep the tunnel open during the operational phase, to limit the extent of the excavation damaged zone, and/or to ensure operational safety. Progressive consolidation and creep of the surrounding host formation lead to increasing stresses on the lining. Understanding, and being able to predict, the time-dependent behaviour of the clay-liner interaction is essential for optimising the concrete liner, which can represent a major portion of the cost of constructing a disposal facility. Accordingly, an important avenue of research is the design and development of innovative support systems, such as compressible liners, capable of reducing the loads acting on them.

4.2 Buffer and seal behaviour

Owing to their high swelling capacity, low hydraulic conductivity and high radionuclides retention capacity, bentonite-based materials have been selected as a buffer between the waste canister and the host formation, or as a seal in excavated disposal galleries, in many concepts. Initially unsaturated, the bentonite barrier will be subjected to hydration from the surrounding host rock. As a result, it will first expand and fill the technological gaps. Once in contact with the host rock, the buffer or seal will develop swelling stresses, close fractures of the excavation damaged zone, and form a tight contact with the surrounding geological formation in order to limit preferential pathways.

Due to easier emplacement, many disposal concepts rely on granular bentonite, or a combination of compacted and granular bentonite (Figure 4). In this case, large initial gradients of dry density are expected. Capturing the effect of dry density in constitutive models remains challenging, mostly due to the lack of experimental data systematically investigating the effect of dry density. While there is a large database reporting the effect of dry density on the swelling pressure and saturated permeability, there are limited results of mechanical tests performed along simple stress paths. The experimental characterisation is indeed complex and time demanding. In addition, the complexity of bentonite behaviour generally justifies the realisation of oedometer tests, rather than triaxial tests. However, oedometer tests do not provide a full description of the material behaviour, as the lateral stress state is rarely measured. Therefore, the development of constitutive models and the calibration of the model parameters using experimental tests are made more complex. Oedometer cells allowing the measurement of lateral stress offer an interesting alternative to complex triaxial tests by improving the state of stress characterisation.

Chemical gradients at the bentonite-host rock interface, including alkaline plumes from cementitious components and ion exchange with (saline) porewater from the host formation, can alter the clay fabric, reduce the swelling capacity, and affect the

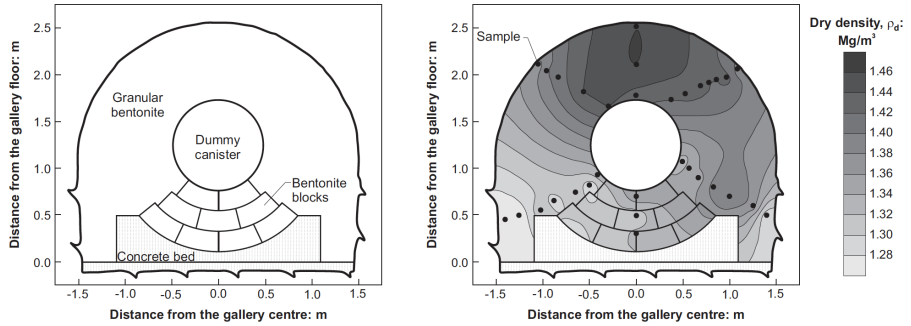

(a) Experimental set-up.

(b) Dry density profile after dismantling.

Figure 4: Engineered Barrier (EB) in situ experiment [MV14].

material permeability. Accordingly, there is a need to better understand the effect of (complex) pore water chemistry on the behaviour of clays, especially when cation exchange is possible, or when the pH is expected to vary. Numerically, this requires coupling (thermo-)hydro-mechanical model for bentonites with transport models.

Finally, calibration of fully coupled multi-physics models for bentonites is generally complex due to the large number of parameters. At times where the source of the bentonite buffer has not been fully set, there is a need to develop clear calibration strategies so that knowledge gained on other materials can be transferred.

4.3 Temperature effects

While most safety cases target a maximum temperature of 90°in the clay host formation, a central question in the design of deep geological repositories is whether higher temperatures can be safely tolerated. Indeed, allowing higher temperatures could bring significant advantages, such as shorter surface storage times, more efficient use of disposal space, and reduced repository footprints. However, increasing the thermal load would also intensify the mechanical and hydraulic stresses acting on both the engineered barriers and the surrounding host rock. When heat is generated by the decay of radioactive waste, it causes pore water within the low-permeability host rock to expand much more than the solid mineral skeleton. Because drainage is limited, this expansion leads to a build-up of excess pore pressure, a process known as thermal pressurisation. The resulting reduction in effective stress can bring the rock closer to failure conditions or induce localised shear deformation, especially in the near field where stress concentrations and excavation-induced damage are already present. This poses a risk to the stability of the excavation damaged zone, which is mechanically weaker and more permeable than intact rock. Accordingly, understanding whether the integrity of the system can be preserved under such conditions is therefore crucial, and recent research within the EURAD programme [VBC$^+$25], has

highlighted several geomechanical challenges that must be addressed.

Testing geomaterials at high temperature poses significant experimental challenges, beginning with the limitations of conventional laboratory equipment. Standard oedometers, triaxial cells, and pore pressure measurement systems are typically designed for ambient or mildly elevated temperatures, and adapting them for prolonged high-temperature operation requires specialised materials, insulation, and instrumentation. Sensors for stress, strain, and pore pressure must remain accurate and stable under thermal cycling, and heating systems must ensure uniform temperature fields to avoid artificial gradients that could induce non-representative stresses. Beyond equipment constraints, reproducing repository-like thermo-hydro-mechanical conditions is inherently difficult. Heating low-permeability materials such as claystones or compacted bentonites generates thermal pressurisation that must be carefully controlled to prevent unintended drainage or evaporation. High temperatures also accelerate time-dependent processes such as creep and structural rearrangement, meaning that experiments often need to run for months or even years to capture relevant behaviour. Collectively, these challenges make systematic experimental characterisation of high-temperature effects on geomaterials both complex and resource-intensive.

4.4 Gas transport

Over the lifespan of a geological disposal facility (GDF), a large amount of gas is expected to be produced as a result of metal corrosion, water radiolysis and biodegradation [OVM02]. Although the gas generation processes are generally slow, it is essential to ensure they do not compromise the proper functioning of the disposal system. The low permeability of the engineered barrier system, while beneficial for the containment function of a repository, also restricts the dissipation of generated gas. Consequently, gas could accumulate more rapidly than it can be transported through the engineered barrier components, potentially leading to the formation of a gas phase within the repository. If the accumulated gas pressure becomes excessive, it could force gas to migrate into the host formation by forming gas-specific pathways through the EBS and/or the host rock.

[MHG05] conceptualised four possible gas transport mechanisms in clay-based materials based on phenomenological considerations (Fig. 5). The model distinguishes between advection and diffusion of gas dissolved in the pore water, visco-capillary two-phase flow, dilatancy-controlled gas flow (pathway dilation), and gas transport along macroscopic tensile fractures (gas fracturing). While the conceptual model still serves as reference for our understanding of gas migration in clays, the conditions controlling the activation and prevalence of each mechanism are not fully understood. It it expected that these depend not only on the hydraulic and mechanical properties of the clay (permeability, gas-entry value, mechanical strength, etc.), but also on the gas pressure at the injection locus and the hydro-mechanical state of the clay (i.e. pore pressure and stress state).

Experimental studies have shown that gas transport in saturated clay-based materials

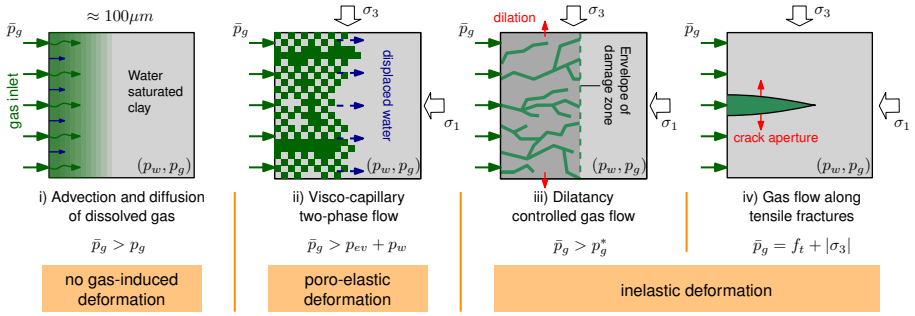

Figure 5: Gas transport processes in water saturated clay depending on the relation between the injection pressure $\bar{p}_g$ with the the state variables p_w (liquid phase pressure), p_g (gas phase pressure), and σ_3 (minimum compressive principal stress), and the material properties p_{ev} (gas-entry value) and f_t (tensile strength). Adapted from [MHG05].

is highly heterogeneous and occurs along discrete pathways. Capturing this behaviour in experiments remains challenging, partly because gas injection tests require a fully sealed system to prevent leaks. In practice, maintaining such sealing is difficult, and relatively high gas injection rates have often been used to overcome these limitations. The discrete nature of gas flow further complicates measurements, highlighting the need to develop non-invasive monitoring techniques that can characterise gas migration without disturbing the system. Techniques capable of detecting and mapping the formation and evolution of discrete gas pathways are particularly important to improve our understanding of gas transport processes under repository-relevant conditions.

From a modelling perspective, predicting gas migration in saturated clay-based systems is inherently complex. The discrete nature of the phenomenon, the strong pneumo-hydro-mechanical coupling, and the impact of material heterogeneity challenges conventional numerical approaches. Deterministic approaches enabling discrete gas flow through fractures or high-permeability pathways provide a useful framework. However, achieving truly predictive capabilities remains challenging and probably calls for probabilistic approaches.

Finally, ensuring safe gas migration also depends on the development of gas-permeable seals within the EBS. Unlike traditional low-permeability barriers, gas-permeable seals (generally made of sand/bentonite mixtures) are designed to allow controlled gas escape while maintaining containment of solutes through a low water permeability. Their design and implementation of such gas-permeable seals require careful consideration of material selection to ensure sufficient swelling capacity and low water permeability, representing an important area of ongoing research in the management of gas in deep geological repositories.

4.5 Long-term behaviour

A unique feature of a geological disposal facility for radioactive waste is the very long timescales over which it should perform its safety function. The construction and operation of such a facility is expected to take several decades, closure may require an additional decade, and the system must continue to fulfil its safety functions for hundreds of thousands of years. In contrast, most of our knowledge has been derived from laboratory and field experiments spanning, at best, a few decades.

Clay-rich and salt rock host formations experience time-dependent deformation, including viscoplastic creep and stress relaxation, which affect excavation-induced stresses and promote self-sealing of the excavation damaged zone through fracture closure and compaction. Bentonite barriers undergo parallel long-term evolution: ongoing hydration drives continued swelling and partial homogenisation of density. Chemical alterations, such as cement–clay interactions, mineral dissolution and precipitation, and ion exchange, can modify porosity, suction, and swelling pressure. Canister corrosion produces gas, which may induce transient fracturing and local desaturation.

Thermal loads increase the rate of many of these processes, including creep, chemical reaction, and excess pore water development, thereby affecting the multi-barrier state and transport properties. Predictive modelling of such coupled behaviour is inherently challenging due to strong interactions between processes, rate-dependent material responses, and scale effects. Fully coupled THMC simulators, equipped with time-dependent constitutive laws and validated against in situ experiments, are required. Robust propagation of uncertainty is also important given the large space and time scales involved.

Addressing this challenge requires a fundamental understanding of the governing multi-physical processes and the development of reliable methods for uncertainty quantification. In addition, natural analogues provide an invaluable source of information to increase confidence in our models, thereby supporting both predictive capability and public trust in the long-term safety of geological disposal.

5 Conclusions

The long-term safety of deep geological repositories hinges on the reliable performance of a complex multi-barrier system subjected to evolving thermo-hydro-mechanical-chemical (THMC) loads. This chapter has highlighted some of the key geomechanical challenges that must be addressed to ensure barrier integrity over geological timescales. These challenges include characterising and predicting the formation and evolution of the excavation-damaged zone, understanding the coupled mechanical and hydraulic behaviour of backfills and seals, and assessing the impacts of thermal stresses and gas generation on the surrounding host rock and engineered components.

Meeting these challenges requires an integrated approach that combines fundamental process understanding with systematic uncertainty management. Laboratory ex-

periments, in situ tests, and long-term monitoring programmes must be designed to capture processes across relevant spatial and temporal scales. These insights need to be complemented by advanced numerical modelling capable of representing coupled THMC phenomena and their evolution over time. Ultimately, progress in linking experimental evidence, mechanistic modelling, and performance assessment is essential to build confidence in the safety case and to demonstrate the long-term containment capability of deep geological disposal systems.

References

[ALN+14] G. Armand, F. Leveau, C. Nussbaum, R. de La Vaissiere, A. Noiret, D. Jaeggi, P. Landrein, and C. Righini. Geometry and properties of the excavation-induced fractures at the Meuse/Haute-Marne URL drifts. *Rock Mechanics and Rock Engineering*, 47:21–41, 2014.

[BBLDM07] P. Blümling, F. Bernier, P. Lebon, and C. Derek Martin. The excavation damaged zone in clay formations time-dependent behaviour and influence on performance assessment. *Physics and Chemistry of the Earth*, 32:588–599, 2007.

[CM87] N. A. Chapman and I. G. McKinley. *The geological disposal of nuclear waste*. John Wiley & Sons, 1987.

[CPB+24] F. Claret, N. I. Prasianakis, A. Baksay, D. Lukin, G. Pepin, E. Ahusborde, B. Amaziane, G. Bátor, D. Becker, A. Bednár, M. Béreš, S. Bérešová, Z. Böthi, V. Brendler, K. Brenner, J. Březina, F. Chave, S. V. Churakov, M. Hokr, D. Horák, D. Jacques, F. Jankovský, C. Kazymyrenko, T. Koudelka, T. Kovács, T. Krejčí, J. Kruis, E. Laloy, J. Landa, T. Ligurský, T. Lipping, C. López-Vázquez, R. Masson, J. C. L. Meeussen, M. Mollaali, A. Mon, L. Montenegro, B. Pisani, J. Poonoosamy, S. I. Pospiech, Z. Saâdi, J. Samper, A.-C. Samper-Pilar, G. Scaringi, S. Sysala, K. Yoshioka, Y. Yang, M. Zuna, and O. Kolditz. EURAD state-of-the-art report: development and improvement of numerical methods and tools for modeling coupled processes in the field of nuclear waste disposal. *Frontiers in Nuclear Engineering*, 3, 2024.

[EI:25] Statistical review of world energy (2025), 2025.

[GSG+09] A. Gens, M. Sánchez, L. Guimarães, E. E. Alonso, A. Lloret, S. Olivella, M. V. Villar, and F. Huertas. A full-scale in situ heating test for high-level nuclear waste disposal: observations, analysis and interpretation. *Géotechnique*, 59(4):377–399, 2009.

[IAE09] IAEA. Classification of radioactive waste. General safety guide. *IAEA Safety Standards*, GSG-1:68, 2009.

[IAE22] IAEA. Status and trends in spent fuel and radioactive waste management. *IAEA Nuclear Energy Series*, NW-T-1.14:68, 2022.

[MHG05] P. Marschall, S. Horseman, and T. Gimmi. Characterisation of gas transport properties of the Opalinus Clay, a potential host rock formation for radioactive waste disposal. *Oil and Gas Science and Technology*, 60(1):121–139, 2005.

[MSC] J.M. Matray, S. Savoye, and J. Cabrera. Desaturation and structure relationships around drifts excavated in the well-compacted tournemire's argillite (Aveyron, France). *Engineering Geology*, 90(1–2).

[MV14] J. C. Mayor and M. Velasco. EB dismantling. Synthesis report. Technical report, Long-term Performance of Engineered Barrier Systems PEBS, 2014.

[NEA08] NEA. Moving forward with geological disposal of radioactive waste, a collective statement by the NEA Radioactive Waste Management Commitee (RWMC). Technical report, OECD – Nuclear Energy Agency, 2008.

[OEC95] OECD/NEA. The environmental and ethical basis of geological disposal of long-lived radioactive wastes. ïA collective opinion of the Radioactive Waste Management Committee of the OECD Nuclear Energy Agency. Technical report, OECD – Nuclear Energy Agency, 1995.

[OS22] M.I. Ojovan and H.J. Steinmetz. Approaches to disposal of nuclear waste. *Energies*, 15(20):7804, 2022.

[OVM02] L Ortiz, G Volckaert, and D Mallants. Gas generation and migration in Boom Clay, a potential host rock formation for nuclear waste storage. *Engineering Geology*, 64:287–296, 2002.

[Par15] B. Pardoen. *Hydro-mechanical analysis of the fracturing induced by the excavation of nuclear waste repository galleries using shear banding*. PhD thesis, Université de Liège, 2015.

[SL13] P. Sellin and O. X. Leupin. The use of clay as an engineered barrier in radioactive-waste management – a review. *Clays and Clay Minerals*, 61(6):477–498, 2013.

[TBD05] C.F. Tsang, F. Bernier, and C. Davies. Geohydromechanical processes in the excavation damaged zone in crystalline rock, rock salt, and indurated and plastic clays – in the context of radioactive waste disposal. *International Journal of Rock Mechanics & Mining Sciences*, 42:109–125, 2005.

[VBC+25] M.V. Villar, P. Bésuelle, F. Collin, R. Cuss, C. de Lesquen, A. Dizier, G. El Tabbal, A. Gens, C.e Graham, D. Grgic, J. Harrington, C. Imbert, O. Leupin, S. Levasseur, A. Narkūnienė, E. Simo, and A. Tatomir.

EURAD state-of-the-art report: thermo-hydro-mechanical behaviour at high temperature of host clay formations. *Frontiers in Nuclear Engineering*, Volume 4, 2025.

Thermo-hydro-mechanical couplings in the context of shallow energy geo-structures

Jean-Michel Pereira

École nationale des ponts et chaussées, Institut Polytechnique de Paris

This chapter provides an overview of thermo-hydro-mechanical (THM) couplings in geomaterials, with a focus on their relevance to shallow energy geo-structures. A thermodynamic framework is first introduced, highlighting the importance of strain-work conjugate variables and the derivation of constitutive equations for porous materials. A poromechanical framework considering both reversible and irreversible processes is introduced, along with its extension to thermoporoelasticity. A review of experimental observations illustrates how temperature influences the mechanical, and hydraulic properties of soils and rocks, including phenomena such as thermal consolidation, thermal pressurisation, and changes in permeability. Constitutive modelling strategies are discussed, ranging from classical elastoplastic models to advanced approaches accounting for cyclic loading. The challenges and limitations of fully coupled versus simplified modelling strategies are addressed, with examples from engineering practice. Applications in energy geotechnics are briefly reviewed, demonstrating the necessity of THM analysis for safe and efficient design. The chapter concludes by emphasizing the ongoing need for robust THM models and simulation tools to support the energy transition and the sustainable development of geo-structures.

1 Introduction

Energy geo-engineering plays a crucial role in the energy transition [SAE+22]. Temperature variations are increasingly considered in geotechnical engineering, affecting a wide range of applications such as thermo-active geostructures, radioactive waste disposal, energy storage in geological reservoirs, and slope stability analyses. From a fundamental standpoint, research into the effects of temperature on geomaterial behavior has grown substantially over recent decades. Figure 1 illustrates the rising number of research articles addressing temperature or thermal topics in geotechnical engineering journals. Notably, the earliest paper identified by the query in Figure 1 was published in the journal *Géotechnique* and examined soil insulation against thermal impacts from industrial facilities [WS50]. After a period of gradual growth, pub-

lication rates accelerated around the year 2000, with early signs in the 1990s linked to studies on radioactive waste disposal. The surge since 2000 is largely attributed to research on thermo-active energy geostructures, with the most cited paper from the query focusing on this topic [Bra06], also in *Géotechnique*.

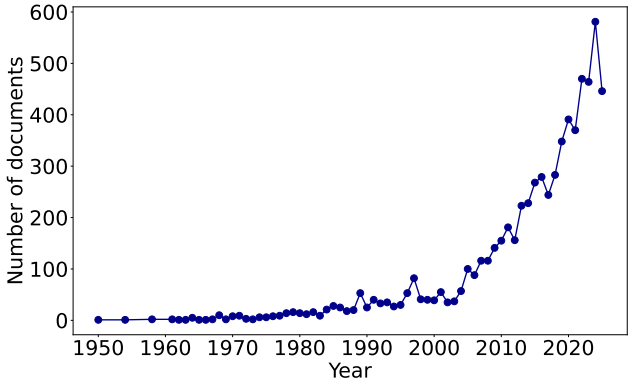

Figure 1: Number of documents published in geotechnical engineering journals mentioning temperature or thermal issues in their title, abstract, or keywords. Data from Scopus, query performed on 2025/07/13: ((TITLE-ABS-KEY(therm* OR temperature*) AND SRCTITLE(geotech* OR geomech* OR "soil mech*" OR "soil* foundation*")) AND (LIMIT-TO(DOCTYPE,"ar") OR LIMIT-TO(DOCTYPE,"re") OR LIMIT-TO(DOCTYPE,"no") OR LIMIT-TO(DOCTYPE,"er") OR LIMIT-TO(DOCTYPE,"le"))).

Thermal effects influence many geotechnical applications, making it essential to understand the fundamental mechanisms governing coupled thermo-hydro-mechanical behavior in geomaterials for reliable geostructure performance predictions. Examples include landscape evolution processes such as rapid landslides [PA10, VVT07] and rock cliff stability [GMV21], offshore geotechnics involving pipe-soil interactions [DWG08], thermo-active geostructures [LD13], radioactive waste disposal [Del10], geological storage of carbon dioxyde [PP13], gas storage in porous media [ZSAP17], and deep geothermal energy production. Many of these are directly related to energy geotechnics [SAE+22].

This chapter provides an overview of the main aspects of thermo-hydro-mechanical (THM) behavior in geomaterials. The focus is on mechanical response at both the material and soil-structure interface scales, as well as hydraulic and thermal properties. Key considerations in constitutive modeling under coupled THM conditions are discussed, including the distinction between fully coupled and simplified modeling strategies commonly used in geotechnical engineering. Recent advances in engineering applications where THM behavior is significant are also briefly reviewed.

2 Starting from thermodynamics

2.1 Definitions

Geomaterials, i.e., materials of geological origin, are inherently porous, comprising a solid phase and a pore space that may be filled with water, air, or other fluids. The total volume of a geomaterial is thus the sum of the solid volume and the pore volume. The fraction of the total volume occupied by pores is termed the porosity. In soil mechanics, it is common to refer to the solid phase as the basis for volume calculations, leading to the definition of the void ratio as the ratio of pore volume to solid volume (see Figure 2). Additionally, the degree of saturation of water quantifies the proportion of the pore space that is filled with water.

A representative elementary volume (REV) of the geomaterial is now considered. It is assumed large enough to be representative of the material's properties at the engineering (i.e. continuous) scale but small enough to neglect heterogeneities appearing at larger scales. At the REV scale (i.e. scale of the material point), the intrinsic density of a geomaterial is defined as the mass of solid particles per unit volume of the solid phase. The apparent density, on the other hand, is defined as the mass of solid particles per unit volume of the total material, including both solid and pore volumes (see Figure 3).

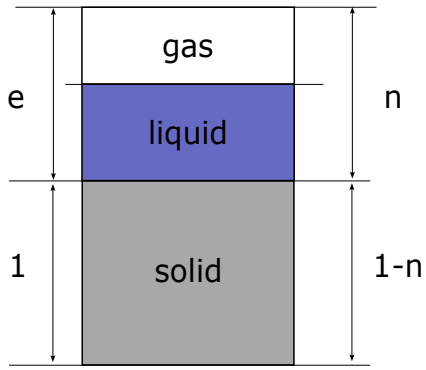

Figure 2: Soil fractions. The reference volume is the solid phase volume when using the void ratio (left), and the total volume when using the porosity (righ).

In the following, we will use the void ratio e and the porosity n to describe the proportions of the constituents of the studied porous materials. The definitions, at the scale of the REV, are as follows:

$$e = \frac{V_v}{V_s} = \frac{n}{1-n} \tag{1}$$

$$n = \frac{V_v}{V} = \frac{e}{1+e} \tag{2}$$

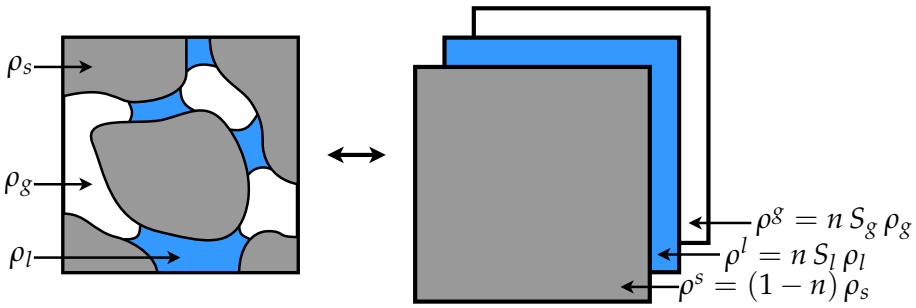

Figure 3: Intrinsic and apparent densities, at the scale of the material point.

where V_v is the pore (void) volume, V_s is the solid volume, and V is the total volume of the material. The degree of saturation of the liquid phase S_l is defined as follows:

$$S_l = \frac{V_l}{V_v} \tag{3}$$

where V_l is the volume of liquid (usually water) in the pore space. The degree of saturation is a dimensionless quantity ranging from 0 (dry material) to 1 (fully saturated material).

In geomechanics or mechanics of porous materials, since the solid skeleton is deforming in response to loadings of various natures, a reference configuration is needed. It is usually chosen as the configuration at the beginning of the loading process, where the material is considered underformed. In the following, we will assume small deformations of the material, meaning that the initial configuration is close to the current configuration. This assumption is valid for most geotechnical applications, except for landslides or rockfalls, or when the installation process (of driven piles for instance) is studied. In these cases, formulations considering large deformations are to be used. Readers are referred to [LZ19] for a review of the various approaches to large deformations in geomechanics.

It is important to note that the definitions of porosity and void ratio given by equations (1) and (2) refer to the actual volumes (at time t). They are by essence eulerian quantities, i.e. defined with respect to the current configuration. The lagrangian porosity ϕ is defined as the ratio of the current pore volume to the initial solid volume:

$$\phi = \frac{V_v}{V_0} \tag{4}$$

2.2 Energetic approach

2.2.1 Strain-work conjugate variables and state equations

Rigorously deriving constitutive laws for geomaterials requires a properly defined thermodynamic framework. The first step is to define the system of interest. As done

by Coussy [CPV10], the solid skeleton is usually the system considered in geomechanics. It comprises the solid phase and the interfaces between the different phases. The fluid phases themselves are excluded, since their behaviour is known *a priori*. This definition is pertinent when the fluid phases and the solid phase interact through their pressure only. When the fluid state depends on interactions with the surface of the solid (e.g. when the fluid adsorbes onto the solid surface) and that these interactions affect the behavior of the solid skeleton, extension of the usual poromechanics framework have to be considered [VBLC10, BVP12]. Once defined, the system is described by a set of state variables. The balance of energy, written at the continuum scale, for the system lets appear the pairs of conjugated variables.

In the following, the focus is primarily on soils, both saturated and unsaturated, within a temperature range of 0 to 100 °C. Consequently, phase changes of pore water are not addressed in detail in this work. The energetic approach adopted here to formulate constitutive equations is illustrated by starting with the simple example of the infinitesimal work $\mathrm{d}W$ input to:

- a 1D spring subjected to a force F elongating it of $\mathrm{d}x$:

$$\mathrm{d}W = F\,\mathrm{d}x$$

- a non-porous solid subjected to a pressure p changing its volume by $-\,\mathrm{d}V$:

$$dW = -p\,\mathrm{d}V$$

- a porous solid subjected to both a total stress p changing its volume by $-\,\mathrm{d}V$ and a fluid pressure p_l contributing to a change in porous volume of $\mathrm{d}nV$:

$$dW = -p\,\mathrm{d}V + p_l\,\mathrm{d}(n\,V)$$

In the continuity, defining now the infinitesimal strain work $\mathrm{d}w$ input to the initial volume of the solid skeleton as $\mathrm{d}W = \mathrm{d}w\,V_0$ leads to:

$$dw = p\,\mathrm{d}\epsilon_v + p_l\,\mathrm{d}\phi \tag{5}$$

where ϕ is the lagrangian porosity, defined with respect to the initial (undeformed) configuration.

Extending this reasoning to the triaxial stress space, the infinitesimal work input to the initial volume of the solid skeleton can be written as:

$$\mathrm{d}w = p\,\mathrm{d}\epsilon_v + q\,\mathrm{d}\epsilon_q + p_l\,\mathrm{d}\phi \tag{6}$$

The strain-work conjugate variables then clearly appear as:

$$p \longleftrightarrow \epsilon_v; \qquad q \longleftrightarrow \epsilon_q; \qquad p_l \longleftrightarrow \phi$$

Interestingly, following [Cou04], if we now assume the incompressibility of the solid grains ($K_s \gg K$), the deformation of the solid skeleton is directly linked to changes in porosity:

$$\mathrm{d}\epsilon_v = -\,\mathrm{d}\phi \tag{7}$$

so that the strain-work input writes as follows, matching the one given in [SW68]:

$$dw = (p - p_l)\,\mathrm{d}\epsilon_v + q\,\mathrm{d}\epsilon_q = p'\,\mathrm{d}\epsilon_v + q\,\mathrm{d}\epsilon_q \tag{8}$$

pointing out to the following conjugate variables:

$$p' = \frac{1}{3}(\sigma'_1 + 2\sigma'_3) \longleftrightarrow \epsilon_v = \epsilon_1 + 2\epsilon_3$$

and

$$q = \sigma_1 - \sigma_3 \longleftrightarrow \epsilon_q = \frac{2}{3}(\epsilon_1 - \epsilon_3)$$

In tensorial form, the work input is:

$$\mathrm{d}w = \boldsymbol{\sigma} :\, \mathrm{d}\boldsymbol{\epsilon} + p_l\,\mathrm{d}\phi = \sigma_{ij}\,\mathrm{d}\epsilon_{ij} + p_l\,\mathrm{d}\phi \tag{9}$$

the strain-work conjugate variables being:

$$\boldsymbol{\sigma} \longleftrightarrow \boldsymbol{\epsilon}; \qquad p_l \longleftrightarrow \phi$$

or, assuming incompressibility of the solid phase:

$$\mathrm{d}w = \boldsymbol{\sigma}' :\, \mathrm{d}\boldsymbol{\epsilon} = \sigma'_{ij}\,\mathrm{d}\epsilon_{ij} \tag{10}$$

and

$$\boldsymbol{\sigma}' \longleftrightarrow \boldsymbol{\epsilon}$$

When considering non-reversible processes, the application of first and second laws of thermodynamics leads to the Clausius-Duhem inequality:

$$\mathrm{d}D = \mathrm{d}w - \mathrm{d}F \geq 0 \tag{11}$$

where D is the dissipation and F, the free energy of the solid skeleton.

This inequality reduces to the following expression when considering infinitesimal reversible processes:

$$\mathrm{d}D = \sigma_{ij}\,\mathrm{d}\epsilon_{ij} + p_l\,\mathrm{d}\phi - \mathrm{d}F \geq 0 \tag{12}$$

In such an elastic case (strictly speaking), there is no dissipation ($\mathrm{d}D = 0$) and $\boldsymbol{\epsilon} = \boldsymbol{\epsilon}^e$ and $\mathrm{d}\phi = \mathrm{d}\phi^e$ so that the free energy can be expressed as:

$$\mathrm{d}F = \sigma_{ij}\,\mathrm{d}\epsilon_{ij} + p_l\,\mathrm{d}\phi \tag{13}$$

Hence, we deduce that $F = F(\boldsymbol{\epsilon},\, \phi)$ and the following state equations hold:

$$\boldsymbol{\sigma} = \frac{\partial F}{\partial \boldsymbol{\epsilon}} \tag{14}$$

$$p_l = \frac{\partial F}{\partial \phi} \tag{15}$$

Once an appropriate energy potential is identified, the constitutive relations for the porous material satisfying the thermodynamic requirements can be derived. As an illustration, linear constitutive relations would derive from a quadratic potential. A detailed discussion of the thermodynamic framework for porous materials is beyond the scope of this chapter, and interested readers are referred to Coussy [Cou04, Cou10] for a comprehensive overview.

2.2.2 Linear poroelasticity

In the case of reversible processes, linear constitutive equations can be derived from a quadratic energy potential. The stress-strain relations for a linear poroelastic material can be expressed as follows, considering a stress- and pressure-free reference state:

$$\boldsymbol{\sigma} = \mathbb{D}\,\boldsymbol{\epsilon} - b\,p_l\,\boldsymbol{\delta} \tag{16}$$

$$\Delta\phi = \phi - \phi_0 = -b\,\epsilon_v + \frac{p_l}{N} \tag{17}$$

If the reference state is a pre-stressed state, then, the stress-strain relations can be written as:

$$\boldsymbol{\sigma} - \boldsymbol{\sigma}_0 = \mathbb{D}\,\boldsymbol{\epsilon} - b\,(p_l - p_{l,0})\,\boldsymbol{\delta} \tag{18}$$

$$\Delta\phi = -b\,\epsilon_v + \frac{p_l - p_{l,0}}{N} \tag{19}$$

where $\mathbb{D}$ is the stiffness matrix, b is the Biot coefficient, and N is the Biot modulus:

$$b = 1 - \frac{K}{K_s} \tag{20}$$

$$\frac{1}{N} = \frac{b - \phi_0}{K_s} \tag{21}$$

2.2.3 Nonlinear poroelasticity

Nonlinear poroelasticity corresponds to the situation where the material parameters depend on the state variables. In this case, material parameters are tangent properties and depend on the material state. The constitutive equations are expressed in incremental form as follows:

$$\mathrm{d}\boldsymbol{\sigma} = \mathbb{D}(\boldsymbol{\sigma}, p_l)\,\mathrm{d}\boldsymbol{\epsilon} - b(\boldsymbol{\sigma}, p_l)\,\mathrm{d}p_l\,\boldsymbol{\delta} \tag{22}$$

$$\mathrm{d}\phi = -b(\boldsymbol{\sigma}, p_l)\,\mathrm{d}\epsilon_v + \frac{\mathrm{d}p_l}{N(\boldsymbol{\sigma}, p_l)} \tag{23}$$

Inspecting equations (22) and (23) The Biot coefficient b is defined as the ratio of the change in total stress to the change in pore pressure. The Biot modulus N is defined as the ratio of the change in porosity to the change in pore pressure. These two quantities characterize the coupling between mechanical and hydraulic behavior in porous materials.

2.2.4 Stress variable(s)

Without any loss of generality, considering isotropic cases only, equation (22) reduces to:

$$\mathrm{d}\sigma = K\,\mathrm{d}\epsilon_v + b\,\mathrm{d}p_l \tag{24}$$

and we can introduce the Biot stress:

$$\mathrm{d}\sigma" = \mathrm{d}\sigma - b\,\mathrm{d}p_l \tag{25}$$

so that:

$$\mathrm{d}\sigma" = K\,\mathrm{d}\epsilon_v \tag{26}$$

showing that the Biot stress is the stress variable conjugated to the strain $\boldsymbol{\epsilon}$.

For soils, the bulk modulus of the material is generally negligible compared to the bulk modulus of the solid constituent:

$$b = 1 - \frac{K}{K_s} \approx 1 \tag{27}$$

$$N \to \infty \tag{28}$$

so that the Biot stress reduces to the Terzaghi effective stress, meaning that Terzaghi's effective stress is the stress conjugated to the strain in the limit of incompressible solid grains:

$$\mathrm{d}\sigma' = \mathrm{d}\sigma - \mathrm{d}p_l \tag{29}$$

Starting from $\mathrm{d}F = p'\,\mathrm{d}\epsilon_v + q\,\mathrm{d}\epsilon_q$ for soils:

$$\begin{pmatrix} \mathrm{d}\epsilon_v \\ \mathrm{d}\epsilon_q \end{pmatrix} = \begin{pmatrix} \dfrac{1}{K(p',q)} & \dfrac{1}{C(p',q)} \\ \dfrac{1}{C(p',q)} & \dfrac{1}{3G(p',q)} \end{pmatrix} \begin{pmatrix} \mathrm{d}p' \\ \mathrm{d}q \end{pmatrix} \tag{30}$$

with

$$\frac{\partial}{\partial q}\left(\frac{1}{K}\right) = \frac{\partial}{\partial p'}\left(\frac{1}{C}\right) \quad ; \quad \frac{\partial}{\partial p'}\left(\frac{1}{3G}\right) = \frac{\partial}{\partial q}\left(\frac{1}{C}\right) \tag{31}$$

The case of unsaturated porous materials is more complex since two fluid pressures and the interfaces' energy has to be considered. This case will not be treated here.

However, it is worth noting that a Bishop like stress variable [Bis59] appears as the work conguate of the strain tensor. Interested readers are referred to [CPV10] for a detailed discussion of the unsaturated case.

As it appears from the previous derivations, constitutive relations introduce materials parameters (and fundamental assumptions) that have to be determined or assessed experimentally. As an illustration, Figure 4 shows the results of an unjacketed ($\sigma = p_l$) test on a limestone, as reported by [Cou04]. Table 1 shows more generally the order of magnitude of poroelastic properties for different materials, as reported by [Cou04]. It appears that the Biot coefficient is larger in materials with relatively low bulk modulus. Regarding the nonlinearity of the behaviour, Figure 5 shows the results of an unjacketed test on a sandstone, showing the linearity of the behaviour of the solid phase (left), while the estimation of the material's (drained) bulk modulus clearly shows a nonlinear behaviour (right). The consistency of the results from two experiments at two distinct fluid pressures show that the bulk modulus depends on the Biot effective stress σ'.

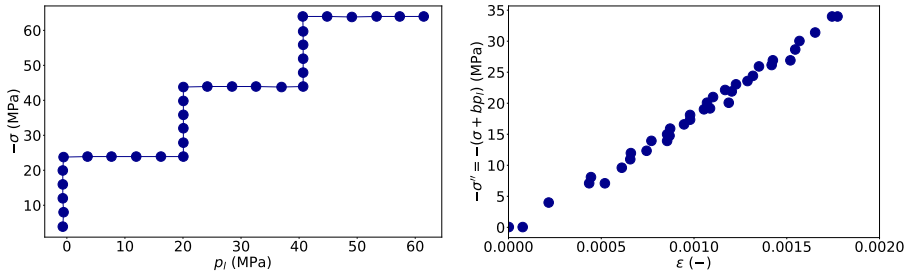

Figure 4: Unjacketed test on a limestone ($K_s = 52.7$ GPa): stress path in terms of total stress σ as a function of fluid pressure p (left) and material response in terms of Biot stress σ" as a function of volumetric deformation ϵ, after [Cou04].

Table 1: Order of magnitude of poroelastic properties for different materials, after [Cou04].

Material	ϕ (%)	K (MPa $\times 10^3$)	b ($-$)	N (MPa $\times 10^3$)
Cement paste	40–63	15–2	0.07–0.37	1170–20
Mortar	27–40	15–3	0.04–0.35	2340–40
Bone	5	12	0.14	160
Granites	1–2	25–35	0.22–0.44	280–370
Marble	2	40	0.20	280
Sandstones	2–26	4.6–13	0.69–0.85	$\sim$17
Limestones	4–29	5–39	0.34–0.88	100–400

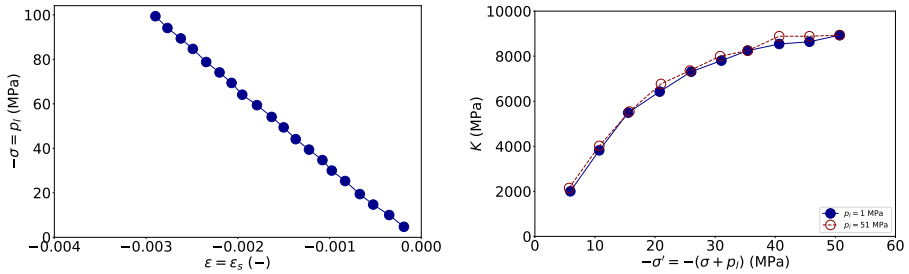

Figure 5: Experimental confirmation of the semi-linear hypothesis: linearity of the solid matrix (left) and non-linearity of the skeleton of a sandstone, after [BBV+01].

2.2.5 Beyond reversibility

In the following, we will consider that irreversible processes are at play, essentially in the form of plastic deformations. We will consider that strains and porosity can be partitioned into elastic and plastic parts:

$$\boldsymbol{\epsilon} = \boldsymbol{\epsilon}^e + \boldsymbol{\epsilon}^p \tag{32}$$

$$\phi = \phi^e + \phi^p \tag{33}$$

Coming back to the Clausius-Duhem inequality, we can write:

$$\mathrm{d}D = \sigma_{ij}\,\mathrm{d}\epsilon_{ij} + p_l\,\mathrm{d}\phi - \mathrm{d}F \geq 0 \tag{34}$$

In this case, the free energy of the solid skeleton is expressed as a function of the elastic strain and the elastic porosity:

$$\mathrm{d}F = \sigma_{ij}\,\mathrm{d}\epsilon^e_{ij} + p_l\,\mathrm{d}\phi^e \tag{35}$$

This time, $\mathrm{d}D \neq 0$ and the dissipation is expressed as:

$$\mathrm{d}D = \sigma_{ij}\,\mathrm{d}\epsilon^p_{ij} + p_l\,\mathrm{d}\phi^p \geq 0 \tag{36}$$

This means that the free energy changes only when the elastic strain or the elastic porosity change. The plastic strain and plastic porosity do not contribute to the free energy, but they do contribute to the dissipation. Another important point is that the stress and fluid pressure are work conjugated to the elastic strain and elastic porosity, respectively. In other words, changing the value of the total stress requires changing the elastic strain, and changing the fluid pressure (actually, the mechanical contribution of the fluid pressure to the solid skeletong) requires changing the elastic porosity.

The remaining ingredients necessary to define the elastoplastic constitutive equations are:

- the yield function,

- the flow rule
- and the hardening law.

The yield function, usually denoted $f(\sigma, p_l, \dots)$ is a scalar function of the stress and fluid pressure, which defines the boundary of the elastic domain in the generalised stress space. This boundary is called the yield surface and corresponds to null values of the yield function, i.e. $f = 0$. By convention, when the yield function is negative, the material behaves elastically; when it is zero, plastic deformation occurs. The flow rule defines how the plastic strain and plastic porosity evolve when the plastic mechanism is activated. In the case of hardening plasticity, the hardening law defines how the location of the yield surface evolves with plastic deformation and plastic porosity. Interested readers are referred to [Cou10] to go further. Another important milestone is the work on hyperplasticity due to [HP06].

It is worth mentionning that the yield function can be expressed in terms of the Terzaghi effective stress. This is actually usually the case for geomaterials. Figure 6 shows the experimental validation of a yield function expressed in terms of Terzaghi stress for a limestone whose Biot coefficient is $b = 0.63$, as reported by [VBPF98] and cited by [Cou10]. Yield points at various levels of stresses and fluid pressures nicely align when plotted as a function of the Terzaghi effective stress (that is with the Biot coefficient $b = 1$), showing that the material yields following a criterion based on Terzaghi's stress even if its elastic behaviour clearly follows a Biot stress with a b coefficient much lower than unity.

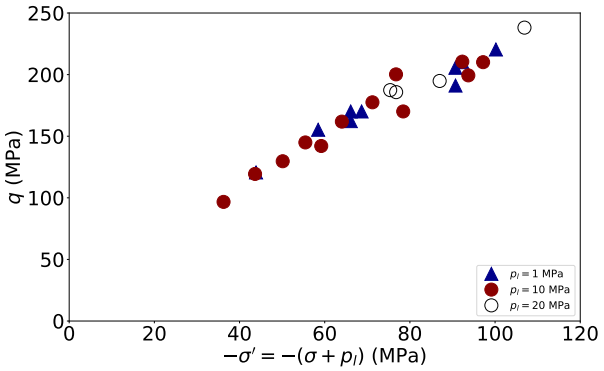

Figure 6: Experimental validation of yield function expressed in terms of Terzaghi stress for a limestone with $b = 0.63$, data from [VBPF98], cited by [Cou10].

2.3 Thermoporoelasticity and beyond

2.3.1 Thermoporoelasticity: a brief overview

Thermoporoelasticity is a field of study that combines the principles of thermodynamics, poroelasticity, and mechanics to understand the behavior of porous materials under thermal and mechanical loads. It is particularly relevant in geotechnical engineering, where the interaction between soil, fluids, and thermal effects plays a crucial role in various applications such as geothermal energy extraction, underground storage, and construction on or within the ground.

Thermoporoelasticity considers the coupled effects of temperature changes, pore fluid pressure, and mechanical stresses on the deformation and flow behavior of porous media. The governing equations typically involve the balance of mass, momentum, and energy, along with constitutive relations that describe the material's response to these coupled effects.

Considering non-isothermal evolutions, the free energy of the solid skeleton can be expressed as a function of the strain, the porosity, and the temperature:

$$\mathrm{d}F = \boldsymbol{\sigma} : \mathrm{d}\boldsymbol{\epsilon} + p_l \,\mathrm{d}\phi - \mathcal{S}_s \,\mathrm{d}T \tag{37}$$

where $\mathcal{S}_s$ is the entropy of the solid skeleton.

The case of non-isothermal processes introduces additional complexity to the constitutive equations, that need to account for the thermal coupling and the thermal effects on the material properties. If one want to obtain linear constitutive equations, the free energy of the skeleton, assuming small deformation and small change in temperature, has to write as follows:

$$F = \frac{1}{2}\lambda\epsilon_v^2 + \mu\epsilon_{ij}\epsilon_{ij} + \frac{1}{2}K_\phi\Delta\phi^2 + K_\psi\epsilon_v\Delta\phi - B_s\epsilon_v\Delta T - B_\psi\Delta T\Delta\phi - \frac{1}{2}m_\alpha\Delta T^2 \tag{38}$$

The stress-strain relations are then given by:

$$\sigma_{ij} = \left(K_\alpha\epsilon_v + K_\psi\Delta\phi - B_s\Delta T\right)\delta_{ij} + 2G\epsilon_{ij} \tag{39}$$

and the porosity change:

$$p - p_l = -(1-\phi)K_\phi\Delta\phi - (1-\phi)K_\psi\epsilon_v + (1-\phi)B_\psi\Delta T \tag{40}$$

For the record, the constitutive equation of the liquid phase can be given by:

$$p_l = -K_l\epsilon_l + B_f\Delta T_l \tag{41}$$

For an ideal porous medium, i.e. when the solid phase is homogeneous and isotropic, the constitutive equations can be simplified:

$$\epsilon_v = -\frac{p}{K} + \beta_s\Delta T \tag{42}$$

$$\Delta\phi = -\frac{p - p_l}{(1-\phi)K_\phi} \tag{43}$$

$$s_s = -\beta_s p + m_s \Delta T \tag{44}$$

where s_s is the entropy of the solid skeleton, β_s is the thermal expansion coefficient of the solid skeleton, and m_s is the thermal capacity of the solid skeleton.

2.3.2 Beyond reversibility

As in the isothermal case, considering irreversible processes is generally done by introducing plastic deformations and plastic porosity. A complete elastoplastic model, including thermal effects, would then require the definition of a yield function, a flow rule, and a hardening law. Insights will be provided in the following sections.

2.4 Lagrangian porosity and multiphysics couplings

Before going further, its is worth defining what is meant by multiphysics couplings in the context of THM behaviour. In this work, we will consider that the mechanical, thermal and hydraulic behaviours of geomaterials are coupled. The coupling between these three behaviours is illustrated in Figure 7. These couplings do not have the same nature, and they can be classified as follows:

- Direct couplings: when the intrinsic variable of one behaviour enters the balance equations of another behaviour. For instance, the deformation of the solid skeleton (mechanical behaviour) affects the pore volume and thus the mass balance of water (hydraulic behaviour).
- Indirect couplings: when the intrinsic variable of one behaviour enters the constitutive equations of another behaviour through material parameters. For instance, porosity changes (mechanical behavior) affect the permeability of the porous material, which enters the constitutive equation if Darcy's law is considered (hydraulic behaviour).

As we will see hereafter, some of these couplings can be decoupled or at least simplified by using lagrangian quantities, such as the lagrangian porosity ϕ.

Even if we assume small deformations, the porosity of a porous material is not constant during the deformation process. The change in porosity is related to the change in pore volume. The lagrangian porosity ϕ is defined as the ratio of the current pore volume to the initial volume of the porous material, as given by equation (4). Alternatively, the eulerian porosity n is defined as the ratio of the current pore volume to the current total volume of the porous material, as given by equation (2).

Distinguishing these two measures can prove practical and efficient. As demonstrated by [Cou07, CPV10], introducing a lagrangian degree of saturation is a more appropriate measure of the pore volume saturated by water than its eulerian counterpart. This is because the lagrangian saturation accounts for the initial volume of the porous material, which is not affected by the deformation process. As a result, changes in

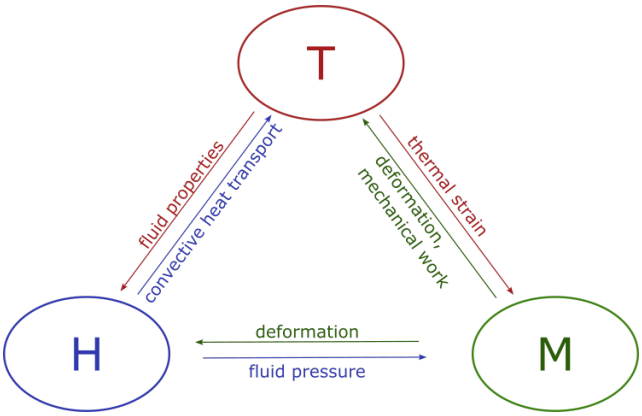

Figure 7: Illustration on interrelationships between mechanical, thermal and hydraulic behaviours in geomaterials.

saturation are only due to the process of water infiltration or drainage, rather than changes in the pore volume due to deformation. In this case, the use of a lagrangian quantity allows for a convenient decoupling of the constitutive equations.

The thermal expansion of a porous solid is another example where the lagrangian porosity and the eulerian porosity will not provide similar responses. When a porous solid is heated, it expands, and the pore volume increases as well. This is illustrated in Figure 8. How does the porosity evolve?

Considering an isotropic behaviour and refering to [Cou04, Che16], it comes:

$$p - p_0 = K\,\epsilon_v - b\,(p_w - p_{w,0}) - 3\alpha\,K\,(T - T_0) \tag{45}$$

$$\phi - \phi_0 = b\,\epsilon_v + \frac{p_w - p_{w,0}}{N} - 3\alpha_\phi\,(T - T_0) \tag{46}$$

and recalling the relation with microscopic properties:

$$\epsilon_v = (1 - \phi_0)\,\epsilon_s + \phi - \phi_0 \tag{47}$$

$$b = 1 - \frac{K}{K_s}; \qquad \frac{1}{N} = \frac{b - \phi_0}{K_s} \tag{48}$$

$$\alpha = \alpha_s; \qquad \alpha_\phi = \alpha\,(b - \phi_0) \tag{49}$$

Let's consider a thought experiment where a drained and stress-free porous solid is heated by a temperature increment $\Delta T = 10\,\mathrm{K}$. The initial void ratio is $e_0 = 1.0$ and the initial porosity is $\phi_0 = 0.5$. The linear thermal expansion of the material is $\alpha = \frac{1}{3} \times 10^{-2}\ \mathrm{K}^{-1}$. The final stress and liquid pressure are both zero.

The final volumetric strain is:

$$\epsilon_v = 3\,\alpha\Delta T = 0.1$$

and the porosity change is:

$$\Delta\phi = b\,\epsilon_v - 3\,\alpha_\phi \Delta T = 3\,\alpha\phi_0\,\Delta T = 0.05$$

The final lagrangian porosity is then $\phi = 0.55$.

As can be seen in Figure 8, the porous material subjected to a temperature change undergoes a homothetic deformation, affecting in the same proportion both the solid phase and the porous volume. As a consequence, the eulerian porosity of the heated material is given by:

$$n = \frac{V_v}{V} = \frac{V_{v,0}}{V_{s,0}} = n_0 = 0.5$$

Similarly, the void ratio is reads:

$$e = \frac{V_{v,0}}{V_{s,0}} = e_0 = 1$$

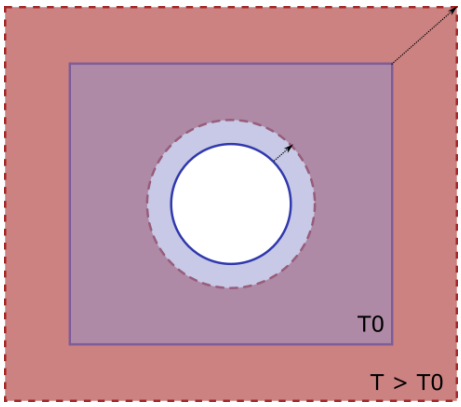

Figure 8: Illustration of the thermal expansion of a solid volume containing a circular void inclusion. The porous solid occupies the scetion in blue at a reference temperature T_0. When the temperature increases to T, the solid expands and the void inclusion expands as well. The lagrangian porosity ϕ increases, while the eulerian porosity n remains constant.

As a general recommandation, it is advised to use both porosities, depending on the context. Eulerian porosity is more convenient when dealing with indirect couplings, such a porosity dependent permeability or thermal conductivity. The lagrangian porosity is more convenient when dealing with direct couplings, such as the those induced by changes in pore volume due to mechanical deformation. Since the lagrangian porosity tracks the deformation of the porous network, its use allows to solve the mass balance of the fluid filling the pores in a conservative manner. Interested readers are referred to [MDG+20] for a discussion on the use of both porosities in the context of a study of bituminous materials.

Now that the thermodynamic framework has been presented, we will review the thermo-hydro-mechanical behaviour of geomaterials, starting with a brief review of what is known about the THM behaviour of soils, before discussing the constitutive models that have been developed to describe this behaviour, focusing mainly on the underlaying assumptions.

3 THM behaviour

3.1 What we know: a brief review

3.1.1 Mechanical behaviour

This section reviews the influence of temperature on the hydromechanical behaviour of geomaterials. Numerous studies have examined how thermal effects alter the mechanical properties of soils. For coarse-grained soils, temperature changes typical of geotechnical applications generally have a limited impact, provided that pore water phase changes do not occur. However, exceptions exist; for instance, [BG13] reported "intrinsic creep" in granular glass bead columns subjected to thermal cycling.

Fine-grained soils exhibit more pronounced thermal effects. Volumetric responses differ significantly between over-consolidated and normally or lightly consolidated soils [CL04, HB90a, SDC02]. Over-consolidated soils tend to show reversible volume changes under temperature cycles, while normally consolidated soils experience irreversible deformations, a phenomenon known as thermal consolidation. After heating and cooling, a normally consolidated clay behaves as if it were over-consolidated. This effect may be leveraged to enhance the mechanical properties of soft clays [HST$^+$23], and should be incorporated into thermo-mechanical constitutive models for clays.

Temperature effects on soil shear strength have also been widely studied, with findings ranging from strength increases to decreases or negligible changes. Recent reviews summarise these varied results for clays [HST$^+$23].

The intrinsic creep observed by [BG13] is attributed to the propagation of temperature gradients, causing non-uniform compaction, especially under rapid thermal cycles. This has implications for the long-term performance of geothermal structures. The impact of thermal cycling on pile settlement has been investigated through small-scale tests in dry sand [NTP17, YTPH14a], saturated clay [NWG$^+$20, NNPT23], and centrifuge modelling [NSGL14, NFGJ21]. These studies generally report an accumulation of irreversible settlement with repeated cycles (ratcheting), with most settlement occurring during the first cycle. The extent of irreversible settlement increases with mechanical load and diminishes when the load is well below the pile's bearing capacity. If thermally induced pile deformation is accommodated by increased shaft friction, deformation remains reversible [PS14]. This topic is further discussed in the applications section 4.2.

Irreversible settlements observed in some experiments raise questions about the thermal behaviour of soil-structure interfaces. Yavari and colleagues [YTPH16] con-

ducted direct shear tests on sand, clay, and clay–concrete interfaces at temperatures between 5 and 40 °C, finding negligible temperature effects on interface properties within this range.

In addition to thermal cycling, the time-dependent behaviour of soils —such as strain rate effects and creep— is also temperature dependent [LM96]. As noted by [BG13], the rate of temperature change can influence soil response due to heat diffusion and resulting non-uniform deformations. More complex couplings may also introduce rate effects at the material point.

3.1.2 Hydraulic behaviour

Temperature effects on the hydraulic properties of soils can be direct or indirect (e.g., via temperature-induced porosity changes). Direct temperature effects on permeability are best addressed by using intrinsic permeability (dimension $[L]^2$) rather than hydraulic conductivity ($[L][T]^{-1}$), since intrinsic permeability is largely unaffected by temperature, while hydraulic conductivity depends on fluid properties, notably viscosity, which is temperature sensitive. In practice, it is recommended to use intrinsic permeability and a temperature-dependent fluid viscosity, which is generally well characterised. If only hydraulic conductivity is available, its temperature dependence can be deduced from the relationship:

$$k = \frac{\rho_f \, g}{\mu_f} k_{int} \tag{50}$$

where k is hydraulic conductivity, ρ_f and μ_f are the fluid density and viscosity, and k_{int} is intrinsic permeability.

The permeability of unsaturated geomaterials has been studied for decades, especially in oil engineering [EMS$^+$20]. Even over large temperature ranges (20–200 °C), in [EMS$^+$20], the authors found that temperature does not affect oil/water relative permeability in consolidated sand packs. In [YWC$^+$12], the authors confirmed that temperature-induced changes in unsaturated hydraulic conductivity of bentonite are due to water viscosity changes at high suction, and to both viscosity and microstructural changes at low suction. In the low suction range, where clay is softer, both direct (thermo-hydraulic) and indirect (thermo-mechanical) effects are present.

Temperature also affects the water retention properties of geomaterials. In the capillary regime, these effects mainly arise from the temperature dependence of interfacial tension. Osmotic and adsorptive contributions are also temperature dependent, but in typical temperature ranges (below 100 °C), these effects only slightly alter the water retention curve [Olc02]. However, the authors of [PHSM23] report appreciable effects at higher temperatures.

Indirectly, temperature-induced deformations alter soil microstructure, leading to changes in hydraulic properties.

3.1.3 Thermal behaviour

Heat transport in geomaterials is complex, but conduction is usually the dominant mode, along with heat advection by fluid flow. Convective and radiative effects are generally neglected due to the presence of the solid walls delimiting the extent of the pore network and the relatively low temperatures, respectively.

A key THM phenomenon in soils and rocks is thermal pressurisation, arising from the mismatch between the thermal expansion coefficients of water and soil minerals —water expands almost ten times more than typical soil solids. In the laboratory, this is observed during undrained experiments [BHPP91, BGD$^+$21] and can lead to tensile failure [BDG$^+$22]. In the field, thermal pressurisation is significant in fast landslides and must be considered [VVT07, SF09, PA10]. Here, water flow (driven by pore pressure gradients and permeability) and the rate of temperature increase interact.

3.2 Constitutive modelling

3.2.1 THM constitutive models

Many constitutive models have been proposed to describe the THM behaviour of soils. The first, based on an extension of the Modified Cam-clay model, was developed by Hueckel and co-authors [HB90b, HB90a]. Numerous subsequent models also use an elastoplastic framework with a temperature-dependent yield surface [ABBP09, CSD00, GTCA01, LN09]. Reviews can be found in [SCAB93, HPTC13]. Adaptations include two-surface plasticity and kinematic hardening for cyclic behaviour [HPC$^+$14, HPTC16].

These models are essentially empirical and focus on modelling thermal consolidation as discussed above. [BHV$^+$17] proposed an approach based on molecular simulations and upscaling to explain, from an energetic viewpoint, how irreversible deformation may be triggered by temperature changes.

Creep and strain rate effects have been incorporated in a model by [LLC08]. Indirect couplings, such as thermally induced changes in hydraulic properties via microstructural changes, can be modelled using the Kozeny-Carman equation [Car37, Koz25] or micro-macro approaches [AP13, PA13].

3.2.2 Thermal properties

Thermal properties (heat capacity, thermal conductivity, thermal expansion) are key for evaluating the THM behaviour of geostructures. In numerical simulations, it is useful to update these properties based on the current state (porosity, water content, or degree of saturation). This is straightforward for heat capacity, but more complex for thermal conductivity, which depends on microstructure.

Neglecting the gas phase, the volumetric heat capacity C of an unsaturated geomaterial is:

$$C = (1 - n)\rho_s c_s + nS_w \rho_w c_w \tag{51}$$

where ρ_s and ρ_w are solid and water densities, c_s and c_w are their specific heat capacities, and n is porosity.

Several models exist for soil thermal conductivity. A simple arithmetic average is sometimes used, but Johansen's model [Joh75], based on a weighted geometric average, is also common:

$$\lambda = \prod_{\alpha} (\lambda_{\alpha})^{f_\alpha} \tag{52}$$

where λ_α is the thermal conductivity of phase α, occupying a volume fraction f_α. For unsaturated soils, Johansen proposed:

$$\lambda(S_r) = (\lambda_{sat} - \lambda_{dry})k(S_r) + \lambda_{dry} \tag{53}$$

where λ_{sat} and λ_{dry} are the saturated and dry conductivities, and $k(S_r)$ is a function of the degree of saturation, fitted to experimental data.

Regarding experimental observations, [GG01] showed that, for granular media, adding water greatly increases thermal conductivity at low water contents, as water forms menisci at grain contacts, enhancing heat transfer. In the case of a finer (and natural) soil, Figure 9 shows the thermal conductivity of an intact loess from northern France as a function of degree of saturation [NHP$^+$17]. The data collapse on a master curve, indicating that water content controls thermal conductivity in the unsaturated range, and the variation is approximately linear.

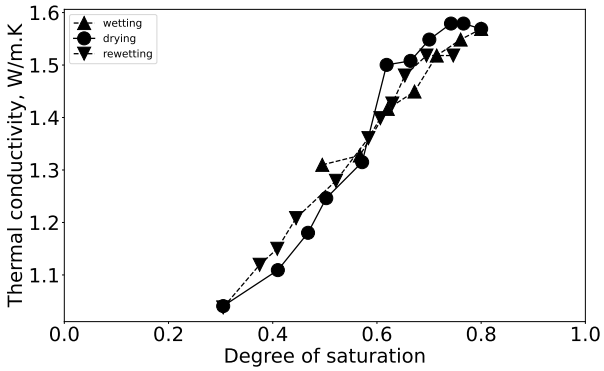

Figure 9: Thermal conductivity of loess from northern France as a function of the degree of saturation of water (adapted from [NHP$^+$17]).

The choice between models such as those above depends on assumptions about heat flow within soil constituents (series, parallel, or mixed), which in turn depends on microstructure and liquid phase distribution. As an illustration of a two-step homogenisation approach, readers are refered to [GGH$^+$07], who proposed a two-scale homogenisation approach for claystone.

Equations like (52) and (53), and other microstructure-based models, readily account for porosity or microstructural changes, facilitating the modelling of coupled effects on thermal properties. For a critical review of soil thermal conductivity models, see [DML15].

3.3 Coupled behaviour vs simplified strategies

In academic contexts, advanced approaches have been developed for specific problems such as nuclear waste disposal or CO_2 geological storage. However, in engineering practice, numerical approaches to THM problems rarely employ fully coupled (monolithic) solutions of the governing equations or advanced constitutive models.

It has been shown that simplified approaches can be used under certain conditions, especially when geotechnical analysis software does not support thermal analyses. For example, Yavari and co-authors [YTPH14b] simulated the mechanical behaviour of thermal piles by imposing the thermally induced volumetric strain on the pile body as a boundary condition. Using this basic decoupling method, the authors obtained satisfactory results for pile head displacement and axial load distribution along the pile length. Of course, this simplified approach has strong limitations, as no temperature change is calculated within the soil mass. In particular, the good performance of this approach suggests that the volumetric expansion of the soil around the pile does not play a significant role in pile behaviour, and that the radial expansion of the pile may be sufficient to approximate the behaviour of the pile-soil interface. It should also be noted that decoupling strategies can lead to significant errors in numerical results, as shown by [PP11a] in the case of THM simulation of CO_2 injection in a geological reservoir.

Simplified engineering tools based on extending the load-transfer approach to thermal problems have been developed [LNV06, RSL20, SP22] and have proven efficient for the thermo-mechanical analysis of thermoactive piles and pile groups. For the cyclic behaviour of thermal piles, simplified models that avoid explicit modelling of every cycle have been developed to predict long-term behaviour [PCC19, PS14]. These simplified strategies are useful in practice but will not be further discussed in this chapter.

4 Applications in energy geotechnics

Engineering applications involving THM behaviour of geomaterials are numerous and varied [SAE+22]. This section briefly reviews some key examples.

4.1 Soil-atmosphere interaction

Although not directly related to energy geotechnics, modelling soil-atmosphere interactions is included here because the numerical tools and models used often originate from THM studies in the field of geotechnics. Soil-atmosphere interaction refers to

humidity and heat exchanges between the soil surface and the environment of geostructures. Such interactions have been considered for decades in applications related to slope stability [TC20], dyke and embankment design [Cui22], and the effects of drought on structures built on expansive clays [HGCV12]. A recent review is provided in [ECP+17]. Numerical modelling of these interactions is complex, as it must account for coupled THM balance equations, vapour-liquid phase changes, hydromechanical effects of vegetation [BLB21], non-trivial and time-varying boundary conditions, and challenges in establishing an equilibrated and representative initial state. For the latter, readers are referred to spin-up strategies discussed in [RSB21, TC20].

4.2 Geothermal structures

Thermo-active geostructures have been used for decades, with the first thermal piles installed in Austria in the 1980s, but their use has accelerated since the early 2000s [BWAS+09, LMV03]. Today, other structures such as diaphragm walls and tunnel linings are also thermo-activated [BDP16, DLT+19]. In numerical modelling, various levels of complexity are considered for the thermal boundary conditions imposed on thermal piles. The simplest approaches use a uniform temperature field corresponding to the average of the ingoing and outgoing heat carrier fluid temperatures. More sophisticated approaches explicitly model fluid flow within the exchanger tubes embedded in the piles, at the cost of increased computational effort. This cost can be mitigated by machine learning techniques, as shown in [MNB18] for the thermal design of thermo-active piles.

In practice, thermal design often receives more attention than the mechanical problem. Constitutive models used in geothermal structure analysis are often relatively simple, as the relevant temperature range is typically between 0 and 50 °C, making thermal consolidation of normally consolidated clays unlikely. As previously mentioned, the cyclic behaviour of the soil-structure interface may be important for long-term assessment. The authors of [BWLBFS22] discussed the significant role of available shaft resistance and the ratio of mobilised friction on settlement accumulation, which mainly occurs during the first cooling due to thermal shrinkage of the pile radius. Incremental settlement per cycle then tends to vanish as the number of cycles increases. This observation, obtained from thermo-mechanical finite element simulations, coincides with experimental results reported in Section 3.1.1.

4.3 Radioactive waste disposals

Accounting for THM behaviour is essential in the analysis of radioactive waste disposals. The literature is extensive and covers many physical aspects, including two-phase flow in swelling clays, thermal pressurisation, and plastic or damage mechanics for the host rock. This application has been studied for decades, and abundant experimental data from laboratory tests, small-scale experiments, and full-scale field experiments are available. These data are highly valuable for validating numerical tools for THM modelling of geomaterials [SGR+20] and for THM constitutive models that account

for complex couplings.

4.4 CO_2 geological storage and deep geothermal energy

Modelling CO_2 geological storage and deep geothermal energy production at the reservoir scale require geomechanics solvers that work efficiently. These applications may require specific developments to simulate multiphase flow in reservoirs, which may be fractured at various scales [LPCN21, LCNP24]. Thermal effects are significant in both deep geothermal energy production and CO_2 geo-storage [VR17]. In some cases, additional couplings, such as chemical interactions in CO_2 storage, are necessary. These couplings are not always implemented in THM codes, so low-coupling strategies (such as sequential coupling between geomechanical codes and reactive transport software) are commonly used. A discussiong on coupling issues and their stabilisation is provided in [PP11a, PP11b].

5 Conclusions

In summary, thermo-hydro-mechanical (THM) couplings are fundamental to understanding and predicting the behaviour of geomaterials in a wide range of geotechnical and energy-related applications. This chapter has outlined the thermodynamic framework underpinning THM processes, reviewed the main experimental observations regarding mechanical, hydraulic, and thermal responses of geomaterials, and discussed constitutive modelling strategies from linear poroelasticity to advanced elastoplastic and thermoporoelastic models. The importance of distinguishing between direct and indirect couplings, as well as the practical use of Lagrangian and Eulerian porosities, has been highlighted for accurate modelling.

Applications in energy geotechnics —such as geothermal structures, radioactive waste disposal, and CO_2 storage— demonstrate the necessity of accounting for THM effects to ensure safety, durability, and performance. While fully coupled numerical approaches provide the most rigorous solutions, simplified strategies are often adopted in engineering practice, balancing complexity and practicality.

Ultimately, the integration of THM couplings into constitutive models and numerical simulations remains a key challenge and opportunity for advancing both fundamental research and engineering practice in the context of the energy transition.

References

[ABBP09] H. M. Abuel-Naga, D. T. Bergado, A. Bouazza, and M. Pender. Thermomechanical model for saturated clays. *Géotechnique*, 59(3):273, 2009.

[AP13] C. Arson and J. M. Pereira. Influence of damage on pore size distribution and permeability of rocks. *International Journal for Numerical and Analytical Methods in Geomechanics*, 37(8):810–831, 2013.

[BBV+01] E. Bemer, M. Boutéca, O. Vincké, N. Hoteit, and O. Ozanam. Poromechanics: From Linear to Nonlinear Poroelasticity and Poroviscoelasticity. *Oil & Gas Science and Technology*, 56(6):531–544, 2001.

[BDG+22] P. Braun, P. Delage, S. Ghabezloo, B. Chabot, N. Conil, and M. Vu. Inducing Tensile Failure of Claystone Through Thermal Pressurization in a Novel Triaxial Device. *Rock Mechanics and Rock Engineering*, 55(7):3881–3899, 2022.

[BDP16] M. Barla, A. Di Donna, and A. Perino. Application of energy tunnels to an urban environment. *Geothermics*, 61:104–113, 2016.

[BG13] B. Blanc and J.-C. Géminard. Intrinsic creep of a granular column subjected to temperature changes. *Phys. Rev. E*, 88(2):22201, 2013.

[BGD+21] P. Braun, S. Ghabezloo, P. Delage, J. Sulem, and N. Conil. Thermo-Poro-Elastic Behaviour of a Transversely Isotropic Shale: Thermal Expansion and Pressurization. *Rock Mechanics and Rock Engineering*, 54(1):359–375, 2021.

[BHPP91] G. Baldi, T. Hueckel, A. Peano, and R. Pellegrini. Developments in modelling of thermo-hydro-mechanical behaviour of Boom clay and clay-based buffer materials, Vol. 1 and 2, EUR 13365/1 and 13365/2. Technical report, Nuclear Science and Technology, Commission of the European Communities, 1991.

[BHV+17] L. Brochard, T. Honório, M. Vandamme, M. Bornert, and M. Peigney. Nanoscale origin of the thermo-mechanical behavior of clays. *Acta Geotechnica*, 12(6):1261–1279, 2017.

[Bis59] A. W. Bishop. The principle of effective stress. *Teknisk Ukeblad*, 106(39):859–863, 1959.

[BLB21] D. Boldrin, A. K. Leung, and A. G. Bengough. Hydro-mechanical reinforcement of contrasting woody species: A full-scale investigation of a field slope. *Géotechnique*, 71(11):970–984, 2021.

[Bra06] H. Brandl. Energy foundations and other thermo-active ground structures. *Géotechnique*, 56(2):81–122, 2006.

[BVP12] L. Brochard, M. Vandamme, and R. Pellenq. Poromechanics of microporous media. *Journal of the Mechanics and Physics of Solids*, 60(4):606–622, 2012.

[BWAS+09] P. J. Bourne-Webb, B. Amatya, K. Soga, T. Amis, C. Davidson, and P. Payne. Energy pile test at Lambeth College, London: Geotech-

nical and thermodynamic aspects of pile response to heat cycles. *Géotechnique*, 59(3):237–248, 2009.

[BWLBFS22] P. J. Bourne-Webb, A. Lupattelli, T. M. Bodas Freitas, and D. Salciarini. The influence of initial shaft resistance mobilisation in the response of seasonally, thermally-activated pile foundations in granular media. *Geomechanics for Energy and the Environment*, 32:100299, 2022.

[Car37] P. C. Carman. Fluid flow through granular beds. *Transactions-Institution of Chemical Engineeres*, 15:150–166, 1937.

[Che16] A. H. Cheng. *Poroelasticity*. Springer, 2016.

[CL04] C. Cekerevac and L. Laloui. Experimental study of thermal effects on the mechanical behaviour of a clay. *International Journal for Numerical and Analytical Methods in Geomechanics*, 28(3):209–228, 2004.

[Cou04] O. Coussy. *Poromechanics*. John Wiley & Sons, Chichester, 2004.

[Cou07] O. Coussy. Revisiting the constitutive equations of unsaturated porous solids using a Lagrangian saturation concept. *International Journal for Numerical and Analytical Methods in Geomechanics*, 31(15):1675–1694, 2007.

[Cou10] O. Coussy. *Mechanics and Physics of Porous Solids*. Wiley, 2010.

[CPV10] O. Coussy, J. M. Pereira, and J. Vaunat. Revisiting the thermodynamics of hardening plasticity for unsaturated soils. *Computers and Geotechnics*, 37(1-2):207–215, 2010.

[CSD00] Y. J. Cui, N. Sultan, and P. Delage. A thermomechanical model for saturated clays. *Canadian Geotechnical Journal*, 37(3):607–620, 2000.

[Cui22] Y. J. Cui. Soil–atmosphere interaction in earth structures. *Journal of Rock Mechanics and Geotechnical Engineering*, 14(1):35–49, 2022.

[Del10] P. Delage. A microstructure approach to the sensitivity and compressibility of some Eastern Canada sensitive clays. *Géotechnique*, 60(5):353–368, 2010.

[DLT+19] S. Dong, X. Li, A. M. Tang, J. M. Pereira, V. T. Nguyen, P. Che, and Z. Xiong. Thermo-mechanical behavior of energy diaphragm wall: Physical and numerical modelling. *Applied Thermal Engineering*, 146:243–251, 2019.

[DML15] Y. Dong, J. S. McCartney, and N. Lu. Critical Review of Thermal Conductivity Models for Unsaturated Soils. *Geotechnical and Geological Engineering*, 33(2):207–221, 2015.

[DWG08] H. R. Dingle, D. J. White, and C. Gaudin. Mechanisms of pipe embedment and lateral breakout on soft clay. *Canadian Geotechnical Journal*, 45(5):636–652, 2008.

[ECP+17] G. Elia, F. Cotecchia, G. Pedone, J. Vaunat, P. J. Vardon, C. Pereira, S. M. Springman, M. Rouainia, J. Van Esch, E. Koda, J. Josifovski, A. Nocilla, A. Askarinejad, R. Stirling, P. Helm, P. Lollino, and P. Osinski. Numerical modelling of slope–vegetation–atmosphere interaction: An overview. *Quarterly Journal of Engineering Geology and Hydrogeology*, 50(3):249–270, 2017.

[EMS+20] S. Esmaeili, J. Modaresghazani, H. Sarma, T. Harding, and B. Maini. Effect of temperature on relative permeability – Role of viscosity ratio. *Fuel*, 278:118318, 2020.

[GG01] J.-C. Géminard and H. Gayvallet. Thermal conductivity of a partially wet granular material. *Physical Review E*, 64(4):041301, 2001.

[GGH+07] C. Gruescu, A. Giraud, F. Homand, D. Kondo, and D. P. Do. Effective thermal conductivity of partially saturated porous rocks. *International Journal of Solids and Structures*, 44(3):811–833, 2007.

[GMV21] M. Gasc-Barbier, V. Merrien-Soukatchoff, and D. Virely. The role of natural thermal cycles on a limestone cliff mechanical behaviour. *Engineering Geology*, 293:106293, 2021.

[GTCA01] J. Graham, N. Tanaka, T. Crilly, and M. Alfaro. Modified Cam-Clay modelling of temperature effects in clays. *Canadian Geotechnical Journal*, 38(3):608–621, 2001.

[HB90a] T. Hueckel and G. Baldi. Thermoplasticity of saturated clays: Experimental constitutive study. *Journal of Geotechnical Engineering*, 116(12):1778–1796, 1990.

[HB90b] T. Hueckel and M. Borsetto. Thermoplasticity of saturated soils and shales: Constitutive equations. *Journal of Geotechnical Engineering*, 116(12):1765–1777, 1990.

[HGCV12] S. Hemmati, B. Gatmiri, Y. Cui, and M. Vincent. Thermo-hydro-mechanical modelling of soil settlements induced by soil-vegetation-atmosphere interactions. *Engineering Geology*, 139–140:1–16, 2012.

[HP06] G. T. Houlsby and A. M. Puzrin. *Principles of Hyperplasticity*. Springer London, London, 2006.

[HPC+14] P. Y. Hong, J. M. Pereira, Y. J. Cui, A. M. Tang, F. Collin, and X. L. Li. An elastoplastic model with combined isotropic–kinematic hardening to predict the cyclic behavior of stiff clays. *Computers and Geotechnics*, 62:193–202, 2014.

[HPTC13] P. Y. Hong, J. M. Pereira, A. M. Tang, and Y. J. Cui. On some advanced thermo-mechanical models for saturated clays. *International Journal for Numerical and Analytical Methods in Geomechanics*, 37(17):2952–2971, 2013.

[HPTC16] P. Y. Hong, J. M. Pereira, A. M. Tang, and Y. J. Cui. A two-surface plasticity model for stiff clay. *Acta Geotechnica*, 11(4):871–885, 2016.

[HST+23] H. J. M. Huancollo, F. Saboya, S. Tibana, J. S. McCartney, and R. Garske Borges. Thermal Triaxial Tests to Evaluate Improvement of Soft Marine Clay through Thermal Consolidation. *Geotechnical Testing Journal*, 46(3):20220154, 2023.

[Joh75] O. Johansen. *Varmeledningsevne Av Jordarter (Thermal Conductivity of Soils)*. PhD thesis, English Translation by US Army Corps of Engineers, University of Trondheim, Trondheim, Norway, 1975.

[Koz25] J. Kozeny. Über turbulentes Fließen bei glatten Wänden. *Zeitschrift für Angewandte Mathematik und Mechanik*, 5(3):244–250, 1925.

[LCNP24] A. C. Loyola, M. P Cordão Neto, and J. M. Pereira. An open-source numerical laboratory to assess the poromechanical behavior of fractured rocks. *Computers and Geotechnics*, 168:106127, 2024.

[LD13] L. Laloui and A. Di Donna. *Energy Geostructures: Innovation in Underground Engineering*. John Wiley & Sons, 2013.

[LLC08] L. Laloui, S. Leroueil, and S. Chalindar. Modelling the combined effect of strain rate and temperature on one-dimensional compression of soils. *Canadian Geotechnical Journal*, 45:1765–1777, 2008.

[LM96] S. Leroueil and M. E. S. Marques. Importance of strain rate and temperature effects in geotechnical engineering. In *Measuring and Modeling Time Dependent Soil Behaviour, Proc. of the ASCE Convention*, volume 61, pages 1–60, Washington, DC, USA, 1996.

[LMV03] L. Laloui, M. Moreni, and L. Vulliet. Comportement d'un pieu bifonction, fondation et échangeur de chaleur. *Canadian Geotechnical Journal*, 40(2):388–402, 2003.

[LN09] L. Laloui and M. Nuth. On the use of the generalised effective stress in the constitutive modelling of unsaturated soils. *Computers and Geotechnics*, 36(1-2):20–23, 2009.

[LNV06] L. Laloui, M. Nuth, and L. Vulliet. Experimental and numerical investigations of the behaviour of a heat exchanger pile. *International Journal for Numerical and Analytical Methods in Geomechanics*, 30(8):763–778, 2006.

[LPCN21] A. C. Loyola, J. M. Pereira, and M. N. Cordão Neto. General Statistics-Based Methodology for the Determination of the Geometrical and

Mechanical Representative Elementary Volumes of Fractured Media. *Rock Mechanics and Rock Engineering*, 54(4):1841–1861, 2021.

[LZ19] W. Liang and J. Zhao. Multiscale modeling of large deformation in geomechanics. *International Journal for Numerical and Analytical Methods in Geomechanics*, 43(5):1080–1114, 2019.

[MDG+20] G. Melot, P. Dangla, S. Granet, S. M'Jahad, J. Champenois, and A. Poulesquen. Chemo-Hydro-Mechanical analysis of Bituminized waste swelling due to water uptake: Experimental and model comparisons. *Journal of Nuclear Materials*, 536:152165, 2020.

[MNB18] N. Makasis, G. A. Narsilio, and A. Bidarmaghz. A machine learning approach to energy pile design. *Computers and Geotechnics*, 97:189–203, 2018.

[NFGJ21] C. W. W. Ng, A. Farivar, S. M. M. H. Gomaa, and F. Jafarzadeh. Centrifuge Modeling of Cyclic Nonsymmetrical Thermally Loaded Energy Pile Groups in Clay. *Journal of Geotechnical and Geoenvironmental Engineering*, 147(12), 2021.

[NHP+17] V. T. Nguyen, H. Heindl, J. M. Pereira, A. M. Tang, and J. D. Frost. Water retention and thermal conductivity of a natural unsaturated loess. *Géotechnique Letters*, 7(4):286–291, 2017.

[NNPT23] A. Nouri, A. Noorzad, J. M. Pereira, and A. M. Tang. Cyclically thermally-activated pile under combined axial/horizontal loads in clay. *Géotechnique Letters*, 13(1):41–47, 2023.

[NSGL14] C. W. W. Ng, C. Shi, A. Gunawan, and L. Laloui. Centrifuge modelling of energy piles subjected to heating and cooling cycles in clay. *Géotechnique Letters*, 4(4):310–316, 2014.

[NTP17] V. T. Nguyen, A. M. Tang, and J. M. Pereira. Long-term thermo-mechanical behavior of energy pile in dry sand. *Acta Geotechnica*, 12(4):729–737, 2017.

[NWG+20] V. T. Nguyen, N. Wu, Y. Gan, J. M. Pereira, and A. M. Tang. Long-term thermo-mechanical behaviour of energy piles in clay. *Environmental Geotechnics*, 7(4):237–248, 2020.

[Olc02] E. Olchitzky. *Couplage hydromécanique et perméabilité d'une argile gonflante non saturée sous sollicitations hydriques et thermiques : courbe de sorption et perméabilité à l'eau*. PhD thesis, Ecole des Ponts ParisTech, 2002.

[PA10] N. M. Pinyol and E. E. Alonso. Criteria for rapid sliding II. Thermo-hydro-mechanical and scale effects in Vaiont case. *Engineering Geology*, 114(3-4):211–227, 2010.

[PA13] J. M. Pereira and C. Arson. Retention and permeability properties of damaged porous rocks. *Computers and Geotechnics*, 48:272–282, 2013.

[PCC19] C. Pastén, E. Castillo, and S. H. Chong. Thermo-mechanical ratcheting in soil–structure interfaces. *Acta Geotechnica*, 14(5):1561–1569, 2019.

[PHSM23] T. A. Pham, A. Hashemi, M. Sutman, and G. M. Medero. Effect of temperature on the soil–water retention characteristics in unsaturated soils: Analytical and experimental approaches. *Soils and Foundations*, 63(3):101301, 2023.

[PP11a] M. Preisig and J. H. Prévost. Coupled multi-phase thermo-poromechanical effects. Case study: CO2 injection at In Salah, Algeria. *International Journal of Greenhouse Gas Control*, 5(4):1055–1064, 2011.

[PP11b] M. Preisig and J. H. Prévost. Stabilization procedures in coupled poromechanics problems: A critical assessment. *International Journal for Numerical and Analytical Methods in Geomechanics*, 35(11):1207–1225, 2011.

[PP13] G. Pijaudier-Cabot and J. M. Pereira, editors. *Geomechanics in CO_2 Storage Facilities*. ISTE-Wiley, 2013.

[PS14] C. Pasten and J. C. Santamarina. Thermally induced long-term displacement of thermoactive piles. *Journal of Geotechnical and Geoenvironmental Engineering*, 140(5):1–5, 2014.

[RSB21] C. Ross, G. Siemens, and R. Beddoe. Initialization of thermal models in cold and warm permafrost. *Arctic Science*, pages 1–33, 2021.

[RSL20] E. Ravera, M. Sutman, and L. Laloui. Load Transfer Method for Energy Piles in a Group with Pile–Soil–Slab–Pile Interaction. *Journal of Geotechnical and Geoenvironmental Engineering*, 146(6):04020042, 2020.

[SAE+22] J. C. Santamarina, A. Aftab, D. N. Espinoza, M. Dusseault, A. Gens, H. Hoteit, S. Kim, J. Y. Lee, L. Lei, G. Narsilio, J. M. Pereira, M. Sanchez, K. Soga, M. V. Villar, and M. Violay. Energy geoengineering. In *Proceedings of Twentieth International Conference on Soil Mechanics and Geotechnical Engineering (ICSMGE 2022): A Geotechnical Discovery down Under*, pages 95–117, Sydney, Australia, 2022.

[SCAB93] H. N. Seneviratne, J. P. Carter, D. W. Airey, and J. R. Booker. A review of models for predicting the thermomechanical behaviour of soft clays. *International Journal for Numerical and Analytical Methods in Geomechanics*, 17(10):715–733, 1993.

[SDC02] N. Sultan, P. Delage, and Y. J. Cui. Temperature effects on the volume change behaviour of Boom clay. *Engineering Geology*, 64(2-3):135–145, 2002.

[SF09] J. Sulem and V. Famin. Thermal decomposition of carbonates in fault zones: Slip-weakening and temperature-limiting effects. *Journal of geophysical research*, 114(B3):B03309, 2009.

[SGR+20] A. Schäfers, A. Gens, A. Rodriguez-Dono, S. Baxter, V. Tsitsopoulos, D. Holton, D. Malmberg, M. Sawada, Q. Yafei, A. Ferrari, L. Laloui, and A. Sjöland. Increasing understanding and confidence in THM simulations of Engineered Barrier Systems. *Environmental Geotechnics*, 7(1):59–71, 2020.

[SP22] H. Song and H. Pei. A Nonlinear Softening Load-Transfer Approach for the Thermomechanical Analysis of Energy Piles. *International Journal of Geomechanics*, 22(5):04022044, 2022.

[SW68] A. Schofield and P. Wroth. *Critical State Soil Mechanics*. McGraw-Hill, London, 1968.

[TC20] V. Tagarelli and F. Cotecchia. The Effects of Slope Initialization on the Numerical Model Predictions of the Slope-Vegetation-Atmosphere Interaction. *Geosciences*, 10(2):85, 2020.

[VBLC10] M. Vandamme, L. Brochard, B. Lecampion, and O. Coussy. Adsorption and strain: The CO2-induced swelling of coal. *Journal of the Mechanics and Physics of Solids*, 58(10):1489–1505, 2010.

[VBPF98] O. Vincké, M. J. Boutéca, J. M. Piau, and D. Fourmaintraux. Study of the effective stress at failure. In *Poromechanics*. CRC Press, 1998.

[VR17] V. Vilarrasa and J. Rutqvist. Thermal effects on geologic carbon storage. *Earth-Science Reviews*, 165:245–256, 2017.

[VVT07] E. Veveakis, I. Vardoulakis, and G. Di Toro. Thermoporomechanics of creeping landslides: The 1963 Vaiont slide, northern Italy. *Journal of Geophysical Research*, 112(F3):F03026, 2007.

[WS50] W. H. Ward and E. C. Sewell. Protection of the Ground from Thermal Effects of Industrial Plant. *Géotechnique*, 2(1):64–81, 1950.

[YTPH14a] N. Yavari, A. M. Tang, J. M. Pereira, and G. Hassen. Experimental study on the mechanical behaviour of a heat exchanger pile using physical modelling. *Acta Geotechnica*, 9(3):385–398, 2014.

[YTPH14b] N. Yavari, A. M. Tang, J. M. Pereira, and G. Hassen. A simple method for numerical modelling of mechanical behaviour of an energy pile. *Géotechnique Letters*, 4:119–124, 2014.

[YTPH16] N. Yavari, A. M. Tang, J. M. Pereira, and G. Hassen. Effect of temperature on the shear strength of soils and the soil–structure interface. *Canadian Geotechnical Journal*, 53(7):1186–1194, 2016.

[YWC+12] W. Ye, M. Wan, B. Chen, Y. Chen, Y. Cui, and J. Wang. Temperature effects on the unsaturated permeability of the densely compacted GMZ01 bentonite under confined conditions. *Engineering Geology*, 126:1–7, 2012.

[ZSAP17] C. Zhu, X. Shen, C. Arson, and A. Pouya. Numerical study of thermo-mechanical effects on the viscous damage behavior of rock salt caverns. In *US Rock Mech. / Geomech. Symp.*, volume 2, pages 1305–1313. OnePetro, American Rock Mechanics Association (ARMA), 2017.

Homogenization and field equations for tightly coupled THMC problems in geomaterials

Manolis Veveakis

Civil and Environmental Engineering, Duke University, Durham NC, USA

In the pursuit of energy resources from increasingly deep reservoirs, it's essential to understand how reservoir rocks behave under high pressure and high temperature (HPHT) conditions. At these depths, rocks can undergo significant changes due to thermal and pressure sensitivity, as well as internal phase changes at the interfaces between pores and solid rock. These changes directly influence how the rocks respond to external forces. To accurately model this behavior, the standard constitutive laws used in geomechanics need to be enhanced. This work summarizes a new multiphysics constitutive theory for sedimentary rocks published recently [SAP$^+$20], based on the principles of viscoplasticity. The new approach homogenizes the internal microstructure and considers that the rock's viscosity is affected by temperature, pore pressure, and the energy required to change the interfaces between rock grains. This energy is determined by the chemical potentials of the different phases involved in processes like the chemical dissolution, precipitation, or mechanical debonding of these interfaces. We hereby summarize the homogenization approach and provide the field equations for THMC problems originally presented in [SAP$^+$20].

1 Introduction

Assessing and enhancing the long-term potential of high-pressure, high-temperature (HPHT) reservoirs is a major challenge in geomechanics. This is crucial not only for unconventional shale gas and deep conventional formations but also for geothermal energy and environmental efforts like nuclear waste disposal and deep energy storage. The difficulty lies in designing engineering operations for vast scales of time and distance, where processes like thermo-mechanical and chemo-mechanical couplings—less significant in shallower environments—play a key role.

To tackle this, we need constitutive modeling that can handle the extreme pressures and temperatures of the Earth's upper crust. The goal is to develop a plasticity theory that predicts the long-term behavior of materials that are often stressed beyond

their initial yield point. This model must incorporate detailed physical mechanisms from the microstructure scale—such as internal transformations—because these tiny changes have a big impact on a material's overall response to stress.

Examples of such models – that accommodate multi-physical feedbacks and are able to operate in the long-term – can be found in the field of metal plasticity, and in particular crystal plasticity, with the first attempts to capture the microscopic response of crystals dating back to the 1930s with the pioneering works of [TQ34a, Eyr36, Oro40, Kau41], to name but a few. These studies, nowadays commonly accepted, showed that the mechanical resistance of metals in shear is dominated by lattice-related processes like the presence of discrete obstacles, lattice resistance, dislocation movements, etc (for more details see [FA82]).

These concepts have been cast into a visco-plastic framework by [Per66], [Lub90], and later generalized to materials displaying pressure sensitivity and more complicated microstructures, like geomaterials [Oka85, Oka81, AO82, Bor91, DNB$^+$14]. Recently [Ein12, ZB17, VRL15a] have extended these concepts to allow the flow law to receive feedbacks from state variables (including pressure,temperature and density). Such concepts have become common knowledge in disciplines studying long-term response of rocks under loading, like Geology, Geophysics and Geodynamics, where the materials are long past their initial yield point and are commonly described as viscous without incorporating the concept of a yield surface or plasticity in general [Kar08]. In these disciplines, the viscosity of the material incorporates all interface processes taking place at the micro-scale, like for example grain boundary sliding, interface chemistry etc. As such, the viscosity of these laws is expressing all microscopic processes as a function of the state variables of the problem at hand, like temperature, pressure and density.

The objective of this work is to provide a modeling framework encompassing internal mechanisms like interface changes (de-bonding, decementation, collapse of capillary bridges, etc) under multi-physical feedbacks, that can be used for modeling Geomaterials at high temperarures and pressures. All the details of this work can be found in recent works of the group [SAP$^+$20, Sar19, LSA$^+$20, LCVP17, LPV20b, LPV20a, GRV19, GRV20, GRVon] that are hereby summarized. To this end, we extend earlier studies considering thermo-chemo-mechanical couplings in Geomaterials [HB90, LC03, LLC08, HFL09, GCH15] and suggest a multi-physics visco-plasticity framework that is enriched with a dependency of the plastic multiplier (viscosity) on state variables and internal interface processes [FB06]. The next sections are laying down the constitutive laws for the mechanical response of rocks experiencing internal interface mechanisms like debonding or interface dissolution/precipitation. The constitutive framework is then completed with governing equations, that are used as evolution laws for the state variables used (pressure and temperature), before being implemented in a finite element simulator and used to reproduce experimental results from triaxial compression tests at different types of rocks. Finally, all the results are synthesized and discussed.

2 Deep Geothermal as an analogy to the moon landing mission for the energy and minerals space

As presented by [RLBC$^+$15], deep geothermal from the hot crystalline basement has remained an unsolved frontier for the geothermal industry for the past 30 years. Unfortunately, although in excess of $0.5 billion have been invested in Australia alone, only limited success can be reported. Therefore, private industry has found it difficult of late to attract matching funds for allocated government grants. Clearly, a new strategy needs to be devised acknowledging the fact that the problem of economical extraction of deep geothermal energy cannot be solved by classical concepts. The requirement for large capital investment provides the first part of the analogy to the equally ambitious 'moon landing' mission. This work mainly addresses the second part of the 'moon landing' counterpart in the energy and minerals space. Unconventional geothermal energy poses a new science challenge that may present unexpected opportunities for deep reservoir engineering and beyond. Strategies have to be devised that acknowledge and are capable to describe the unconventional nature of the material behaviour at high temperature and high depth. We claim that these challenges can only be met by an "unconventional geomechanics" approach.

The concept of drilling into the hot crystalline basement and extracting heat through an artificially engineered reservoir has remained a challenge for geothermal energy since the early experiments at Fenton Hill, USA. The original idea of a hot dry rock (HDR) reservoir was to create fluid flow paths between an injection and extraction well deep into the crystalline hot rock by hydraulic fracturing. It became clear in early projects that rather than creating new hydraulic fractures, the existing natural fractures provided the flow paths, and their transmissibility was improved by stimulation. This has lead to the use of the term Enhanced (or Engineered) Geothermal Systems (EGS). Numerous projects have been carried out in the USA, Europe, Japan and Australia all facing the same problem. The artificially stimulated flow rates could only be sustained at a maximum of around 20–65 L/s, and only with significant parasitic (energy and water) losses incurred through pumping at high operating pressures. A main lesson learned is the necessity to take advantage of the existing geological inventory and the neotectonic deformation field and target existing fracture zones with existing hydrothermal flow.

The original idea, as put forward by one of the protagonists Don Brown [BDK$^+$99], was to create an EGS within a previously impermeable body of a hot crystalline basement rock containing an array of re-sealed (and therefore essentially impermeable) joints. The original idea of a HDR reservoir was therefore to create by hydraulic pressurization a deep, multiply jointed rock mass such, that it is totally con- fined, and enclosed within a "stress cage" as an elastic re- sponse to the hydraulic stimulation of the HDR reservoir. The idea was to select the production temperature, by selecting the drilling depth and the size of the reservoir, by the amount of fluid injected. The first reservoir tests in Fenton Hill in 1980 proved successfully that a production flow rate of 5.9 L/s and a temperature of 158 C can be achieved. The phase II experi- ments

between 1986–1995 improved the production tempera- ture to 190 C and a production flow rate of 13.5 L/s. Injection water loss was also improved from an initial 0.4 to 0.15 L/s for the phase II testing. However, to date we have not seen a commercially viable operation, which could be achieved if the flow rates are at least quintupled, and the water loss and the excessive pumping power problems overcome.

The partial success of the Fenton Hill operation sparked a series of similar attempts over the past 30 years in England (Rosemanowes), Sweden (Fjaellbacka), France (Mayet de Montagne, Soultz), Germany (Urach), Japan (Hijori) and Australia (Habanero). Improvements over the Fenton Hill experiment have only been incremental; yet, important lessons have been learned in the European science project in Soultz where a modified concept to the one followed at Fenton Hill was presented.

The European Soultz-sous-Forêts project set out in 1987 with the same geologic target as the Fenton Hill project (the crystalline basement), however, as an alternative choice a geological system, where active normal faults were expected, was chosen. The granitic basement was not 'dry' but contained geothermal fluids migrating along the fault. Therefore the project was labeled an EGS rather than a HDR project. It reached a target temperature of 200 C and a maximum flow rate of 60 L/s during stimulation. The expected production flow rate for the first geothermal power plant in Soultz sous Forets is 35 L/s at a production temperature of 175 C [GEC$^+$10]. A challenge was the existence of a seriously damaged granitic reservoir in the area of fluid circulation with a style of "fracturing" that was quite unexpected. Soultz features a number of seriously altered zones of granite, which cannot be interpreted by classical fracture mechanics, but rather appear to be strongly affected by fluid alteration zones. From the appearance of these fluid alteration zones the question is raised; what role do chemical alterations play in a deep crystalline granitic reservoir? Rather than using a simple extension of classical linear elastic fracture mechanics to stimulate a fully elastic "stress cage", a new multi-physics approach was found to be needed where thermal, mechanical, fluid, and chemical processes are considered in a fully coupled manner. The science that deals with quantifying these processes is Thermo-Hydro-Chemo-Mechanical (THMC) reservoir modeling.

All the above posit that the challenge of deep geothermnal extraction can be resolved by developing a new THMC geomechanics approach to stimulate such reservoirs. While a number of new unconventional brittle techniques are still available to improve stimulation on short time scales, the astonishing richness of failure modes of longer time scales in hot rocks has so far been overlooked. These failure modes represent a series of microscopic processes: brittle microfracturing prevails at low temperatures and fairly high deviatoric stresses, while upon increasing temperature and decreasing applied stress or longer time scales, the failure modes switch to transgranular and intergranular creep fractures. Accordingly, fluids play an active role and create their own pathways through facilitating shear localization by a process of time-dependent dissolution and precipitation creep, rather than being a passive constituent by simply following brittle fractures that are generated inside a shear zone caused by other localization mechanisms. It is apparent that a new THMC theoretical approach is needed

for the design of new strategies to utilize, enhance and maintain the natural permeability in the deeper and hotter domain of geothermal reservoirs. The new approach is required to be able to offer solutions at extreme conditions and long timescales, and will have the advantage to -rather than engineering an entirely new EGS reservoir- acknowledge a suite of creep-assisted geological processes that are driven by the current tectonic stress field. Such processes are particularly supported by higher temperatures potentially allowing in the future to target commercially viable combinations of temperatures and flow rates.

3 Mathematical Framework of Multi-Physics Mechanics

We start by presenting the governing laws of physics used in this framework. The work is based on the basic and fundamental principles of continuum mechanics, considering a representative elementary volume (REV), the smallest volume over which a measurement can be made that will yield a value representative of the whole [Hil63]. Given all applications in this work involve rocks of a few centimetres at the smallest, this assumption is not restrictive for the type of rocks considered (mudstone, sandstone, carbonates).

3.1 Extended Mixture's Theory

Porous media represent a wide range of materials but also a tremendous challenge to be fully understood and harnessed. Most materials exhibit heterogeneous structures when observed close enough; yet, porous media bear an additional level of complexity since their characteristic source of heterogeneity, the pores, also allows fluid flow. Among porous media, geomaterials, stemming from millions of years of transformations under harsh conditions, represent a particularly complex subclass, inasmuch as processes in these media are multiphysics and multiscales. Recent advances in geosciences found, however, that this complexity boils down to the great heterogeneity and stochasticity of geomaterials' microstructures. The dependence of the macroscopic behavior of geomaterials on the latter is the recipe for a wide range of processes. For instance, pressure solution [NEM09, CRG13, vdENS19, GRV20], strain localization [VS95, KAVA18], frictional instabilities [RSS18a, RSS$^+$18b], fault reactivation [VPA14, LPV20b], and granular flow [BE21] largely depend on the microstructural geometry, or *morphometry*. The same conclusion holds for engineered porous materials, such as ceramics [SPS18] and energetic materials [CRN$^+$20]. Biomaterials, forming a third subclass of porous media [HLK$^+$02], are also increasingly studied in the light of their microstructures, especially in bone mechanics [AS06, WKM$^+$02].

Therefore, adequately modeling the microstructural dynamics of porous media is a crucial step toward better understanding their macroscopic behavior, but also laying out the blueprint for novel metamaterials. In metallurgy, this has been achieved with phase-field modeling [AC79, PE10, BSO19], which tracks the grains interface through

finite elements, and in geosciences, with discrete element modeling (DEM) [O'S11, KAVA18], which tracks the grains as discrete elements. Recently, the author and colleagues introduced a phase-field model for geomaterials to propose capabilities complementary to those of DEM [GRV20, GRVon] (see Chapter 3). That said, due to computational limitations, relying solely on microscopic simulations for large scales and, more generally, for industrial applications, is unrealistic. On the other hand, the existing constitutive macroscopic laws rely heavily on destructive experimental calibration, which can be unfeasible because of the limited availability of materials, or the impossibility to reproduce environmental conditions. For example, obtaining rocks from high depths can be prohibitively expensive or even impossible, and geological time scales are hardly reproducible in laboratory. As for biomaterials, such as bones, they are best studied in vivo (see [FRG$^+$19] e.g.). These hurdles point toward finding a compromise between systematically modeling the microstructure of porous media and relying on destructive experiments, in order to predict the macroscopic behavior of these materials.

The continuum studied includes considerations for a two-phase material, made of a fully saturated porous matrix filled with fluid. As such, the material is decomposed into the part that constitutes the skeleton, receiving forces from the loading conditions, and the weak (or fluid) phase which occupies the void volume and does not participate into the force chain network. The volume ratio of the voids can therefore be defined as the porosity,

$$\phi = \frac{V_{void}}{V}, \tag{1}$$

which allows the deployment in the following sections of the well known governing equations for a bi-phasic material in the context of mixtures theory. Based on that, we then define the respective phase densities:

$$\rho_1 = (1 - \phi)\rho_s \tag{2a}$$

$$\rho_2 = \phi\, \rho_f \tag{2b}$$

where the subscripts s and f refer to the solid and fluid components respectively.

The aforementioned canonical definitions are illustrating the traditional approach of homogenizing complex media via the use of a single internal state variable, in this case the porosity. Similar approaches can be found in damage and damage-like homogenization, like breakage where the internal state variable is identified to be a measure of the grain size [Ein07]. The complete depiction of a porous medium is, however, much more complicated and cannot be expressed through a single internal state variable. A mathematically complete representation of complex internal geometries is provided recently by [GRVon, LPD$^+$25] in a framework supported by Hadwiger's theorem [AMR$^+$19].

In that representation, the total internal volume (what we call traditionally porosity) ϕ is expanded to be described by four morphometers: the nominal volume of voids M_1, the internal surface area of the solid-fluid interface M_2, the mean curvature or average grain size M_3 and the Euler characteristic M_4. Mathematically, these four are

expressed as moments of the original definition of the lagrangian (reference) porosity n, with $M_1 \sim n$, $M_2 \sim \epsilon\nabla n$, $M_3 \sim \epsilon^2\nabla^2 n$, $M_4 \sim \epsilon^3\nabla^3 n$. This provides a taylor expansion of the total porosity ϕ around its reference value to incorporate higher order effects representing the internal geometrical complexity:

$$\phi = M_1 + \epsilon M_2 + \epsilon^2 M_3 + \epsilon^3 M_4 = M_1 \left(1 + \epsilon\frac{M_2}{M_1} + \epsilon^2\frac{M_3}{M_1} + \epsilon^3\frac{M_4}{M_1}\right) \quad (3)$$

When the porous geometry is sufficiently simple, for example when stacks of spheres are assumed, the higher order terms are negligible and we recover the classical view of poromechanics. However, when irregular shapes with strong gradients are considered, the higher order terms could become important and extend the traditional mixture's theory with additional compressibility-like terms.

3.2 Governing Laws

Mass Balance The mass balance of the fluid and solid phases can be expressed as:

$$\begin{aligned} \frac{\partial\rho_1}{\partial t} + \frac{\partial(\rho_1 V_k^{(1)})}{\partial x_k} &= 0 \\ \frac{\partial\rho_2}{\partial t} + \frac{\partial(\rho_2 V_k^{(2)})}{\partial x_k} &= 0 \end{aligned} \quad (4)$$

In this work we will focus in the case where the material is fully saturated with one fluid. In this case, each phase can assumed to follow the equation of the state with respect to the (state) pressure of the fluid p_f and Temperature T:

$$\frac{d\rho_{(i)}}{\rho_{(i)}} = \beta_{(i)}dp_f - \lambda_{(i)}dT, \quad i \in \{s, f\} \quad (5)$$

where $\beta_{(i)}$ is the compressibility ($\beta_{(i)} = \frac{1}{\rho_{(i)}}\left(\frac{d\rho_{(i)}}{dp_f}\right)_T$) and $\lambda_{(i)}$ is the thermal expansion ($\lambda_{(i)} = -\frac{1}{\rho_{(i)}}\left(\frac{d\rho_{(i)}}{dT}\right)_{p_f}$).

Using Eq. 4 and Eq. 5, combined with Darcy's law for the filter velocity $\phi(V_k^{(2)} - V_k^{(1)}) = -\frac{k}{\mu_f}\frac{\partial p_f}{\partial x_k}$ (k is the permeability an μ_f the saturating fluid viscosity) while neglecting convective terms, leads to the final mass balance equation for the mixture:

$$\beta_m\frac{\partial p_f}{\partial t} - \lambda_m\frac{\partial T}{\partial t} - \frac{k}{\mu_f}\frac{\partial^2 p_f}{\partial x_k x_k} + \frac{\partial V_k^{(1)}}{\partial x_k} = 0 \quad (6)$$

where $\beta_m = (1-\phi)\beta_s + \phi\beta_f$ is the mixture's compressibility, and $\lambda_m = (1-\phi)\lambda_s + \phi\lambda_f$ the mixture's thermal expansion coefficient.

Momentum Balance The acceleration of the mixture is assumed to be negligible. Therefore, the local form of the momentum balance of the mixture together with the effective stress definition $\sigma_{ij} = \sigma'_{ij} - bp_f\delta_{ij}$ (where σ_{ij} is the total stress tensor of the mixture, σ'_{ij} the effective stress tensor, b the Biot coefficient and p_f the pore pressure), can be written in its stress equilibrium regime as follows,

$$\frac{\partial \sigma'_{ij}}{\partial x_j} - \frac{\partial \Delta p_f \delta_{ij}}{\partial x_j} + b_i = 0 \tag{7}$$

where we have assumed $b = 1$ for simplicity in the calibration process of the model. By convention, stresses are taken negative in compression in this work. In this expression we decomposed the pore pressure itself as $p_f = p_{hyd} + \Delta p_f$ where p_{hyd} is the hydrostatic pressure (constant in this study) and Δp_f is the excess pore pressure.

Energy Balance The local form of the energy equation expresses the energy balance and takes into account Fourier's law for heat conduction and the second law of thermodynamics [RRRH00]:

$$(\rho C)_m \frac{\partial T}{\partial t} = \alpha \frac{\partial^2 T}{\partial x_i \partial x_i} + \Phi \tag{8}$$

where $(\rho C)_m$ the heat capacity of the mixture and α the thermal conductivity. The term Φ corresponds to the mechanical work rate dissipated into heat, which is non negative based on the second law of thermodynamics:

$$\Phi = \sigma'_{ij}\dot{\epsilon}^i_{ij} + \frac{\partial \psi}{\partial \xi_k}\dot{\xi}_k \geq 0 \tag{9}$$

In this expression, the (frequently called cold-) work of internal state variables is expressed through the product of derivative of the Helmholtz free energy ψ with respect to any dissipative internal state variable vector ξ_k and its rate, $\frac{\partial \psi}{\partial \xi}\dot{\xi}_k$. The expression (9) can be re-arranged to take the form:

$$\Phi = \chi \sigma'_{ij}\dot{\epsilon}^i_{ij} \geq 0\ ,\ \chi = 1 - \frac{E_\xi \dot{\xi}_k}{\sigma'_{ij}\dot{\epsilon}^i_{ij}} \tag{10}$$

where $E_\xi = -\frac{\partial \psi}{\partial \xi_k}$ and χ is the Taylor-Quinney coefficient [TQ34b], expressing the amount of mechanical work dissipated by the internal state variables into internal microstructural mechanisms. When it is zero all the mechanical work rate is consumed into internal state variables, whereas when it is equal to one all the mechanical work rate is converted into heat. Note that χ is in general a function of all the state variables, like density (or pressure), temperature, ξ_k, etc, and that when it is zero, it corresponds to a constant mechanical dissipation state. In this work we are considering equal to one, and relegate the effect of the state variables into the flow law, to account for the effect of surface energy terms that would normally appear as higher order (gradient) terms in the volumetric expression of the energy balance equation.

4 THMC Elasto-Visco-Plasticity with internal mechanisms

In this section we present the temperature- and pressure- sensitive law of elasto-viscoplasticity that will be used in this work. The underlying physical model for this study is combining concepts from the viscoplastic approach in metals, as discussed in the introduction, with the required modifications to capture interface mechanisms in pressure-sensitive, porous materials.

The formulation is based on the principles of overstress plasticity [Per66], used in a novel elasto-viscoplastic approach [PV16]. As is done classically in Mechanics, the total strain rate is decomposed into its elastic (reversible) and plastic (irreversible) components, $\dot{\epsilon}_{ij} = \dot{\epsilon}^r_{ij} + \dot{\epsilon}^i_{ij}$.

Thermo-Poro-Elasticity The reversible part is considered to obey a linear thermo-elastic law of the form:

$$\dot{\epsilon}^r_{ij} = C_{ijkl}\dot{\sigma}'_{kl} - \lambda_s \Delta T \delta_{ij} \tag{11}$$

where σ'_{ij} is the effective stress, obeying Terzaghi's law [Ter25] $\sigma_{ij} = \sigma'_{ij} - p_f\delta_{ij}$ (where σ_{ij} is the total stress tensor of the mixture and p_f the pore pressure), C_{ijkl} is the compliance modulus, λ_s the thermal expansion coefficient of the solid and ΔT the temperature variation. Note that the Einstein notation (summation of repeated indices) applies and that δ_{ij} is Kronecker's delta.

Visco-plasticity The irreversible part of the strain rate respects a visco-plastic flow law which is expressed in terms of the norm of the overstress of the deviatoric and volumetric components, as follows (see also figure 1):

$$\dot{\epsilon}^i_d = \frac{\dot{\epsilon}^d_0}{\dot{\epsilon}_0}\,\dot{\Pi}\,\frac{\partial f}{\partial q}, \tag{12a}$$

$$\dot{\epsilon}^i_v = \frac{\dot{\epsilon}^v_0}{\dot{\epsilon}_0}\,\dot{\Pi}\,\frac{\partial f}{\partial p'}, \tag{12b}$$

where Π is the overstress function, hereby assumed to be the norm of the flow rate tensor at a reference strain rate $\dot{\epsilon}_0$ (see figure 1): $\dot{\Pi} = \sqrt{\dot{\epsilon}_0^2 \left\langle \frac{q-q_Y}{\sigma_{ref}} \right\rangle^{2m} + \dot{\epsilon}_0^2 \left\langle \frac{p'-p_Y}{\sigma_{ref}} \right\rangle^{2m}}$, f is the initial yield envelope of the material (considered here to be constant and independent of temperature, thus relegating all the post yield evolution in the "viscosity" of the material), $\dot{\epsilon}_0^{v,d}$ is the reference strain rate for the deviatoric and volumetric part, p' denotes the volumetric mean effective stress, q the equivalent deviatoric stress (also called von Mises stress), p_Y and q_Y the corresponding values of p' and q at yield, and σ_{ref} a reference stress. The angular brackets $\langle\cdot\rangle$ represent the Macaulay brackets.

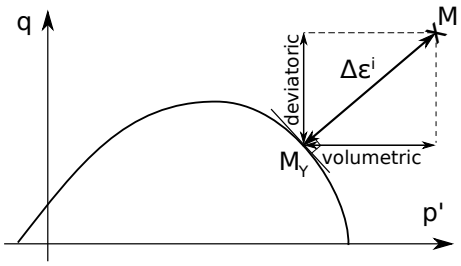

Figure 1: Decomposition of the plastic flow rule into a volumetric and a deviatoric components in the $p' - q$ space (mean effective stress – shear stress), for a stress point M and its corresponding point on the yield point M_Y.

Following the need to allow in principle different mechanisms to operate in volumetric and deviatoric loading, the reference strain rates are assumed to take Arrhenius-like forms like:

$$\dot{\epsilon}_0^d = \dot{\epsilon}_0 \exp\left(-\frac{\Delta Q^d_{mech}}{RT}\right), \tag{13a}$$

$$\dot{\epsilon}_0^v = \dot{\epsilon}_0 \exp\left(-\frac{\Delta Q^v_{mech}}{RT}\right) \tag{13b}$$

where R the universal gas constant and T the temperature. ΔQ^d_{mech} and ΔQ^v_{mech} are the activation enthalpies of the deviatoric and volumetric components, expressing the activation energy required to overcome (activate) the dissipative mechanisms admissible by the microstructure. It is also to be noted that traditional concepts like dilatancy are hereby expressed through these activation enthalpies. Indeed, the dilatancy coefficient would be $\psi = \frac{\dot{\epsilon}^i_v}{\dot{\epsilon}^i_d} = \exp\left(\frac{\Delta Q^d_{mech} - \Delta Q^v_{mech}}{RT}\right)\frac{\partial q}{\partial p'}$, with the model deviating from associativity when $\Delta Q^d_{mech} \neq \Delta Q^v_{mech}$.

The enthalpies ΔQ^d_{mech} and ΔQ^v_{mech} are functions of all the state variables of the problem (density, pressure, temperature, etc). Therefore, temperature, pressure and density dependencies are accounted for through the definition of the activation enthalpies for the deviatoric (ΔQ^d_{mech}) and the volumetric (ΔQ^v_{mech}) components of the irreversible strain rate. Those terms incorporate the activation energies of all micromechanical mechanisms taking place, including frictional initiation [RLR01], volumetric pore collapse [PV16], or debonding and grain cracking [ZB17], and can be functions of all the global and internal state variables of the problem at hand. An example of such an approach is illustrated in the following section for arbitrary processes at the skeleton's interface, emphasizing the specific mechanism of debonding in an isotropic medium where $\Delta Q^d_{mech} = \Delta Q^v_{mech} = \Delta Q_{mech}$. Through considerations of the interface physics at the grain scale, we are able to upscale for a continuum

expression of ΔQ_{mech} in the considered representative elementary volume (REV, see 3).

Let us now consider a generic system of two grains submerged in a saturating fluid, and assume them being connected through a bonding interface which can be of solid (cement) or fluid (capillary bridge) form [GCH15]. This system of grains and bond (skeleton) is experiencing a mean pressure P_{sk}, while the saturating fluid is experiencing a mean pressure p_f. In such a system, debonding/bonding processes may take place at the interface, with them being of chemical (dissolution/precipitation) or mechanical (breakage/healing) origin, or even a combination thereof (e.g. breakage/precipitation or dissolution/healing). A generic way of approaching this interface configuration, is to assume that the interface is allowed to experience a transition of the solid skeleton into a fluid (and vice versa), following a phase transformation of the form $skeleton \rightleftharpoons fluid$. Since all these processes – irrespectively of their origin – are affecting the mechanical response of the skeleton, the activation enthalpy of the mechanical law needs to account for these interface effects. In a two-grain (single contact) system, this is expressed in incremental form as:

$$\Delta q_{mech} = \Delta q^0_{mech} + \Delta q_{interface} = \Delta q^0_{mech} + \sum_i \mu_i \Delta m_i \tag{14}$$

In this equation Δq^0_{mech} is the base enthalpy of the system and $\Delta q_{interface} = \sum_i \mu_i \Delta m_i$ for $i = sk, f$ is the enthalpy of the interface, expressing the energy required to break chemo-mechanical bonds of the skeleton and form weak fluidized phases. μ_i is the chemical potential and m_i the mass of each constituent.

The mechanical enthalpy of a system of multiple contacts is obtained if we average Eq. (14) over the volume of our Representative Elementary Volume (REV) V for a given contact distribution $N(V)$:

$$\Delta Q_{mech} = \frac{1}{V} \int \Delta q_{mech} N(V) dV \tag{15}$$

Note that the size of the volume is arbitrary and can be calculated separately by using thermodynamic convergence of the upper and lower bound of the dissipation rate of an assembly, as described by [VRL15b]. Such an analysis is out of the scope of this work, as we assume the presence of an REV at a sufficient number of grain contacts. Under this assumption, and for the simple case of a uniform contact distribution Eq. (15) provides:

$$\Delta Q_{mech} = \Delta Q^0_{mech} + \mu_1 \Delta \rho_1 + \mu_2 \Delta \rho_2 \tag{16}$$

where $\Delta Q^0_{mech} = \Delta q_{mech} n_c$, with n_c being the number of evenly distributed contacts in the REV. The indices $1, 2$ are referring to the solid and fluid phases, respectively ($\mu_1 = \mu_{sk} n_c$, $\mu_2 = \mu_f n_c$). Note that all the contacts are assumed energetically equiprobable, allowing for the chemical potentials to be considered constant over the volume averaging procedure. Substituting in Eq. (16) the mixture's expressions for

the densities $\rho_1 = (1-\phi)\rho_{sk}$ and $\rho_2 = \phi\rho_f$, with ϕ being the porosity of the mixture, we obtain:

$$\Delta Q_{mech} = \Delta Q^0_{mech} + (\mu_f n_c \rho_f - \mu_{sk} n_c \rho_{sk})\, \Delta\phi \tag{17}$$

Note that when the two phases of the interface are in equilibrium, the chemical potentials are equal, $\mu_f = \mu_{sk}$.

Recalling the mass balance of the solid phase (neglecting convective terms) in its incremental form, $(1-\phi)d\rho_s = \rho_s d\phi$, and the Equation of State (EoS) considered (Eq. 5), we may express $\Delta\phi$ in terms of the excess pore fluid pressure Δp_f and temperature variation ΔT, $\Delta\phi = \phi_0\beta_\phi \Delta p_f - \phi_0\lambda_\phi \Delta T$, where $\beta_\phi = (1-\phi)\beta_s, \lambda_\phi = (1-\phi)\lambda_s$ are the compressibility and thermal expansion coefficients of the void space [Ric06]. In addition, the chemical potentials of the $i-$species are frequently expressed through their partial pressures experienced, through a pressure-like quantity f [Kar08]:

$$\mu_i = \mu_0 + RT \ln \frac{f_i}{f_0} \tag{18}$$

where μ_0 is a reference value of the chemical potential at a reference value f_0, that will be set to zero hereafter to ensure tractability of the mathematical derivations. The pressure-like quantity f is identified as the fugacity in the case of gaseous constitutents. It has the units of pressure and is an "effective pressure" i.e, the pressure that gives the correct value for the chemical potential of a real gas. In case of ideal gases, the fugacity is therefore equal to the gas pressure P. In the more general case of condensed (liquid or solid) phase, the deviation of the fugacity from the ideal case is expressed through a fugacity coefficient ν linking it to a representative pressure of the system for each constituent i, $f_i = \nu_i P$ [Kar08]. In this case the reference value is set to $f_0 = P$.

Substituting the above considerations into Eq. (17) we finally obtain:

$$\Delta Q_{mech} = \Delta Q^0_{mech} + \frac{n_c RT}{\rho_0} (\rho_f \ln \nu_f - \rho_{sk} \ln \nu_{sk})\, \Delta\phi \tag{19a}$$

$$\Delta\phi = \phi_0\beta_\phi \left(\Delta p_f - \frac{\lambda_\phi}{\beta_\phi} \Delta T \right) \tag{19b}$$

Since the fugacity coefficients are in principle unknown for non-ideal gas components, in this study they will be first used as inversion parameters, and later discussed for their physical origin and applicability to the mechanics of sedimentary rocks. We will therefore be using the following expression,

$$\Delta Q_{mech} = \Delta Q^0_{mech} + \Delta\phi V_{act} \tag{20}$$

where $V_{act} = \frac{n_c RT}{\rho_0} (\rho_f \ln \nu_f - \rho_{sk} \ln \nu_{sk})$.

5 Model Validation

In this section we calibrate the visco-plastic constitutive law for different pore pressures and temperatures and restrict further the mathematical formula of the chosen Arrhenius law of Eqs. (13), which encapsulates the pressure and temperature sensitivity of the model. For this task, the experimental data from [FP89] have been chosen, comprising a series of triaxial tests in Carrara marble, Solnhofen limestone and Gosford sandstone. These tests were performed under constant confinement (300 MPa), and the pore pressure was used to vary the mean effective stress instead of directly controlling the confining pressure as in typical triaxial experiments. Five different values of the pore pressure were applied, ranging from 30 to 280 MPa. Furthermore, the experiments were conducted with argon as saturating fluid, which remained at supercritical state during the tests at four different values of temperature ($20^\circ - 600^\circ$C), and two loading rates ($10^{-4}s^{-1}$ and $10^{-5}s^{-1}$). An example of the results reported can be found in figure 9a of [FP89].

Given the number of possible combinations of these tests, Fischer and Paterson focused on reporting mainly the axial stress of the material at 10% axial strain as representative deformation at post yield state of the material (as can be seen figure 9b in [FP89]). At this strain the materials are already in the post-yield regime, having accumulated significant plastic deformation. Since our target in this section is to calibrate the visco-plastic formulation against these data, the following simplifying assumptions have been made based on the experimental results: 1) the material is treated as rigid-viscoplastic, 2) the material admits a Drucker-Prager yield surface, $f = q - c - \tan\alpha p'$ (c is the cohesion and α the friction angle in the $p' - q$ space). This choice allows to properly describe the pressure sensitivity of the material as suggested by the experimental data (see figure 9a,b in [FP89]), while keeping the yield surface linear.

Starting with the sandstone data (figure 2a,b) it is observed that the material remains pressure sensitive throughout the experiments and the results are fairly regular. As such, it seems reasonable to assume that the composition of the material remains the same despite the significant increase in the temperature. For this series of data, the inversion was made with respect to the activation volume, while searching for the optimal values of the friction angle the strain rate ratio and the activation energy. The values used to fit the data at $10^{-4}s^{-1}$ and $10^{-5}s^{-1}$ strain rate are summarized in [SAP+20]. The corresponding results of the calibration are shown in figure (2a,b). Note that the nature of the activation volume is unknown in the thermo-mechanical context at the laboratory scale so far, and as such it is used as a free parameter inverted from the fitting exercise. Significant variation in V_{act} could be explained as the result of the debonding of grains for instance. Note that the change of the parameter A from 0.5 to 0.2 at $10^{-4}s^{-1}$ and $10^{-5}s^{-1}$ strain rate, respectively represents the viscous effect triggered from the change in the loading rate.

By looking at the reported data of limestone and marble (Fig. 3a,b and 4), it can be observed that the pressure sensitivity changes significantly with increasing temperature.

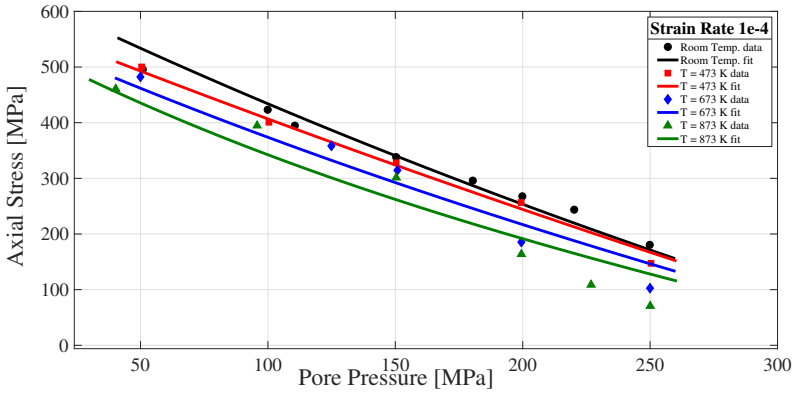

(a)

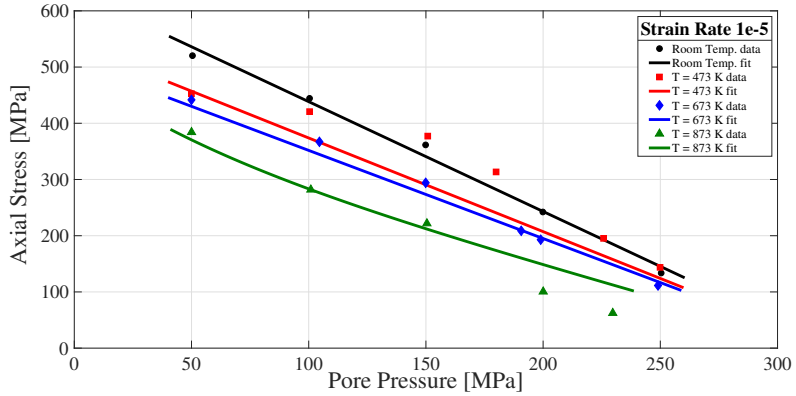

(b)

Figure 2: (a) Fitting sandstone data at $10^{-4}s^{-1}$ strain rate, (b) Fitting sandstone data at $10^{-5}s^{-1}$ strain rate

The materials become more pressure insensitive (i.e. undrained), indicative of excess pore pressure generation inside the sample. A possible candidate for a mechanism causing excess pore pressure under high temperatures in carbonate-rich rocks is the presence of a fluid-release chemical alteration, potentially producing excess pore fluid pressure during chemical decomposition. This chemical change has been reported by [FP89], who stated that the limestone material was uncontrollable at high temperature and higher strain rate. The chemical alteration leads to the change of the yield surface, decreasing the friction angle α and the viscosity as expressed by the ratio of strain rates A. Therefore, in the optimization process those two parameters were allowed to vary for each temperature to capture the behaviour for limestone and marble, while V_{act} and $\Delta Q^0_{mech}/m$ were kept constant. Setting the value of V_{act} at very low values renders the hydraulic effects inactive, which seems reasonable since the experiments are drained and the pressure sensitivity is negligible at high temperatures.

In summary, all calibrations in this section show that the model can capture adequately the rate, temperature, and pressure dependency of different materials. They can be included just by changing the yield surface as in classical thermo-plasticity. The assumptions used here are crude as in the lab scale, thermo-elastic effects are important. The fact that the model does a good job despite that should be noted here. Indeed, the fact that the same model, with reasonable and comparable parameter values, can capture adequately the behaviour of a variety of materials at different temperature and pressure conditions, suggests that this model is sufficiently rich to be used across materials and loading conditions.

Despite being able to capture the pressure and temperature sensitivity of these materials, the tests were performed at relatively low effective confinement, not allowing the materials to reach the cap of the yield envelope that is present at high confinements. In addition, this data set does not allow to evaluate the validity of the evolution laws of the model, as usual when capturing stress-strain evolution in triaxial experiments. To test these capabilities of the model, we present in the next section the performance of the model against triaxial experiments of sandstone and mudstone across a wide range of pressures, reaching the cap.

6 Modeling Triaxial Compression Tests with the Field Equations

In this section, the theoretical framework described previously is used to fit a series of laboratory tests for different types of rocks (sandstone and mudstone) subject to drained triaxial compression. This is achieved by solving -using finite element approaches [GNHLG09, BFS$^+$15]- the governing laws of momentum, mass and energy balance (see 3), combined with the elasto-viscoplastic model presented in the previous sections. The numerical approach used to solve the theoretical framework is using REDBACK, an open-source parallel simulator for Rock mEchanics with Dissipative feedBACKs [PV16, PPV16]. Note that, since the model's hardening law is expressed through the state variables temperature and porosity (pore pressure), the mass and en-

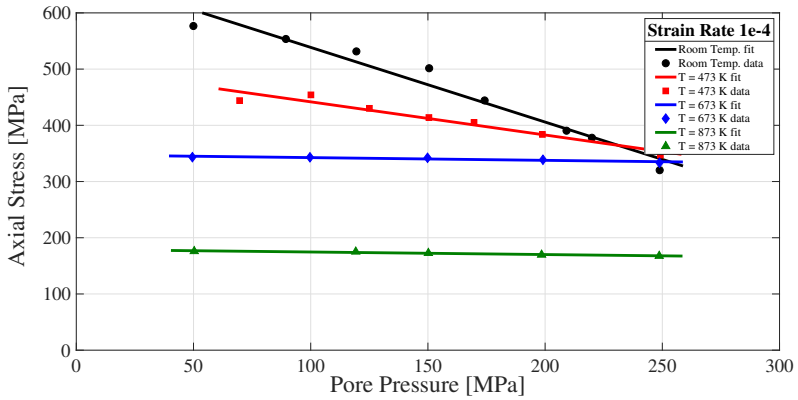

(a)

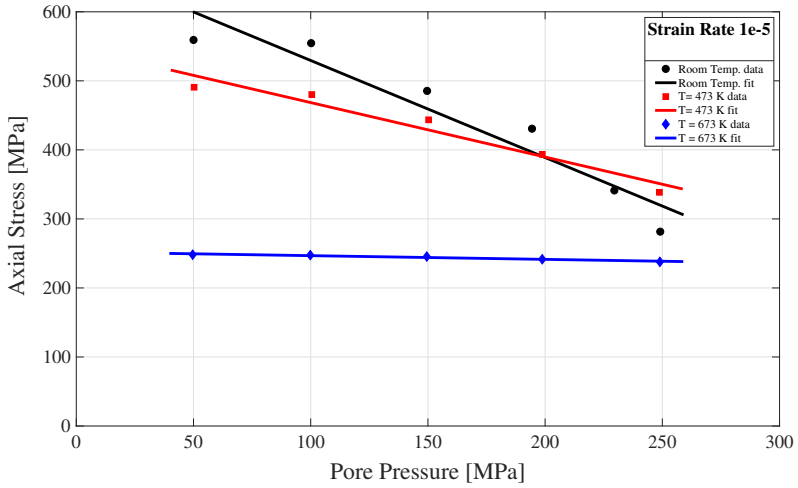

(b)

Figure 3: (a) Fitting limestone data at $10^{-4}s^{-1}$ strain rate, (b) Fitting limestone data at $10^{-5}s^{-1}$ strain rate

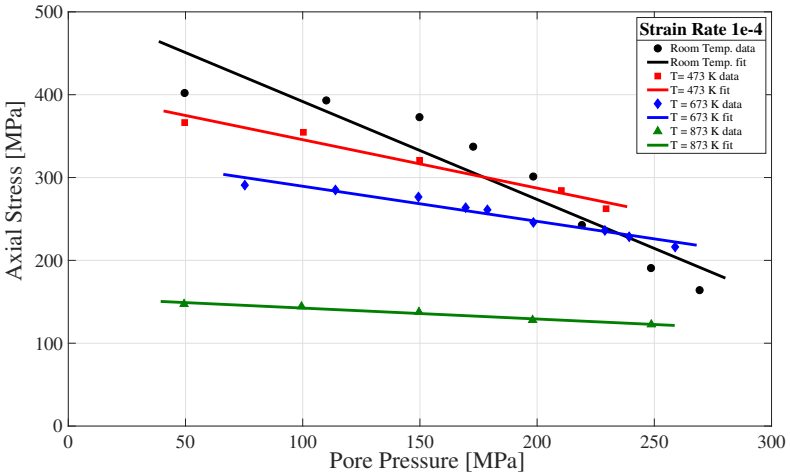

Figure 4: Fitting marble data at $10^{-4}s^{-1}$ strain rate

ergy balance represent the equivalent evolution laws of the assumed state variable in classical plasticity, with the added benefit of the present framework including internal length scales that can regularize otherwise mesh-sensitive solutions like the localization of plastic deformation during softening branches of the stress-strain response (see 7).

Having seen the model's response against materials having a linear (Drucker-Prager) yield surface, the goal of this section is to constrain the form of the activation enthalpy ΔQ_{mech} of the flow law, for materials that exhibit a non-linear, capped yield envelope. Recalling the discussion of the introduction, ΔQ_{mech} is expected to have a generic form of the following type for wet experiments:

$$\Delta Q_{mech} = \Delta Q^0_{mech} + \Delta\phi V_{act} \tag{21}$$

where ΔQ^0_{mech} is a reference value of the activation enthalpy, $\Delta\phi$ is the porosity variation described by Eq. 19ab, and V_{act} the activation volume for the pore volume deformation processes. In the following, we are using the numerical inversion procedure described in [Lin19, LSA+20] to constrain the values of ΔQ^0_{mech} and -mainly- of V_{act}.

6.1 Triaxial Compression Test for Sandstone

The first case considered in this section was presented by [WDZ97], who conducted a series of triaxial experiments on Adamswiller sandstone under a broad range of effective pressures. Through these tests the authors were able to identify the transition in failure mode from brittle faulting to cataclastic flow. Six cylindrical samples were

used, cored parallel to the bedding, 38.1 mm long and 18.4 mm in diameter, with 22.6% initial porosity. The experiments were performed at a fixed loading rate of 5×10^{-5}/s, under confining pressures of 5, 20, 40, 60, 100 and 150 MPa respectively.

Figure (5a) shows the stress paths from the laboratory experiments [WDZ97] with the corresponding yield points identified by the original authors. See [WDZ97] for all details regarding the experiments. These experiments were fit with a cap envelope consisting of a Drucker Prager [DP52] surface in shear and a Modified Cam Clay model as a cap [RB68], expressed as $\left(\frac{q}{M}\right)^2 + p(p - p_0) = 0$. The preconsolidation stress p_0 and the slope of the critical state line M were inverted from the experimental data and set to be $p_0 = 210$ MPa and $M = 1.35$.

Those experiments were then modelled numerically following the methodology described by [PV16]. The experimental curves reported for this sandstone have been fitted by using the material properties provided by the authors of the experimental works, listed in table (1), and by varying only V_{act} at different confining pressures. The optimal fit for both the deviatoric and volumetric component is shown in figures (6a,b). For the inversion process, we optimized the numerical results to fit the deviatoric component of Fig. (6a), and obtained the volumetric component of Fig. (6b) as a forward prediction of the model. The fitting procedure was performed for a constant value of ΔQ^0_{mech} and by varying V_{act} with confinement (i.e. constant during each test but allowed to change with confinement). During this procedure, we derived the following logarithmic dependence of V_{act} on confining pressure:

$$V_{act} = \alpha_0 \left(1 - \frac{\ln P_{c(max)}/p_0}{\ln P_{cs}/p_0}\right) RT = \alpha_0 \frac{RT}{\ln P_{cs}/p_0} \ln \frac{P_{cs}}{P_{c(max)}} \tag{22}$$

In this expression P_{cs} is the effective confining pressure corresponding to the critical state for a given stress path [PV16]. In [SAP+20] we retrieved that for the yield envelope used during the inversion (figure 5a), $\alpha_0 = 29.4$. It is to be noted that V_{act} changes sign with confinement, being negative when $P_{cs} < P_{c(max)}$ (i.e. at the "dilatant" shear part of the yield envelope where "brittle" failure is observed in rocks), positive when $P_{cs} > P_{c(max)}$ (i.e. at the "contractant" cap of the yield envelope where "ductile" response is encountered), and zero at critical state $P_{cs} = P_{c(max)}$.

6.2 Triaxial Compression Test for Mudstone

The second series of experiments used to validate the model in triaxial compression was performed by [OKH+11] on diatomaceous mudstone. The test was aiming to demonstrate the existence of compaction bands in this rock and how the variation of the confinement pressure affect on the direction and the inclinations of the strain localization. A series of triaxial tests was performed on six rectangular shaped-prismatic specimens with 8 cm high and 4 cm side. In order to avoid the effect of the initial anisotropy the specimens were taken with their longitudinal direction perpendicular to the plane of sedimentation. Various levels of confining pressure to observe differ-

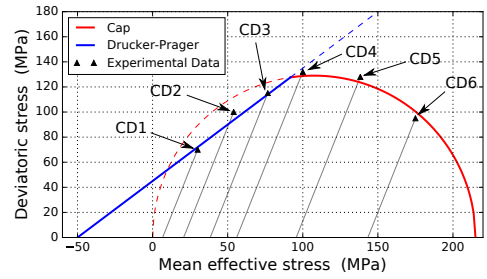

(a)

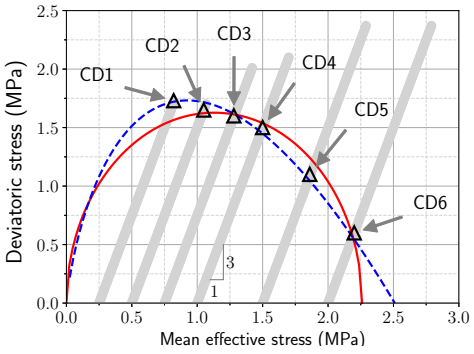

(b)

Figure 5: (a) The experimentally derived yield points (circles) for experiments performed at 6 different confinements (CD 1-6) by [WDZ97] and the modified cam-clay yield envelope used in modelling the tests (solid line), (b) is a modified figure from [PV16] showing the best fits of the data using the original Cam Clay (dashed line) and Modified Cam Clay (solid line) models. The experimental stress paths and corresponding yield points were taken from figure 5 in [OKH$^+$11]

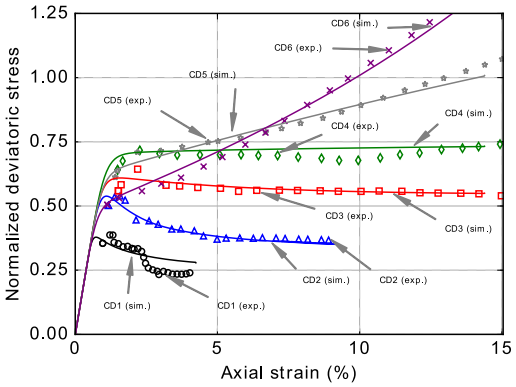

(a)

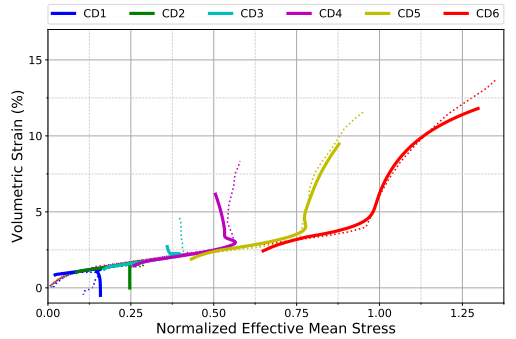

(b)

Figure 6: (a) The normalized (against the preconsolidation pressure) deviatoric stress (τ) vs. axial strain results for the experiments (symbols) and the numerical simulations (lines) for sandstone, (b) The volumetric strain versus the effective mean stress results for the experiments (dashed lines) and the numerical simulations (solid lines) for sandstone.

Parameter	Mudstone	Sandstone
$c_{th}\,[\mathrm{m}^2/\mathrm{s}]$	1.3×10^{-6}	1.43×10^{-7}
$k_\pi\,[\mathrm{m}^2]$	1.48×10^{-14}	1.55×10^{-9}
$\mu_f\,[Pa.s]$	8.9×10^{-4}	8.9×10^{-4}
$\beta_m\,[Pa^{-1}]$	2.5×10^{-10}	9.34×10^{-8}
$\dot{\epsilon}_0\,[s^{-1}]$	1.3×10^{-2}	1.36×10^{-3}
$\Delta Q^0_{mech}\,[J/mol]$	1000	1345
$\lambda_m\,[K^{-1}]$	3.88×10^{-5}	5.18×10^{-5}
$\sigma'_{ref}\,[MPa]$	189	2.26
$T_{ref}\,[K]$	300	300
$x_{ref}\,[m]$	0.01	0.02
$m\,[-]$	2	2
$\chi\,[-]$	0.65	0.65

Table 1: Parameters used in order to fit the experimental data for sandstone and mudstone. The expression $c_{hy} = k_\pi/\mu_f\beta_m$ have been used for the hydraulic diffusivity where k_π the permeability and μ_f the fluid viscosity. Note that $\frac{\lambda_\phi}{\beta_\phi}$ has been taken equal to $10^{-2}\ MPa/^\circ C$, having negligible influence due to the isothermal nature of the tests.

Table 2: The selected confinement pressures used in the triaxial test experiment from [OKH$^+$11]

Case No.	CD1	CD3	CD3	CD4	CD5	CD6
Effective confining pressure (MPa)	0.25	0.5	0.75	1.0	1.5	2.0

ent deformation patterns and the scenarios are listed in table (2). All the tests were conducted up to roughly 20% axial strain.

Following the same methodology described in Section 6.1 for sandstone, a series of numerical experiments are performed using a Modified Cam Clay yield envelope. To match the experimental data, the values of $p_0 = 2.26$ MPa and $M = 1.44$ were selected (see figure (5b). The activation enthalpy ΔQ_{mech} is used as a free parameter which is inverted for in such a way such that its pressure dependency fits the experiment data, as seen in figure (7a,b). The experimental curves reported for this sandstone have been fitted by using the material properties listed in table (1) and varying only V_{act} at different confining pressures we retrieve that in mudstone V_{act} is also following equation (22), with $\alpha_0 = 22.9$.

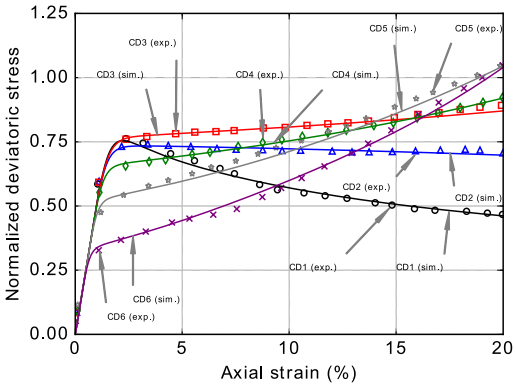

(a)

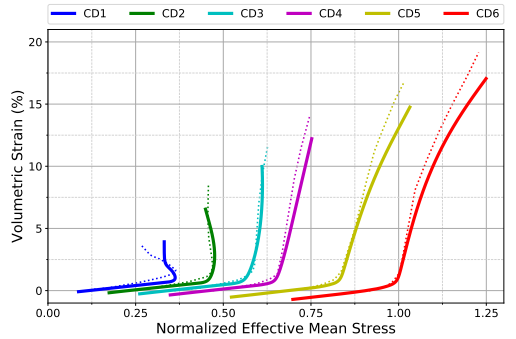

(b)

Figure 7: (a) The normalized (against the preconsolidation pressure) deviatoric stress (τ) vs. axial strain results for the experiments (symbols) and the numerical simulations (lines) for mudstone, (b) The volumetric strain versus the effective mean stress results for the experiments (dotted lines) and the numerical simulations (solid lines) for mudstone.

7 Numerical Regularization of Localization of Deformation

Geomaterials exhibit a spontaneous change of the deformation mode from uniform deformation towards either diffuse or localized failure patterns in the inelastic regime (see [VS95] for a comprehensive summary of the main results on this topic). Within the framework of bifurcation theory, this phenomenon can be modelled as a mathematical instability and, given an elasto-plastic constitutive law with a non-associative flow rule, it was shown that its onset can occur either in the strain hardening or in the strain softening regime [RR75]. As such, predicting a finite thickness of localization bands [MV87], or spacing between them [VRL15a, VRLW15], is a necessary feature of any model designed to describe the inelastic behaviour of geomaterials and their scale effect [SSV11, PV11, VSS12, VSS13, RSS$^+$17, RSS18a, RSS$^+$18b]. As shown by [Nee88], the combination of the momentum balance law and the rheology of a viscous material under simple shear fails to provide a finite thickness at the quasi-static limit of the equations. In such a case, the latter is equal to the size of a predetermined imperfection, contradicting the concept that localization stems from the constitutive description of the material and is a material property. Indeed, when neglecting the energy and mass balance laws, it is only by introducing inertia terms in the momentum balance law that one can "regularize" the problem of shear banding for a rate-dependent material by delaying its arrival to the stationary wave limit, as shown by [Slu92]. Using the present framework, where energy and mass balance laws are used as evolution equations for the state variables of the flow law, it was suggested in [PBRLV16] and shown in [Sar19] that the localization problem is indeed regularized (see also Fig. 8) and has a thickness (internal length) l given as a function of the activation enthalpy ΔQ_{mech} as follows:

$$l \propto \exp\left(\frac{\Delta Q_{mech}}{RT}\right) \tag{23}$$

8 Synthesis of the Results

In this work the suggested flow law has been calibrated for triaxial compression experiments in various materials. The dependence of the material's parameters on pressure, temperature and strain rate has been shown to be captured adequately by the model, with the power law parameters $\dot{\epsilon}_0$ and m encapsulating the strain rate effects and the activation enthalpy Q_{mech} of the material encompassing thermal and pressure sensitivity:

$$\Delta Q_{mech} = \Delta Q^0_{mech} + \Delta p_f V_{act}(P_c^{max}, T) \tag{24}$$

where ΔQ^0_{mech} is a reference activation enthalpy. It has been shown that ΔQ_{mech} in the present framework acts as a hardening function for the visco-plastic flow law, encompassing physical information of the system on its state variables (temperature

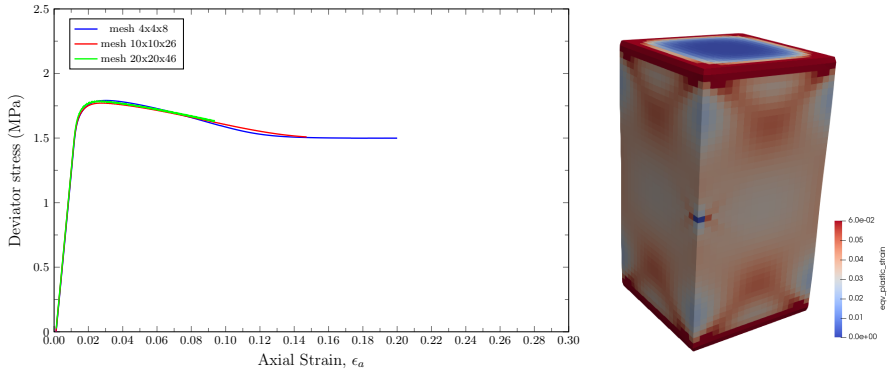

Figure 8: (left) Mesh sensitivity analysis showing the deviatoric stress (τ) vs. axial strain results different simulations of the low confinement experiment (CD1) with different mesh sizes, (right) Distribution of the equivalent plastic strain on a prismatic sample (mudstone) showing the shear bands

and porosity/pore pressure). The results presented so far demonstrated the ability of the model to capture rock behaviours under various conditions and further work to express more precisely the mechanisms operating in ΔQ_{mech}, including to better constrain the values of all respective parameters, could provide this model predictive capabilities beyond laboratory conditions.

8.1 Internal interface mechanisms expressed through the activation volume

From the analysis of all the experimental results, the activation volume V_{act} was shown to obtain a logarithmic dependency with the confining stress (22), that has the form:

$$V_{act} = \alpha_0 \frac{RT}{\ln P_{cs}/p_0} \ln \frac{P_{cs}}{p_{c(max)}} \tag{25}$$

where P_0 is the reference (preconsolidation) pressure, and P_{cs} is a stress path dependent quantity, representing the initial confining pressure corresponding to the critical state for a given stress path. One may immediately observe that this is a relationship akin to Kelvin's equation [F.R71] for curved liquid-vapour interfaces,

$$\gamma = \frac{rRT}{2V_m} \ln\left(\frac{\pi}{\pi_0}\right), \tag{26}$$

where π and π_0 represent the actual and saturated vapour pressures, r the radius of a droplet, V_{m} the molar volume of the liquid, γ the surface tension, R the universal gas

constant and T the temperature. Since Kelvin's law describes the pressure in a liquid-vapor interface, like water bridges in unsaturated samples, the inverted logarithmic law for V_{act} of equation (25) could be seen as expressing the pressure experienced by any grain interface, like solid bridges (cement), water bridges (capillary forces), etc. What remains yet to be evaluated is the physical meaning and processes represented by the fugacity coefficients assumed in the theoretical construction of the model.

8.2 Comparison with the theoretical results

Indeed, the considerations of the energetics of the interface processes between the fluid phase and the solid phase led to the following expression for V_{act}:

$$V_{act} = \phi_0 \beta_\phi n_c \frac{\rho_f}{\rho_0} \left(\ln \nu_f - \frac{\rho_{sk}}{\rho_f} \ln \nu_{sk} \right) RT \tag{27}$$

Comparing the outcomes of the inversion process (Eq. 25) with the theoretical result of Eq. 27 allows us to equate the two expressions. This procedure provides the following expressions for the coefficient α_0 and the fugacity coefficients ν_{sk}, ν_f:

$$\alpha_0 = p_0 \frac{\rho_f}{\rho_0} \phi_0 \beta_\phi n_c \ln \frac{P_{cs}}{P_0} \tag{28}$$

$$\ln \frac{P_{cs}/p_0}{P_{c(max)}/p_0} = \ln \frac{\nu_f}{\nu_{sk}^{\rho_{sk}/\rho_f}} \Longleftrightarrow \nu_f = \frac{P_{cs}}{p_0} \text{ and } \nu_{sk} = \left[\frac{P_{c(max)}}{p_0} \right]^{\frac{\rho_f}{\rho_{sk}}} \tag{29}$$

For a modified Cam-Clay (mCC) type of yield envelope in triaxial loading, $P_{cs} = \frac{p_0}{2}\left(1 - \frac{M}{\omega}\right)$, where ω is the slope of the stress path ($\omega = 3$ in triaxial loading).

We are therefore deducing that:

1. α_0 is a stress-path dependent pore compressibility quantity, expressing how compressible the porous structure is under a given loading-path. It is maximum ($\alpha_0 \to \infty$) when the material is loaded in isotropic conditions ($\omega \to 0$) and minimum ($\alpha_0 \to -0.69 \frac{p_0 \rho_f \phi_0 \beta_\phi n_c}{\rho_0}$) when the material is loaded in purely deviatoric conditions ($\omega \to \infty$). This intuitive result confirms the experimental observations in sedimentary rocks, suggesting that when materials are loaded in direct shear (i.e. under purely deviatoric conditions) they can deform with minimum pore structure change. This phenomenon (pore structure collapse) is the most pronounced at isotropic compression, as the present approach also concluded.

2. the fugacity coefficient of the fluid phase ν_f is also stress-path dependent and equal to $\frac{P_{cs}}{p_0} = \frac{1}{2}\left(1 - \frac{M}{\omega}\right)$, for a mCC-like material. It determines the effective pressure in the chemical potential of the fluid phase, expressing that the vigorousness of the fluid phase to participate in interface processes depends on the type of mechanical loading the material undergoes. It can only admit positive values, as it consists the argument of the logarithmic part of the chemical

potential, something achieved when $\omega > M$, i.e. when the material is loaded at stress-paths with slopes larger than the critical state line's. This means that skeleton-fluid interface processes are dominant when the deviatoric component of the loading path is preponderant with respect to its isotropic counterpart. Reciprocally, it means that during isotropic compression, volumetric mechanisms of the skeleton (e.g. grain breakage, pore collapse) would prevail over surface (interface) processes between solid and fluid.

3. the fugacity coefficient of the skeleton ν_{sk} is equal to $\left[\frac{P_{c(max)}}{p_0}\right]^{\frac{\rho_f}{\rho_{sk}}}$, i.e. a power of the maximum pressure the material has experienced $P_{c(max)}$, or equivalently of the minimum Overconsolidation Ratio (OCR) a mCC-type material can admit, $\frac{P_{c(max)}}{p_0}$. The power law is a ratio of the densities, $\frac{\rho_f}{\rho_{sk}}$, becoming linear when the fluid phase has the same density as the solid phase, i.e. at processes like debonding where parts of the solid skeleton get debonded and released in a "fluidized" state.

8.3 Transition from brittle to ductile regime

As it became apparent from the performance of the suggested theory against triaxial data of sandstone and mudstone, the model can transition from a brittle to a ductile response with increasing confinement. The main driver for the model to be able to transition between the two regimes is the change of sign of V_{act}, being negative in the brittle and positive in the ductile regime, as shown by [SAP+20].

By comparing the experimentally derived expression of V_{act}, Eq. (25), we conclude that this change of sign is happening when $P_{cs} = P_{c(max)}$, with $P_{cs} < P_{c(max)}$ being in the brittle regime. This outcome is confirming the experimental observations based on stresses. From the theoretical one of Eq. (27), we obtain that this change of sign is happening when $\nu_f^{\rho_f} = \nu_{sk}^{\rho_{sk}}$, with $\nu_f^{\rho_f} < \nu_{sk}^{\rho_{sk}}$ being in the brittle regime. This in turns means that, when the partial pressure experienced by the skeleton part of the interface is larger than the partial pressure experienced by the fluid (within a power law exponent $\frac{\rho_{sk}}{\rho_f}$), then the material will follow the predominant solid component and exhibit brittle response. We are therefore in a position to interpret the macroscopic response of rocks based on the microscopic interface process at hand.

8.4 Application to fault reactivation

Fluid injection or production in petroleum reservoirs affects the reservoir stresses such that it can even sometime reactivate dormant faults in the vicinity. In the particular case of deep carbonate reservoirs, faults can also be chemically active and chemical dissolution of the fault core can transform an otherwise impermeable barrier to a flow channel. Due to the scale separation between the fault and the reservoir, the implementation of highly non-linear multiphysics processes for the fault, needed for such phenomenon, is not compatible with simpler poromechanics controlling the reservoir behaviour. Recently, [LPV20b] presented a three-scale finite element framework us-

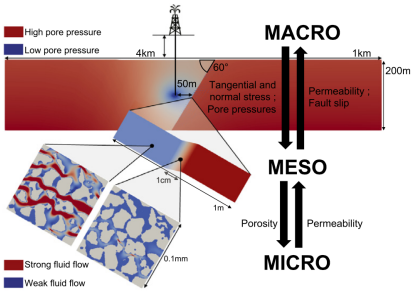

(a) Schematic of the fault's three different scales, displaying the apparent scale separation, and their couplings.

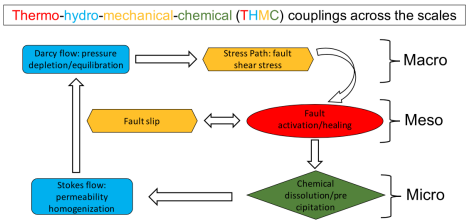

(b) Diagram showing a simplified loop of coupled scales and physics allowing for fault reactivation and healing. A blue box represents a hydraulic mechanism; yellow is mechanical; red is thermal; green is chemical.

Figure 9: Schematic of the multiscale fault reactivation framework in terms of scale separation and coupled processes. From [LPV20b]

ing the REDBACK simulator to solve for the field equations and models presented here (see fig. 9), thereby accounting for those multiphysics couplings in faults during fluid production. This approach linked the reservoir (km) scale – implementing poromechanics both for the fault interface and its surrounding reservoir – with the fault at the meso-scale (m) – implementing a THMC reactivation model [VAV10] – and the micro-scale (μm) – implementing a hydro-chemical model on meshed μCT-scan images. Through this work, we can explain the permeability increase during fault reactivation and successfully replicate fault activation, slip evolution and deactivation features, predicted by common fault reactivation models, yet with continuous transitions between the sequences. [LPV20b] showed that multiscale coupling allows to resolve the heterogeneous propagation of the fault slip which can be uncorrelated from the initial highest slip tendency location. They also demonstrated the advantage of dynamically upscaled laws compared to empirical ones as we show that a hydraulically imperceptible alteration of the microstructure's geometry can lead to different durations of the reactivation event at the macro-scale.

The main result of the work was that the fault reactivation sequence follows the bifurcation analysis of the dynamic system of pdes. Indeed, slippage of the fault results at the macro-scale in a horizontal elastic relaxation of the reservoir. This stress drop tends to bring back the fault towards a deactivated state, competing with the pressure depletion which keeps it activated. Given the difference of rates of those two processes, with pressure diffusing much slower than the fault slips, the stress decreases faster than the strain rate increases. This relaxation decreases the shearing stress at the fault. After a sufficient decrease, the stress reaches a low enough value where the fault cannot remain in its activated state and returns to the lower branch of the S-curve. The temperature and slip velocity return to their initial value and the fault goes back to its initial slow creep regime. Correspondingly, the permeability goes back to its initial low value as the reversible temperature-activated calcite decomposition reaction switches from forward to reverse direction. The chemical dissolution responsible for

the large increase of permeability gives way to its opposite reaction, which heals the fault by precipitating calcite at its core.

For the generic scenario selected, the whole reactivation event lasts for 250 days. Note the small thickness of reservoir leads the slip to propagate to the limits of the domain and the whole reservoir therefore accommodates the same vertical displacement jump as the fault. The fact that the reactivated fault splits the whole reservoir leads to an artificially increased period of slip. Considering a much deeper section of the reservoir, as well as its 3D nature, would be required to model appropriately a more precise duration of the whole slip event. This example illustrates nonetheless the ability of the approach to capture the physical couplings responsible for the activation, permeability increase and deactivation. Note that in any case we do expect a longer opening compared to a brittle fault slip, as it is an important characteristic of ductile faults, along with the aseismic nature of the slip.

Another important point is that the reactivation on the fault tends to propapagate along its length. Indeed, the reactivation of the first fault segment occurs at a specific location determined by the heterogeneous stress distribution along the fault, due to the radial diffusion of pressure depletion around the well coupled with gravitational effects. This first slip triggers a cascading chain of events, as the slip of one point of the fault directly impacts the stress state of the neighbouring fault segments. In the particular example studied, the slip propagates along the whole fault, leading to a complete synchronisation of the fault slippage.

The location of the first slip event corresponds to the zone of highest stress, but, interestingly, it is not directly linked to the pressure depletion profile. Using the stress path explained earlier, this translates to a maximum shear stress around the middle of the fault, which can be taken as proxy for fault stability, as usually done to assess slip tendency for faults in the plastic regime. We can then see that the middle of the fault, where the pressure depletion is the highest, has the highest tendency of reactivating. Yet, the multiscale couplings between the fault and the reservoir lead to a more complex problem of interferences between all segments of the fault and we actually observe an initial reactivation of the fault at the top of the model, as can be seen on the timelapse of reactivation in Fig. 21 of [LPV20b].

Once the first fault segment reactivates, the fault starts slipping, i.e. creeping at a much faster rate. The same couplings responsible for the initial reactivation remain at play afterwards and lead to a cascading transfer of forces from that location to the neighbouring fault segments, causing a sequential reactivation of those segments. Slippage is indeed known to propagate much further away than just the surroundings the fault. Following the phase of propagation that ends with the last reactivation event at the bottom of the reservoir, we observe in Fig. 21 of [LPV20b], a synchronisation of the whole fault.

9 Conclusions

This study proposes a multi-physics constitutive framework for elasto-visco-plastic materials. This framework accounts for the effect of interface processes and uses a hardening law of plasticity that depends on global and internal variables like temperature, pressure, density, and chemical potentials. The evolution of these variables is governed by the fundamental laws of mass and energy balance. We've incorporated the impact of grain contact and surface processes by upscaling the system's internal enthalpy. The model has been validated against various materials and tests, showing strong agreement within a realistic range of parameters. The analysis also revealed that the simulation results offer sufficient data to constrain the parameters for the mechanical enthalpy, highlighting the value of combining data-driven and physics-based methods.

Based on experimental validation, we reached several key conclusions:

The primary mechanism controlling the model's response in triaxial compression tests is an internal interface mechanism between the rock skeleton and the pore fluid. This is similar to the capillary forces described by Kelvin's law.

This interface process is stress-path dependent, becoming more significant under loading with a large deviatoric component (shear). In pure isotropic compression, energy dissipation seems to focus more on volumetric processes like pore collapse or grain breakage rather than on interface physics.

The interface model provides a physical understanding of the different mechanisms at play during volumetric versus shear-enhanced loading. Since experimental data on these specific mechanisms is limited, our model's interface mechanisms were defined based on the energy required to match the experimental results. This encourages future experimental research to investigate these aspects in more detail. Nevertheless, our energetic approach already allows for a quantitative understanding of the underlying processes that cause the different—and expected—behaviors under these two types of deformation. This opens the door to future work to fully validate the model's stress-path dependency.

References

[AC79] Samuel M. Allen and John W. Cahn. A microscopic theory for antiphase boundary motion and its application to antiphase domain coarsening. *Acta Metallurgica*, 27(6):1085–1095, 1979.

[AMR+19] Ryan T. Armstrong, James E. McClure, Vanessa Robins, Zhishang Liu, Christoph H. Arns, Steffen Schlüter, and Steffen Berg. Porous media characterization using Minkowski functionals: theories, applications and future directions. *Transport in Porous Media*, 130(1):305–335, 2019.

[AO82] T. Adachi and F. Oka. Constitutive equations for normally conslidated clay based on elasto-viscoplasticity. *Soils and Foundations*, 22(4):57–70, 1982.

[AS06] Peter Augat and Sandra Schorlemmer. The role of cortical bone and its microstructure in bone strength. *Age and Ageing*, 35:27–31, 2006.

[BDK+99] Donald Brown, Robert DuTeaux, Paul Kruger, Daniel Swenson, and Tsutomu Yamaguchi. Fluid circulation and heat extraction from engineered geothermal reservoirs. *Geothermics*, 28(4):553–572, 1999.

[BE21] Giuseppe Buscarnera and Itai Einav. The mechanics of brittle granular materials with coevolving grain size and shape. *Proceedings the Royal Society A*, 477, 2021.

[BFS+15] R.M. Brannon, T.J. Fuller, O.E. Strack, A.F. Fossu, and J.J. Sanchez. Kayenta: Theory and user's guide. Sandia Report SAND2015-0803, Sandia National Laboratories, 2015.

[Bor91] Ronaldo I Borja. Cam-clay plasticity, part ii: Implicit integration of constitutive equation based on a nonlinear elastic stress predictor. *Computer Methods in Applied Mechanics and Engineering*, 88(2):225–240, 1991.

[BSO19] Swastibrata Bhattacharyya, Ryoji Sahara, and Kaoru Ohno. A first-principles phase field method for quantitatively predicting multi-composition phase separation without thermodynamic empirical parameter. *Nature Communications*, 10(1):1–2, 2019.

[CRG13] Delphine Croizé, François Renard, and Jean Pierre Gratier. Compaction and porosity reduction in carbonates: a review of observations, theory, and experiments. In *Advances in geophysics*, volume 54, pages 181–238. Elsevier, 2013.

[CRN+20] Sehyun Chun, Sidhartha Roy, Yen Thi Nguyen, Joseph B. Choi, H. S. Udaykumar, and Stephen S. Baek. Deep learning for synthetic microstructure generation in a materials-by-design framework for heterogeneous energetic materials. *Scientific Reports*, 10(1):1–15, 2020.

[DNB+14] Thomas Dewers, Pania Newell, Scott Broome, Jason Heath, and Steve Bauer. Geomechanical behavior of cambrian mount simon sandstone reservoir lithofacies, iowa shelf, usa. *International Journal of Greenhouse Gas Control*, 21:33 – 48, 2014.

[DP52] Daniel Charles Drucker and William Prager. Soil mechanics and plastic analysis or limit design. *Quarterly of applied mathematics*, 10(2):157–165, 1952.

[Ein07] Itai Einav. Breakage mechanics-Part I: Theory. *Journal of the Mechanics and Physics of Solids*, 55(6):1274–1297, 2007.

[Ein12] Itai Einav. The unification of hypo-plastic and elasto-plastic theories. *International Journal of Solids and Structures*, 49(11):1305 – 1315, 2012.

[Eyr36] Henry Eyring. Viscosity, plasticity, and diffusion as examples of absolute reaction rates. *The Journal of chemical physics*, 4(4):283–291, 1936.

[FA82] H.J. Frost and M.F. Ashby. *Deformation-mechanism maps: the plasticity and creep of metals and ceramics*. Pergamon Press, 1982.

[FB06] A. F. Fossum and R. M. Brannon. On a viscoplastic model for rocks with mechanism-dependent characteristic times. *Acta Geotechnica*, 1(2):89–106, Sep 2006.

[FP89] George J Fischer and Mervyn S Paterson. Dilatancy during rock deformation at high temperatures and pressures. *Journal of Geophysical Research: Solid Earth*, 94(B12):17607–17617, 1989.

[F.R71] Sir William Thomson F.R.S. Lx. on the equilibrium of vapour at a curved surface of liquid. *The London, Edinburgh, and Dublin Philosophical Magazine and Journal of Science*, 42(282):448–452, 1871.

[FRG+19] Eirini A. Fragogeorgi, Maritina Rouchota, Maria Georgiou, Marisela Velez, Penelope Bouziotis, and George Loudos. In vivo imaging techniques for bone tissue engineering. *Journal of Tissue Engineering*, 10, 2019.

[GCH15] Alessandro Gajo, Francesco Cecinato, and Tomasz Hueckel. A microscale inspired chemo-mechanical model of bonded geomaterials. *International Journal of Rock Mechanics and Mining Sciences*, 80:425 – 438, 2015.

[GEC+10] Albert Genter, Keith Evans, Nicolas Cuenot, Daniel Fritsch, and Bernard Sanjuan. Contribution of the exploration of deep crystalline fractured reservoir of soultz to the knowledge of enhanced geothermal systems (egs). *Comptes Rendus Geoscience*, 342(7):502–516, 2010. Vers l'exploitation des ressources géothermiques profondes des systèmes hydrothermaux convectifs en milieux naturellement fracturés.

[GNHLG09] D. Gaston, C. Newman, G. Hansen, and D. Lebrun-Grandi. Moose: A parallel computational framework for coupled systems of nonlinear equations. *Nuclear Engineering and Design*, 239(10):1768–1778, Oct 2009.

[GRV19] Alexandre Guevel, Hadrien Rattez, and Manolis Veveakis. Contact phase-field modeling for chemo-mechanical degradation processes. Part II: Numerical applications with focus on pressure solution. 2019.

[GRV20] A. Guével, H. Rattez, and E. Veveakis. Viscous phase-field modeling for chemo-mechanical microstructural evolution: application to geomaterials and pressure solution. *International Journal of Solids and Structures*, 207:230–249, 2020.

[GRVon] A. Guével, H. Rattez, and E. Veveakis. Morphometric description of strength and degradation in porous media. *International Journal of Solids and Structures*, in revision.

[HB90] T. Hueckel and G. Baldi. Thermoplasticity of saturated clays: Experimental constitutive study. *Journal of Geotechnical Engineering*, 116(12):1778, 1990.

[HFL09] T. Hueckel, B. François, and L. Laloui. Explaining thermal failure in saturated clays. *Géotechnique*, 59(3):197–212, 2009.

[Hil63] R. Hill. Elastic properties of reinforced solids: Some theoretical principles. *Journal of the Mechanics and Physics of Solids*, 11(5):357 – 372, 1963.

[HLK+02] Jacques M Huyghe, R Van Loon, Patricia M Van Kemenade, Theo H Smit, and Blood Perfusion. We all are porous media. *Poromechanics II*, pages 17–28, 2002.

[Kar08] S. Karato, editor. *Deformation of Earth Materials*. Cambrige University Press, 2008.

[Kau41] Walter Kauzmann. Flow of solid metals from the standpoint of the chemical-rate theory. *Trans. AIME*, 143:57–83, 1941.

[KAVA18] Reid Kawamoto, Edward Andò, Gioacchino Viggiani, and José E. Andrade. All you need is shape: Predicting shear banding in sand with LS-DEM. *Journal of the Mechanics and Physics of Solids*, 111(November):375–392, 2018.

[LC03] L. Laloui and C. Cekerevac. Thermo-plasticity of clays: An isotropic yield mechanism. *Computers and Geotechnics*, 30(8):649 – 660, 2003.

[LCVP17] Martin Lesueur, Maria Camila Casadiego, Manolis Veveakis, and Thomas Poulet. Modelling fluid-microstructure interaction on elasto-visco-plastic digital rocks. *Geomechanics for Energy and the Environment*, 12:1–13, 2017.

[Lin19] J. Lin. Inversion workflow for multiphysics modelling of triaxial experiments. Master's thesis, UNSW Minerals and Energy Resources Engineering, 2019.

[LLC08] L. Laloui, S. Leroueil, and S. Chalindar. Modelling the combined effects of strain rate and temperature on one-dimensional compression of soils,. *Can. Geotech. J.*, 45:173 – 194, 2008.

[LPD+25] W. Lindqwister, J. Peloquin, L. E. Dalton, K. Gall, and M. Veveakis. Predicting compressive stress-strain behavior of elasto-plastic porous media via morphology-informed neural networks. *Communications Engineering*, 4(1):73, 2025.

[LPV20a] Martin Lesueur, Thomas Poulet, and Manolis Veveakis. Permeability Hysteresis From Microchannels Opening During Dissolution/Reprecipitation Cycle. *Geophysical Research Letters*, 47(18):1–8, 2020.

[LPV20b] Martin Lesueur, Thomas Poulet, and Manolis Veveakis. Three-scale multiphysics finite element framework (FE3) modelling fault reactivation. *Computer Methods in Applied Mechanics and Engineering*, 365, 2020.

[LSA+20] Jack Lin, Mustafa Sari, Sotiris Alevizos, Manolis Veveakis, and Thomas Poulet. A heuristic model inversion for coupled thermo-hydro-mechanical modelling of triaxial experiments. *Computers and Geotechnics*, 117:103278, 2020.

[Lub90] Jacob Lubliner. *Plasticity theory*. Macmillan Publishing Company, New York, 1990.

[MV87] H. B. Muhlhaus and I. Vardoulakis. Thickness of shear bands in granular materials. *Geotechnique*, 37(3):271–283, 1987.

[Nee88] A. Needleman. Material rate dependence and mesh sensitivity in localization problems. *Computer Methods in Applied Mechanics and Engineering*, 67(1):69 – 85, 1988.

[NEM09] André Niemeijer, Derek Elsworth, and Chris Marone. Significant effect of grain size distribution on compaction rates in granular aggregates. *Earth and Planetary Science Letters*, 284(3-4):386–391, 2009.

[Oka81] Fusao Oka. Prediction of time-dependent behaviour of clay. *Soil mechanics and foundation engineering. Proc. 10th international conference, Stockholm, June 1981. Vol. 1, (A.A.Balkema)*, 1:215–218, 01 1981.

[Oka85] F Oka. Elasto/viscoplastic constitutive equations with memory and internal variables. *Computers and geotechnics*, 1(1):59–69, 1985.

[OKH+11] F. Oka, S. Kimoto, Y. Higo, H. Ohta, T. Sanagawa, and T. Kodaka. An elasto-viscoplastic model for diatomaceous mudstone and numerical simulation of compaction bands. *International Journal for Numerical and Analytical Methods in Geomechanics*, 35(2):244–263, 2011.

[Oro40] E Orowan. Problems of plastic gliding. *Proceedings of the Physical Society*, 52(1):8–22, jan 1940.

[O'S11] Catherine O'Sullivan. *Particulate discrete element modelling: a geomechanics perspective*. Spon Press, 2011.

[PBRLV16] Martin Paesold, Andrew Bassom, Klaus Regenauer-Lieb, and Manolis Veveakis. Conditions for the localisation of plastic deformation in temperature sensitive viscoplastic materials. *Journal of Mechanics of Materials and Structures*, 11(2):113–136, 2016.

[PE10] Nikolas Provatas and Ken Elder. Phase-field methods in material science and engineering. *Wiley-VCH*, page 312, 2010.

[Per66] Piotr Perzyna. Fundamental Problems in Viscoplasticity. *Advances in Applied Mechanics*, 9(C):243–377, 1966.

[PPV16] Thomas Poulet, Martin Paesold, and Emmanuil Veveakis. Multi-physics modelling of fault mechanics using redback - a parallel open-source simulator for tightly coupled problems. *Rock Mechanics and Rock Engineering*, pages 1–17, 2016.

[PV11] Stefanos-Aldo Papanicolopulos and Emmanuil Veveakis. Sliding and rolling dissipation in cosserat plasticity. *Granular Matter*, 13(3):197–204, Jun 2011.

[PV16] Thomas Poulet and Manolis Veveakis. A viscoplastic approach for pore collapse in saturated soft rocks using redback: An open-source parallel simulator for rock mechanics with dissipative feedbacks. *Computers and Geotechnics*, 74:211 – 221, 2016.

[RB68] K.H. Roscoe and John Burland. On the generalized stress-strain behavior of wet clays. *Cambridge University Press*, 01 1968.

[Ric06] J. R. Rice. Heating and weakening of faults during earthquake slip. *J. Geophys. Res.*, 111:B05311, 2006.

[RLBC+15] Klaus Regenauer-Lieb, Andrew Bunger, Hui Tong Chua, Arcady Dyskin, Florian Fusseis, Oliver Gaede, Rob Jeffrey, Ali Karrech, Thomas Kohl, Jie Liu, Vladimir Lyakhovsky, Elena Pasternak, Robert Podgorney, Thomas Poulet, Sheik Rahman, Christoph Schrank, Mike Trefry, Manolis Veveakis, Bisheng Wu, David A. Yuen, Florian Wellmann, and Xi Zhang. Deep geothermal: The 'moon landing'mission in the unconventional energy and minerals space. *Journal of Earth Science*, 26(1):2–10, 2015.

[RLR01] James R. Rice, Nadia Lapusta, and K. Ranjith. Rate and state dependent friction and the stability of sliding between elastically deformable solids. *Journal of the Mechanics and Physics of Solids*, 49(9):1865 – 1898, 2001. The {JW} Hutchinson and {JR} Rice 60th Anniversary Issue.

[RR75] J.W. Rudnicki and J.R. Rice. Conditions for the localization of deformation in pressure sensitive dilatant materials. *J. Mech. Phys. Solids*, 23:371–394, 1975.

[RRRH00] P. Rosakis, A.J. Rosakis, G. Ravichandran, and J. Hodowany. A thermodynamic internal variable model for the partition of plastic work into heat and stored energy in metals. *Journal of the Mechanics and Physics of Solids*, 48(3):581 – 607, 2000.

[RSS+17] H. Rattez, I. Stefanou, J. Sulem, M. Veveakis, and T. Poulet. Localisation of deformation for shearing of a fault gouge with cosserat microstructure and different couplings. In Euripides Papamichos, Panos Papanastasiou, Elena Pasternak, and Arcady Dyskin, editors, *Bifurcation and Degradation of Geomaterials with Engineering Applications*, pages 155–160, Cham, 2017. Springer International Publishing.

[RSS18a] Hadrien Rattez, Ioannis Stefanou, and Jean Sulem. The importance of thermo-hydro-mechanical couplings and microstructure to strain localization in 3d continua with application to seismic faults. part i: Theory and linear stability analysis. *Journal of the Mechanics and Physics of Solids*, Accepted, 03 2018.

[RSS+18b] Hadrien Rattez, Ioannis Stefanou, Jean Sulem, Manolis Veveakis, and Thomas Poulet. The importance of thermo-hydro-mechanical couplings and microstructure to strain localization in 3d continua with application to seismic faults. part ii: Numerical implementation and post-bifurcation analysis. *Journal of the Mechanics and Physics of Solids*, 115:1 – 29, 2018.

[SAP+20] Mustafa Sari, Sotiris Alevizos, Thomas Poulet, Jack Lin, and Manolis Veveakis. A visco-plastic framework for interface processes in sedimentary reservoir rocks at HPHT conditions. *Geomechanics for Energy and the Environment*, 22:100165, 2020.

[Sar19] M. Sari. *A multi-physics visco-plasticity theory for porous sedimentary rocks*. PhD thesis, UNSW Minerals and Energy Resources Engineering, 2019.

[Slu92] L.J. Sluys. *Wave Propagation, Localisation and Dispersion in Softening Solids*. PhD thesis, Technische University, 01 1992.

[SPS18] Vânia Regina Salvini, Victor C. Pandolfelli, and Dirceu Spinelli. Mechanical properties of porous ceramics. *Recent Advances in Porous Ceramics*, 2018.

[SSV11] Jean Sulem, Ioannis Stefanou, and Manolis Veveakis. Stability analysis of undrained adiabatic shearing of a rock layer with cosserat microstructure. *Granular Matter*, 13:261–268, 06 2011.

[Ter25] Karl Terzaghi. *Erdbaumechanik auf bodenphysikalischer grundlage*. Leipzig ; Wien : F. Deuticke, 1925.

[TQ34a] G. Taylor and H. Quinney. The latent energy remaining in a metal after cold working. *Proc. R. Soc., Ser. A.*, 143:307 – 326., 1934.

[TQ34b] G. Taylor and H. Quinney. The latent energy remaining in a metal after cold working. *Proc. R. Soc., Ser. A.*, 143:307 – 326., 1934.

[VAV10] E. Veveakis, S. Alevizos, and I. Vardoulakis. Chemical reaction capping of thermal instabilities during shear of frictional faults. *Journal of the Mechanics and Physics of Solids*, 58(9):1175–1194, 2010.

[vdENS19] M. P.A. van den Ende, A. R. Niemeijer, and C. J. Spiers. Influence of grain boundary structural evolution on pressure solution creep rates. *Journal of Geophysical Research: Solid Earth*, 124(10):10210–10230, 2019.

[VPA14] E. Veveakis, T. Poulet, and S. Alevizos. Thermo-poro-mechanics of chemically active creeping faults. 1: Theory and steady state considerations. *Journal of Geophysical Research: Solid Earth*, 119(6):4583–4605, 2014.

[VRL15a] E Veveakis and Regenauer-Lieb. Cnoidal waves in solids. *Journal of Mechanics and Physics of Solids*, 78:231–248, 2015.

[VRL15b] E. Veveakis and K. Regenauer-Lieb. Review of extremum postulates. *Current Opinion in Chemical Engineering*, 7(0):40–46, 2015.

[VRLW15] E. Veveakis, K. Regenauer-Lieb, and R.F. Weinberg. Ductile compaction of partially molten rocks: the effect of non-linear viscous rheology on instability and segregation. *Geophysical Journal International*, 200(1):519–523, 2015.

[VS95] I. Vardoulakis and J. Sulem, editors. *Bifurcation Analysis in Geomechanics*. Blankie Acc. and Professional, 1995.

[VSS12] Emmanuil Veveakis, Jean Sulem, and Ioannis Stefanou. Modeling of fault gouges with cosserat continuum mechanics: Influence of thermal pressurization and chemical decomposition as coseismic weakening mechanisms. *Journal of Structural Geology*, 38:254 – 264, 2012. Physico-Chemical Processes in Seismic Faults.

[VSS13] E. Veveakis, I. Stefanou, and J. Sulem. Failure in shear bands for granular materials: thermo-hydro-chemo-mechanical effects. *Geotechnique Let.*, 3(2):31–36, 2013.

[WDZ97] T. Wong, C. David, and W. Zhu. The transition from brittle faulting to cataclastic flow in porous sandstones: Mechanical deformation. *Journal of Geophysical Research: Solid Earth*, 102(B2):3009–3025, 1997.

[WKM+02] N. J. Wachter, G. D. Krischak, M. Mentzel, M. R. Sarkar, T. Ebinger, L. Kinzl, L. Claes, and P. Augat. Correlation of bone mineral density with strength and microstructural parameters of cortical bone in vitro. *Bone*, 31(1):90–95, 2002.

[ZB17] Yida Zhang and Giuseppe Buscarnera. A rate-dependent breakage model based on the kinetics of crack growth at the grain scale. *Ge?otechnique*, 02 2017.

Physical model experiments in geomechanics for the energy transition

Hadrien Rattez, Luc Simonin, Pauline André

Institute of Mechanics Materials and Civil Engineering, UCLouvain, Louvain-la-Neuve, Belgium

The global energy transition requires developing reliable and cost-effective subsurface infrastructure, ranging from offshore wind foundations to CO_2 sequestration wells. Physical modeling offers a practical approach to investigate design strategies and validate numerical tools under complex conditions. This chapter outlines the principles of scaling laws essential for translating physical (smaller scale) model results to real-world applications. Key concepts of dimensional analysis, both equation-based and variable-based are introduced with examples. The role of centrifuge testing in replicating stress-dependent soil behavior is emphasized. Practical limitations of physical modeling such as partial similarity and Thermo-Hydro-Chemo-Mechanical couplings challenges are discussed in the context of subsurface energy infrastructures. Even when full similarity cannot be achieved, informed scaling enables partial similarity to provide meaningful insights, ensuring that model results remain interpretable and applicable to design.

1 Introduction

The global energy transition, driven by the alarming reports of the IPCC for climate change [Int23] increasingly relies on subsurface resources and infrastructures. This urgent transition is associated to the need to reduce greenhouse gas emissions across the full energy sector, including a substantial reduction in overall fossil fuel use (high confidence) as one of the key source of carbon emissions [IPC23]. Examples of subsurface infrastructures treated in this doctoral school range from wind and geothermal energy, underground hydrogen storage to Carbon Capture and Sequestration (CCS). In this context, geomechanics plays a central role in understanding and controlling the behavior of geomaterials under evolving Thermal, Hydraulic, Mechanical, and Chemical (THMC) conditions associated to the deployment of such infrastructures at large scale [SR21].

Many of the technologies that are to be developed in a relatively short timescale for the energy transition require knowledge of geomaterials' behavior under unexplored conditions. It also requires the design of infrastructures that should last hundreds of thousands to up to 1 million years (Nuclear Waste Disposals) [Ram18], the design of piles much larger than in traditional civil engineering constructions (for Offshore Wind Turbines foundations) [SB21] or exposed to new types of loading like thermal cycles (for energy piles). Moreover, the high costs associated to the construction of those facilities limit the number of pilot projects to test different design strategies. For example, wells for deep geothermal systems for electricity production should reach a wellhead temperature of more than 100^oC, which corresponds to a depth of 2,000 to 5,000 meters [AWS14], and the associated cost to drill one well to this depth ranges from 3 to 15 million dollars in average [BM19] not including hydraulic stimulation, surface facilities or power plants. Injection wells for CO_2 underground storage must reach 800 meters for the CO_2 to remain in supercritical state (dense and liquid-like), which improves storage efficiency [BAP$^+$24], and typical wells are in between 800 and 3000 meters, with costs ranging from 1 to 3 million of dollars onshore (considering an average price of 1000 dollars per meters) to 7 to 24 million of dollars offshore (considering an average price of 8000 dollars per meters) [VHCV12]. A typical monopile, representing the majority of offshore wind turbine foundations, for a 5 MW turbine typically costs 2.4 million euros, with half of the price stemmming from the manufacturing process and the other half from the material [MB14]. The installation of such monopiles lasts 3 days in average and requires the use of specialised vessels allowing for large lifting height and crane capacity, which costs around 200,000 dollars per day [Jia21]. Thus, physical models (usually representing the prototype design at a smaller scale) offer an economical and more practical way to validate numerical models or tests different design strategies.

Physical modelling is used to investigate specific aspects of a prototype's behavior [Woo17]. While full-scale testing is a form of physical modelling, most models are built at reduced scales to allow quicker, more controlled studies. These scaled models often support parametric studies, where key variables are systematically varied to understand their effects. Multiple tests, and sometimes repeated trials, are typically needed to ensure reliable results [Woo17]. Karl von Terzaghi conducted some of the first physical modeling experiments in geotechnics for dams in the 1920s [Goo99], but the development of scaled model tests increased with the use of centrifuges to simulate soil behavior under scaled gravitational loads, first used by [Buc31] and [PF36], but widely applied by Andrew N. Schofield at Cambridge in the 1970s [Sch80]. However, to ensure that such experiments yield insights applicable to real-world systems, rigorous scaling laws must be employed [Woo17]. These laws allow researchers to interpret model results in terms of full-scale (prototype) behavior, but their application in the energy transition domain comes with significant challenges due to multi-physics interactions, heterogeneous materials, and complex boundary conditions.

This chapter aims at presenting the general methodology for setting up a scaled geomechanical model test of a given infrastructure in the laboratory (referred to as 1g-model tests because the gravity is not changed) or in the centrifuge (in which the

equivalent gravity is changed), examples of such model experiments, and challenges associated with them.

2 Fundamentals of scaling laws

When physical models are not full-scale, scaling laws are essential for translating observations to the prototype level (or in other words to the "real" scale). If materials behave linearly and uniformly under expected loads, scaling can be straightforward but the accuracy still depends on the theoretical framework behind the model [Woo17]. In typical geotechnical problems (like the soils' consolidation below a structure or the bearing capacity analysis of a foundation) model tests can be planned using standard scaling laws, commonly presented in table format in the literature [ITN05, GGS+07, Woo17].

However, most geomaterials present a nonlinear behavior and most engineering projects related to energy involve the couplings of various thermo-hydro-chemo-mechanical phenomena. It is thus especially important to understand the expected behavior and the theoretical laws governing its behavior, so the physical model can be accurately designed and the appropriate rules for extrapolating results are clear. This step is realized through the development of scaling laws, which ensure the similarity between the physical model and the real-world prototype so that they exhibit the same behavior under a set of non-dimensional parameters, even if their actual sizes, timescales, or other dimensions differ. The most direct similarity is geometric similarity, which ensures that the model and prototype have the same shape but different sizes. In fig1, an example of geometric similarity for an offshore wind turbine foundation is shown for a scale factor of 100. Dimensional analysis is used to identify the main dimensionless groups that govern a physical system. Dimensional analysis is essential for reliable extrapolation, as it ensures that a physical model will exhibit behavior similar to the prototype when both are governed by the same set of dimensionless groups. This analysis can be conducted in two different ways through equation-based or variable-based dimensional analysis.

2.1 Equation-based dimensional analysis

When the partial differential equation (PDE) governing the behavior of a system is known, dimensional analysis can be performed by starting from the PDE itself, such as the Navier-Stokes, diffusion, or consolidation equations. By introducing appropriate non-dimensional parameters, the equation can be reformulated in dimensionless form, revealing the key dimensionless groups that govern the system's behavior. These groups often define important physical regimes typically used in fluid mechanics or thermodynamics, such as short versus long timescales or diffusive versus convective heat transfers. They also help justify the omission of certain terms in equations when the dimensionless numbers associated with them are small compared to others.

In the following the equation-based dimensional analysis is applied to the consolida-

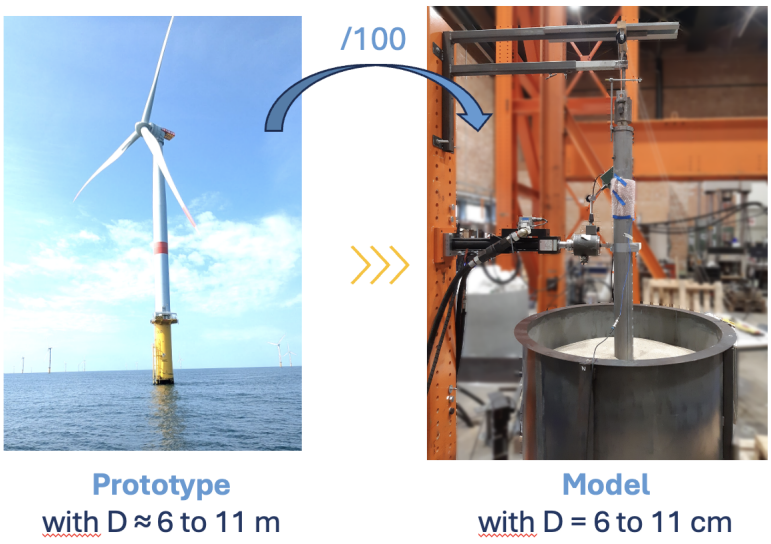

Figure 1: Schematic example of scaling strategy for an offshore wind turbine.

tion equation to highlight the different steps:

- Step 1: Governing equation (1D Consolidation Equation)

  The one-dimensional consolidation equation for a layer drained at the top and bottom (see fig.2(a)) is given by:

$$\frac{\partial u}{\partial t} = c_v \frac{\partial^2 u}{\partial z^2} \tag{1}$$

  where $u(z,t)$ is the excess pore water pressure, t is the time, z is the vertical spatial coordinate (depth) and c_v is the coefficient of consolidation (in m^2/s).

- Step 2: Introduce characteristic scales

  We define characteristic scales for the variables (they can also be considered as scale factors, see section 2.3):

$$z \sim H, \quad t \sim T, \quad u \sim U \tag{2}$$

  We introduce nondimensional variables:

$$z = H\hat{z}, \quad t = T\hat{t}, \quad u = U\hat{u} \tag{3}$$

where $\hat{z}, \hat{t}, \hat{u}$ are dimensionless quantities of order 1.

- Step 4: Apply scaling to the equation

  Using the chain rule:

$$\frac{\partial u}{\partial t} = \frac{U}{T}\frac{\partial \hat{u}}{\partial \hat{t}}, \quad \frac{\partial^2 u}{\partial z^2} = \frac{U}{H^2}\frac{\partial^2 \hat{u}}{\partial \hat{z}^2} \tag{4}$$

  Substitute into the original PDE:

$$\frac{U}{T}\frac{\partial \hat{u}}{\partial \hat{t}} = c_v \cdot \frac{U}{H^2}\frac{\partial^2 \hat{u}}{\partial \hat{z}^2} \tag{5}$$

  Divide by U and multiply by T both sides:

$$\frac{\partial \hat{u}}{\partial \hat{t}} = \frac{T.c_v}{H^2}\frac{\partial^2 \hat{u}}{\partial \hat{z}^2} \tag{6}$$

  In Eq.6, we obtain the dimensionless number controlling the consolidation process $\frac{T.c_v}{H^2}$, which should be the same for the physical model and the prototype to ensure similarity of the consolidation phenomenon.

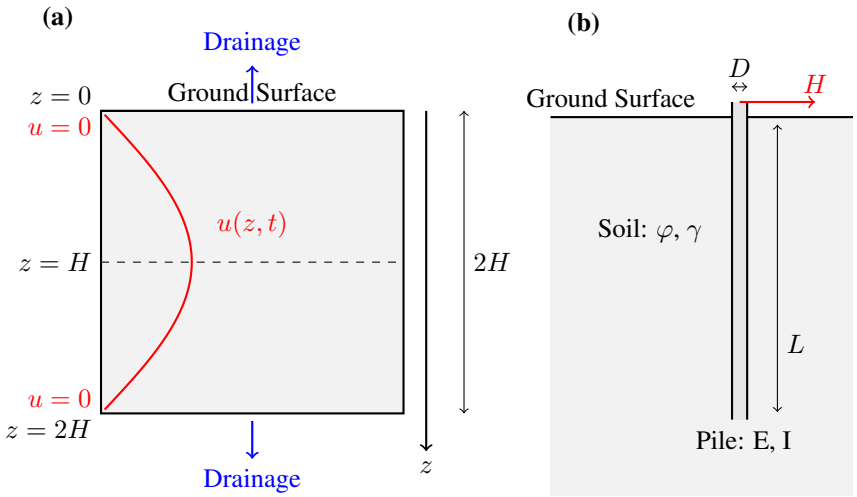

Figure 2: Schematic for the two examples used to describe: (a) equation-based dimensional analysis, a 1D layer in consolidation (b) variable-based scaling, a pile subjected to lateral force.

2.2 Variable-based dimensional analysis

When the governing equations of a physical phenomenon are unknown or too complex to derive (unlike the previous section), variable-based dimensional analysis provides a powerful alternative by focusing on the key variables that influence the system's behavior. This method involves identifying all relevant physical quantities and applying the Buckingham π theorem to reduce them into a set of independent dimensionless groups. These groups can then be analyzed or tested experimentally to uncover empirical relationships and scaling laws that characterize the system [Woo17, Bak21].

Originally formulated by Buckingham in 1914 [Buc14], the π theorem forms the cornerstone of dimensional analysis. It states that if a problem involves m physical variables and k fundamental dimensions, it can be reformulated in terms of $m - k$ dimensionless parameters. The Buckingham π method is the standard procedure for constructing these dimensionless groups. It begins with listing all relevant variables, then selecting k "repeating" or "governing" variables that are used to non-dimensionalize the remaining $m - k$ variables. Although systematic, the method presents challenges in practice, such as choosing appropriate repeating variables and determining the most suitable form of each dimensionless group from among many valid combinations [Woo17].

In the following, the variable-based dimensional analysis is applied to the lateral capacity of a pile (a problem of primary importance for offshore wind turbines as they are mainly loaded laterally by wind and waves) to highlight the different steps:

- Step 1: Identification of relevant variables

  To analyze the lateral load capacity H of a single pile embedded in cohesionless soil (see fig.2(b)), we begin by identifying the physical variables that influence this behavior. These include: the lateral load capacity H itself (with dimensions of force, $[MLT^{-2}]$); the embedment length of the pile L and its diameter D (both with dimensions of length, $[L]$); the unit weight of the soil γ (with dimensions $[ML^{-2}T^{-2}]$); the Young's modulus E of the pile material (with dimensions $[ML^{-1}T^{-2}]$); and the second moment of area I of the pile cross-section (with dimensions $[L^4]$). In addition, the soil's shear strength is characterized by the internal friction angle ϕ, which is a dimensionless parameter. These seven variables collectively describe the problem from a mechanical and geotechnical standpoint.

- Step 2: Buckingham's π theorem

  The problem involves three fundamental dimensions: mass $[M]$, length $[L]$, and time $[T]$. With a total of seven variables and three fundamental dimensions, Buckingham's π theorem tells us that we can reduce the system to $7 - 3 = 4$ independent dimensionless groups, known as π terms. The goal of the following step is to construct these four Π terms using a suitable set of repeating variables that include all base dimensions and are independent of the dependent variable H.

- Step 3: Dimensional Analysis Setup

  We choose the repeating variables as: D (pile diameter), E (Young's modulus of pile), γ (unit weight of soil). These span the fundamental dimensions of mass $[M]$, length $[L]$, and time $[T]$.

  – Π Term 1: Lateral Load Capacity

  $$\Pi_1 = \frac{H}{\gamma L^3} \tag{7}$$

  Explanation: γL^3 has the same dimensions as force, $[MLT^{-2}]$, so this ratio is dimensionless. This term expresses the normalized lateral capacity of the pile. It should be noted that in [LHB10], a different choice for Π_1 is considered $\Pi_1 = \frac{H}{\gamma L D^2}$

  – Π Term 2: Slenderness Ratio

  $$\Pi_2 = \frac{L}{D} \tag{8}$$

  Explanation: A geometric ratio comparing pile length to diameter.

  – Π Term 3: Relative Pile Stiffness

  $$\Pi_3 = \frac{EI}{\gamma L^5} \tag{9}$$

  Explanation: EI has units of flexural stiffness $[ML^3T^{-2}]$, and γL^5 also has units $[ML^3T^{-2}]$. So their ratio is dimensionless.

  – Π Term 4: Soil Friction Angle

  $$\Pi_4 = \phi \tag{10}$$

  Explanation: The internal friction angle ϕ is already dimensionless.

  – Resulting Functional Relationship

  $$\frac{H}{\gamma L^3} = f\left(\frac{L}{D}, \frac{EI}{\gamma L^5}, \phi\right) \tag{11}$$

The dimensionless groups derived in Eq.11 guide the parametric analysis of the system's mechanical behavior. Consequently, the experimental plan should aim to vary each dimensionless group independently. For instance, varying L and D independently is unnecessary if the experiments are conducted at the same $\frac{L}{D}$ ratio, as their individual effects cannot be decoupled under such conditions.

If the physical model (index m) shares the same dimensionless groups expressed in the function f as the prototype (index p), the lateral capacity obtained for the physical model in the laboratory can be scaled to the prototype scale using the following relationship:

$$\frac{H_p}{\gamma_p L_p^3} = \frac{H_m}{\gamma_m L_m^3} \tag{12}$$

or,

$$H_p = \frac{H_m}{\gamma_m L_m^3} \gamma_p L_p^3 \tag{13}$$

2.3 From dimensionless groups to scaling factors

Once a set of dimensionless groups is established, whether through variable-based or equation-based dimensional analysis, the next step in physical modeling is to determine the appropriate scale factors. These are ratios between model and prototype quantities (e.g., length, time, stress) that ensure similarity is preserved. They are usually reported in widely used tables for scaling laws [GGS$^+$07]. For example, length λ_l, time λ_t and stress λ_σ scale factors can be defined as:

$$\lambda_l = \frac{l_p}{l_m} \quad \lambda_t = \frac{t_p}{t_m} \quad \lambda_\sigma = \frac{\sigma_p}{\sigma_m} \tag{14}$$

where the subscripts p and m refer to the variables in the prototype and in the physical model respectively. By matching the dimensionless groups between model and prototype, we derive relationships between scale factors, which guide how experiments must be designed or interpreted.

The number of independent scale factors you can define for a given problem is equal to the number of fundamental dimensions involved. If k is the number of fundamental dimensions (e.g., $[M], [L], [T]$) involved in the problem, one can define at most k independent scale factors. All other scaling are dependent and must be consistent with the dimensionless group requirements.

For example, for scale factors:

- $\lambda_l = \dfrac{l_p}{l_m} = N$ for length, with the physical model picturing a prototype N times larger.
- $\lambda_g = \dfrac{g_p}{g_m} = 1$ for gravity, for a test in the laboratory (not a centrifuge test).
- $\lambda_\rho = \dfrac{\rho_p}{\rho_m} = 1$ for the density of the sand, if the same sand with the same density is used in the model as in the prototype.

Therefore, as the vertical stress due to overburden pressure in the soils are determined by: ($\sigma_v = \rho g z$), the stresses scale as:

$$\lambda_\sigma = \lambda_\rho \lambda_g \lambda_l = N \tag{15}$$

As $\lambda_\sigma = \dfrac{\sigma_p}{\sigma_m}$, this means that the stresses in the prototype are N times larger than in the physical model.

3 Single gravity and centrifuge modeling in geomechanics

Centrifuge modeling is an experimental method widely applied in geotechnical engineering, where experiments are carried out in a specially designed container that spins around a vertical axis (see fig.3 for an example of a beam centrifuge) at high rotational speed. The rotation generates a centrifugal acceleration that simulates increased gravitational forces, scaled according to the rotation speed.

The centrifugal acceleration a_c and the associated centrifugal force F_c experienced by the geotechnical physical model of mass m_p in the rotating physical model is given by:

$$a_c = \omega^2 \cdot R \quad \text{and} \quad F_c = m_p \cdot a_c \tag{16}$$

Where F_c is the centrifugal force, ω is the angular velocity (in radians per second) and R is the distance from the center of rotation to the model (in meters). there are many beam geocentrifuge facilities around the globe with R ranging from 0,75 meters to 9 meters [ISS25].

Eq.16 can also be expressed in terms of gravitational acceleration g to obtain the gravity level (N_g-g):

$$\frac{a_c}{g} = \frac{\omega^2 \cdot r}{g} = N_g \tag{17}$$

So, the model experiences N_g times Earth's gravity, where N_g is the gravity scaling factor (e.g., 50g, 100g) and $g \approx 9.81$ m/s^2

The fundamental goal is to recreate the stress conditions of a real-world (prototype) system within a reduced-scale model, ensuring that the soil responds in a similar manner. This method addresses one of the core challenges in physical modeling in geomechanics: replicating stress-dependent soil behavior, which significantly improves the credibility of experimental findings. Nonetheless, the technique is not without constraints: the limited dimensions of the centrifuge container can pose challenges for

applying loads and installing precise monitoring equipment. Moreover, parasitic (unwanted) vibrations of a geotechnical centrifuge hinder the use of this setup to study some cyclic and dynamic foundation-soil interaction problems [BDN+21].

In order to illustrate how artificial gravity generated by the centrifugal force affects the stresses, let us consider the same scaling factors as in section 2.3. For this physical model, we consider that the scale factors for length and density are unchanged, while the gravity is changed, such that the scale factors are:

$$\lambda_l = \frac{l_p}{l_m} = N \text{ , } \lambda_\rho = \frac{\rho_p}{\rho_m} = 1 \text{ and } \lambda_g = \frac{g_p}{g_m} = \frac{1}{N_g}.$$

This is such that the stresses scale as:

$$\lambda_\sigma = \lambda_\rho \lambda_g \lambda_l = \frac{N}{N_g} \tag{18}$$

Thus, if the geometric scaling factor N is the same as the gravity scaling factor N_g (which is usually the case) then $\lambda_\sigma = 1$, which means that the stresses in the physical model are the same as in the prototype.

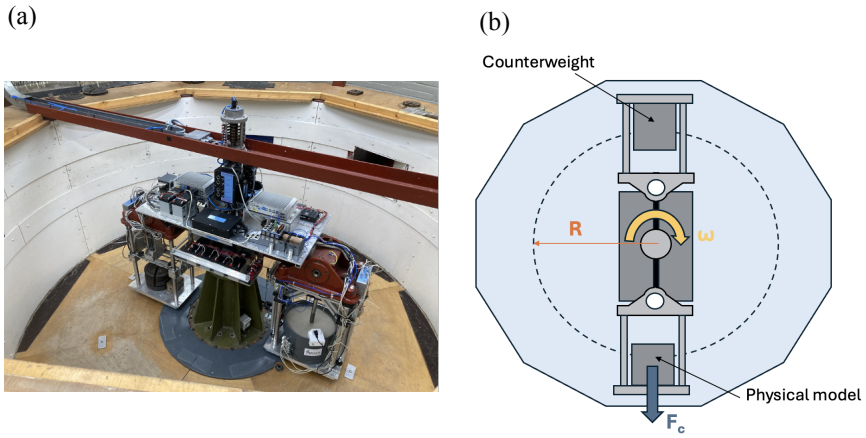

Figure 3: (a) Picture of the geo-centrifuge experimental setup at TUDelft (Netherlands) (b) Schematic top view of the centrifuge in rotation.

4 Limits and Challenges of physical models

Partial similarity occurs when only some aspects of the prototype behavior are correctly reproduced in the model, typically due to practical limitations in replicating all governing parameters or conflicts appearing in-between the scaling of different physical processes [SHB+63]. Partial similarity is common in many lab-scale geotechnical

tests (i.e., 1g experiments) or when some physical effects happening at the prototype scale cannot be reproduced in the same conditions for the physical model. In this case, the physical model can still provide qualitative insights, help identify mechanisms, or compare different design alternatives, but does not provide exact field performance when applying the scaling laws.

For 1g tests, some solutions can be applied to overcome the limitation of the stress-state conditions differing from the prototype. In the physical model at 1g, the lower confining stresses typically applied result in elevated friction angles for the soil but reduced shear stiffnesses when compared to prototype conditions. To ensure that the peak friction angle observed in the laboratory corresponds to that of a full-scale scenario, samples are commonly prepared at lower relative densities [Bak21]. While this adjustment is relatively straightforward, reproducing representative stiffness characteristics remains significantly more complex due to their sensitivity to stress level, but also strain range. A methodology to address this issue for the particular case of laterally loaded piles is developed in [LHB10] by considering momentum balance equations of the system.

When dealing with Thermo-Hydro-Chemo-Mechanical (THCM) couplings in geotechnical centrifuge modeling or at 1g lab-modeling, achieving complete scaling (full similarity) across all processes is extremely challenging. Each physical field (thermal, hydraulic, chemical, mechanical) has its own characteristic scales and dependencies, and not all of them scale naturally with gravity. This creates conflicts and trade-offs in scaling laws. This is the case in particular for the scaling of the time for the physical model.

In scaled modeling, mechanical forces are scaled, which imposes constraints on stress, strain, and implicitly time (when the process is not static). Stresses have a dimension that can expressed in $[ML^{-1}T^{-2}]$. Therefore, the scale factor for time for the mechanical process $\lambda_{t,m}$ is:

$$\lambda_{t,m} = \sqrt{\frac{\lambda_m}{\lambda_l \cdot \lambda_\sigma}} \tag{19}$$

where λ_m is the scaling factor for the mass. This yields a scaling factor for the time $\lambda_{t,m}$ of $\sqrt{N}$ for 1-g physical models and N for centrifuge tests.

Hydraulic, thermal, and chemical processes are typically governed by diffusion equations of the form:

$$\frac{\partial \phi}{\partial t} = D\nabla^2\phi \tag{20}$$

where ϕ is a field variable (e.g., temperature, pore pressure or concentration), and D is the diffusivity (thermal α_T, hydraulic c_v as in section 2.1, or chemical D_c).

These diffusion processes are controlled by the dimensionless number $\frac{T \cdot D}{H^2}$, as shown in Eq.6, that can be expressed in terms of scaling factor $\lambda_{t,diff}$:

$$\lambda_{t,diff} = \frac{\lambda_l^2}{\lambda_D} \tag{21}$$

where λ_D is the scaling factor for the diffusivity. If the physical model is scaled with a factor N, the scaling factor for the time can be expressed as $\lambda_{t,diff} = \frac{N^2}{\lambda_D}$, which means that, to obtain the same time scaling as for the mechanical process ($\lambda_{t,m} = \lambda_{t,diff}$), we need to have $\lambda_D = N^{3/2}$ at 1-g or $\lambda_D = N$ in the centrifuge.

Since diffusive processes and mechanical processes each have their own governing time scales, they do not naturally scale together unless the relevant diffusivities are adjusted. This requires the use of analog materials with modified properties: thermal conductivity and heat capacity must be altered to scale the thermal diffusivity α_T, hydraulic conductivity must be adjusted to correctly scale the coefficient of consolidation c_v, and chemical diffusivity should be modified to control the effective diffusion coefficient D_c. Without such adjustments, diffusion processes will occur too rapidly in the model, leading to effects such as rapid temperature equalization, fast pore pressure dissipation, and unrealistically fast contaminant transport. These discrepancies result in only partial similarity, meaning the model no longer accurately replicates the time-dependent behavior of the prototype system.

For hydro-mechanical couplings, the coefficient of consolidation is:

$$c_v = \frac{k}{m_v \cdot \gamma} \tag{22}$$

where m_v is the coefficient of volume compressibility, γ is the unit weight of the fluid in the pores and k is the hydraulic conductivity. The latter can be expressed as $k = \frac{\kappa \cdot \gamma}{\mu}$ (with κ the permeability of the medium and μ the viscosity of the fluid). Therefore, many authors have scaled the hydraulic process by using a liquid with a greater viscosity than water allowing to change λ_D to achieve full similarity [AM15].

Numerous centrifuge experiments have investigated energy piles with thermo-mechanical or thermo-hydro-mechanical couplings [LMNS20]. In those studies, the thermal diffusivity was not scaled resulting in a larger thermal influence zone around the heat source and partial similarity.

Sandbox experiments have also been developed to investigate the sequestration of CO_2 in geological layers and in particular fluids displacement physics, including structural trapping, residual trapping, and convective mixing and dissolution [KNF24]. It is also used to validate numerical model as their results for underground CO_2 storage are almost never quantified with respect to direct observations that provide a ground truth (see fig.4) [SSHE$^+$24]. In essence, such sandbox experiments allow to observe subsurface CO_2 dynamics in a simplified well-controlled, scaled-down version of reality with partial similarity. It still allows to learn a lot about certain

interactions if the limitations of scaling are well characterized and the experimental campaign is coupled to numerical models, as the scale, complex geology, dynamic pressures, and full range of chemical and biological processes cannot be entirely replicated or accurately predicted from the confined environment [KNF24].

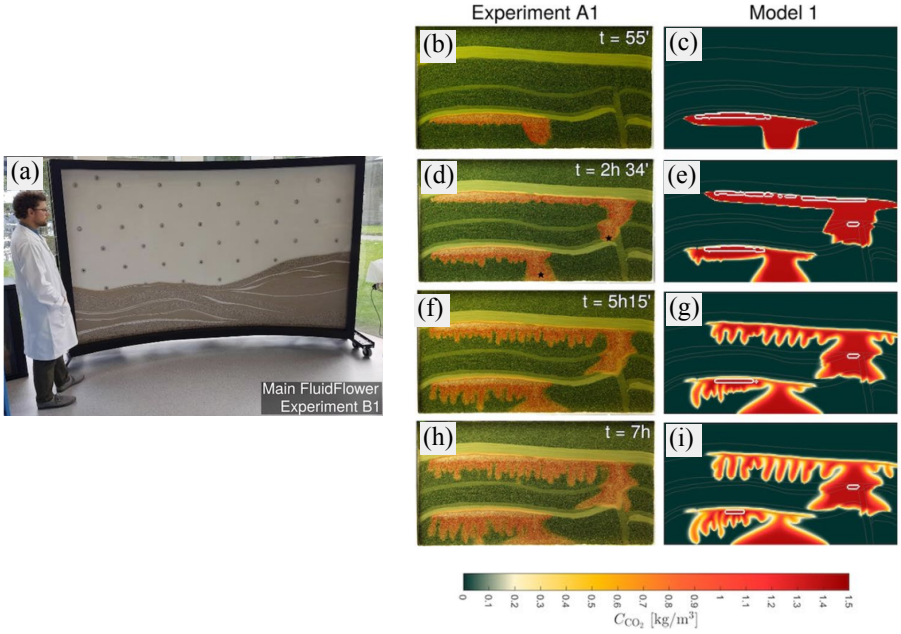

Figure 4: (a) Overview of the sandbox experimental setup FluidFlower developed at the university of Bergen, (b-i) Comparison between an experiment of CO_2 injection (left column) and simulation results (right column). Color map in simulation plots refers to CO_2 concentration in water, according to color bar. Figure adapted from [SSHE$^+$24], under CC BY 4.0..

5 Conclusions and Perspectives

This chapter has underscored the pivotal role of physical modeling in addressing geomechanical challenges of the energy transition. By exploring fundamental scaling laws and dimensional analysis, it highlighted the necessity and the challenges of maintaining similarity between model and prototype systems, particularly under multiphysics conditions. Centrifuge experiments emerged as essential tools, when possible to use, to replicate stress environments, while acknowledging practical constraints like partial similarity and THMC scaling conflicts. Informed scaling, grounded in rigorous dimensional reasoning and tailored to project specific phenomena is indispensable for producing reliable, transferable insights.

In terms of future perspective, hybrid approaches combining physical testing, advanced numerical modeling, and data-driven techniques (e.g., digital twins and sensitivity analysis) are expected to enhance fidelity and predictive power. Greater emphasis on uncertainty quantification and reproducibility will further solidify the role of informed physical modeling for the understanding and development of energy infrastructures.

References

[AM15] Orestis Adamidis and Gopal Santana Phani Madabhushi. Use of viscous pore fluids in dynamic centrifuge modelling. *International Journal of Physical Modelling in Geotechnics*, 15(3):141–149, 2015.

[AWS14] Thorsten Agemar, Josef Weber, and Rüdiger Schulz. Deep geothermal energy production in germany. *Energies*, 7(7):4397–4416, 2014.

[Bak21] Hussein Bakri. *Étude expérimentale et numérique de l'interaction sol-structure sous chargement cyclique dynamique: application aux fondations mono-pieux des éoliennes offshore*. Thèse de doctorat, Université Paris-Est (ENPC / Navier), Paris, France, December 2021.

[BAP+24] Ahmed Bashir, Muhammad Ali, Shirish Patil, Murtada Saleh Aljawad, Mohamed Mahmoud, Dhafer Al-Shehri, Hussein Hoteit, and Muhammad Shahzad Kamal. Comprehensive review of co2 geological storage: Exploring principles, mechanisms, and prospects. *Earth-Science Reviews*, 249:104672, 2024.

[BDN+21] Subhamoy Bhattacharya, Hasan Emre Demirci, George Nikitas, Ganga Kasi V. Prakhya, Domenico Lombardi, Nicholas A. Alexander, M. Aleem, Sadra Amani, and George Mylonakis. Chapter 11 - physical modeling of interaction problems in geotechnical engineering. In Pijush Samui, Sunita Kumari, Vladimir Makarov, and Pradeep Kurup, editors, *Modeling in Geotechnical Engineering*, pages 205–256. Academic Press, 2021.

[BM19] Koenraad F Beckers and Kevin McCabe. Geophires v2. 0: updated geothermal techno-economic simulation tool. *Geothermal Energy*, 7(1):5, 2019.

[Buc14] Edgar Buckingham. On physically similar systems; illustrations of the use of dimensional equations. *Physical review*, 4(4):345, 1914.

[Buc31] P. B. Bucky. *The use of models for the study of mining problems*, volume 425 of *Technical Publication*. American Institute of Mining and Metallurgical Engineers, New York, 1931.

[GGS+07] Jacques Garnier, Christophe Gaudin, Sarah M Springman, PJ Culligan, D Goodings, D Konig, B Kutter, R Phillips, MF Randolph, and Luc

Thorel. Catalogue of scaling laws and similitude questions in geotechnical centrifuge modelling. *International Journal of Physical Modelling in Geotechnics*, 7(3):01–23, 2007.

[Goo99] Richard E Goodman. Karl terzaghi: The engineer as artist. American Society of Civil Engineers, 1999.

[Int23] Intergovernmental Panel on Climate Change (IPCC). Sections. In H.Lee and J.Romero, editors, *Climate Change 2023: Synthesis Report. Contribution of Working Groups I, II and III to the Sixth Assessment Report of the Intergovernmental Panel on Climate Change*, pages 35–115. IPCC, Geneva, Switzerland, 2023.

[IPC23] *Climate Change 2022 - Mitigation of Climate Change: Working Group III Contribution to the Sixth Assessment Report of the Intergovernmental Panel on Climate Change*. Cambridge University Press, 2023.

[ISS25] ISSMGE TC104. Facilities. `https://tc104-issmge.com/facilities/`, 2025. [Online; accessed July 21, 2025].

[ITN05] S Iai, T Tobita, and T Nakahara. Generalised scaling relations for dynamic centrifuge tests. *Geotechnique*, 55(5):355–362, 2005.

[Jia21] Zhiyu Jiang. Installation of offshore wind turbines: A technical review. *Renewable and Sustainable Energy Reviews*, 139:110576, 2021.

[KNF24] Anthony R Kovscek, Jan Martin Nordbotten, and MA Fernø. Scaling up fluidflower results for carbon dioxide storage in geological media. *Transport in Porous Media*, 151(5):975–1002, 2024.

[LHB10] Christian LeBlanc, Guy T Houlsby, and Byron W Byrne. Response of stiff piles in sand to long-term cyclic lateral loading. *Géotechnique*, 60(2):79–90, 2010.

[LMNS20] Fleur Loveridge, John S. McCartney, Guillermo A. Narsilio, and Marcelo Sanchez. Energy geostructures: A review of analysis approaches, in situ testing and model scale experiments. *Geomechanics for Energy and the Environment*, 22:100173, 2020.

[MB14] Anders Myhr, Catho Bjerkseter, Anders Ågotnes, and Tor A. Nygaard. Levelised cost of energy for offshore floating wind turbines in a life cycle perspective. *Renewable Energy*, 66:714–728, 2014.

[PF36] G. Y. Pokrovsky and I. S. Fedorov. Studies of soil pressures and soil deformations by means of a centrifuge. In *Proceedings of the 1st International Conference on Soil Mechanics and Foundation Engineering*, volume 1, 1936.

[Ram18] M. V. Ramana. Technical and social problems of nuclear waste. *WIREs Energy and Environment*, 7(4):e289, 2018.

[SB21] Kingsley Sunday and Feargal Brennan. A review of offshore wind monopiles structural design achievements and challenges. *Ocean Engineering*, 235:109409, 2021.

[Sch80] Andrew Noel Schofield. Cambridge geotechnical centrifuge operations. *Geotechnique*, 30(3):227–268, 1980.

[SHB+63] D.B. Spalding, H.C. Hottel, S.L. Bragg, A.H. Lefebvre, D.G. Shepherd, and A.C. Scurlock. The art of partial modeling. *Symposium (International) on Combustion*, 9(1):833–843, 1963.

[SR21] Juan Carlos Santamarina and Rached Rached. Energy geoscience and engineering. In Marco Barla, Alice Di Donna, and Donatella Sterpi, editors, *Challenges and Innovations in Geomechanics*, pages 75–97, Cham, 2021. Springer International Publishing.

[SSHE+24] Lluís Saló-Salgado, Malin Haugen, Kristoffer Eikehaug, Martin Fernø, Jan M Nordbotten, and Ruben Juanes. Direct comparison of numerical simulations and experiments of co 2 injection and migration in geologic media: Value of local data and forecasting capability. *Transport in Porous Media*, 151(5):1199–1240, 2024.

[VHCV12] Harry Vidas, Bob Hugman, Ananth Chikkatur, and Boddu Venkatesh. Analysis of the costs and benefits of co2 sequestration on the us outer continental shelf. *OCS Study BOEM*, 100, 2012.

[Woo17] David Muir Wood. *Geotechnical modelling*. CRC press, 2017.

Microscale geomechanics

Martin Lesueur

Delft University of Technology

Microscale geomechanics investigates the grain- and pore-scale processes that govern the bulk behavior of geomaterials, with direct implications for the performance, reliability, and long-term safety of renewable energy technologies. This book chapter provides a comprehensive overview of the foundational concepts, experimental and numerical methods used to characterize and model geomechanics at the microscale. The first section introduces the scale at play and relevant parameters of the microstructure that influence bulk material behaviour. The second section presents the experimental characterisation of microscale geomechanics, focusing primarily on microscale imaging which is required for the numerical flow and mechanical simulations, described in the third section. Section four explains the fundamental principles of upscaling which is used to homogenise effective properties from the microscale. The last section presents some perspective of the current challenges in the discipline.

1 The importance of the microscale for geomechanics

In geomechanics, the microscale refers to the characteristic length scale at which the internal microstructure of a geomaterial can be directly observed, discretized, and quantified. This is the scale at which the material ceases to appear as a homogeneous continuum and instead reveals its heterogeneous structure. Elements that can be observed include solid grains, voids, cement bonds, biofilms, microcracks and fluid-filled pores. For most soils and rocks, the microscale corresponds to dimensions on the order of a few micrometres to hundreds of micrometres — typically comparable to individual grain sizes. You can refer to those scales in the well-known Udden–Wentworth grain size scale [Wen22].

At this scale, several parameters can influence the material's bulk behavior:

- Grain size distribution and grains morphology
- Pore network geometry
- Grain contacts and fabric

- Mineral composition
- Cementation or biofilm bonding and reactivity
- Presence of flaws or defects
- Multi-phase fluid distribution within the pore space

Understanding geomechanical behavior from a microscale perspective is essential because macroscopic properties and responses – thermal, mechanical, hydraulic and chemical – can emerge from microscale interactions often in the form of structure-property relationships. For instance, stress transmission in granular assemblies occurs through discrete force chains formed at grain contacts; permeability is controlled by the connectivity and constriction of the pore network; and chemical reactivity is influenced by interfacial area and surface properties at the grain scale.

It is important to acknowledge that different physical phenomena manifest at different spatial and temporal scales, and each must be studied at the scale most relevant to its governing mechanisms. Many mechanisms of porous flow for example come from the microscale. While pore pressure diffusion expressed by Darcy's law is solved for at the reservoir scale, its main parameter permeability is directly controlled by tortuosity that depends on the pore network geometry, see Fig. 1. And permeability can only be directly computed via upscaling from explicitly resolving the flow at the microscale – using Navier-Stokes equations for example. For multiphase flow, capillary trapping – which prevents flow through – is directly controlled by pore throat geometry. As the only scale where the pore-grain interface appears, the microscale dictates most chemical processes that often occur at reactive interfaces and depend on specific surface area. Chain forces and grain rearrangement are the reasons that most geomechanics constitutive laws emerge from the microscale, and they can be directly interpreted from DEM simulations that consider grains arrangement and grain-to-grain forces, see Fig. 1. For thermal processes, while thermal conductivity is influenced by the heterogeneous mineral composition at the microscale, thermal diffusion has a larger characteristic length scale like pressure diffusion.

Despite the clear significance of microscale processes in shaping macroscopic responses, two major challenges arise. The first is the experimental difficulty of observing and quantifying microscale features and their evolution under realistic pressure, temperature, and chemical conditions. The second the mathematical and physical challenge of modeling these microscale interactions with sufficient fidelity to capture the essential physics, while managing computational cost and complexity. In this context, the concept of upscaling provides a crucial framework as it connects detailed microscale information to the macroscopic properties required in engineering-scale models, allowing us to bridge length scales and transfer insights from physical or virtual experiments into predictive continuum formulations.

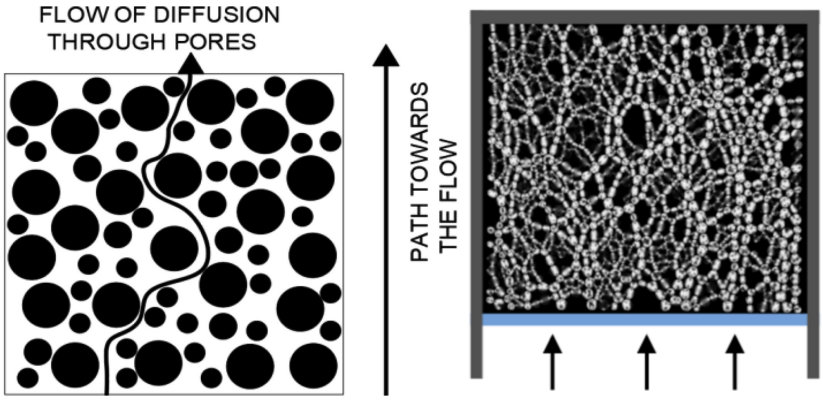

Figure 1: (left) Illustration of tortuosity in a porous medium [dSdRCVM22]. (right) Force chains image in uniaxial stress state [Dan17].

2 Experimental characterisation

Since many rock properties are inherently controlled by microscale features, capturing and quantifying those features of the microstructure represents a main challenge of microscale geomechanics. Some average properties can already be obtained through routine core characterisation in the lab. Porosity is the most famous one, which can be measured by a porosimeter using injection of either mercury or helium. For more detailed measurements, we have to resort to direct imaging techniques.

2.1 Microscale imaging

Direct imaging of geomaterials at the microscale provides a means to visualize, analyze, and quantify the internal microstructure of a material. Compared to most mechanical or flow experiments, imaging is typically considered a non-destructive technique, which is particularly advantageous when working with rare or valuable geomaterials, such as those obtained from deep-drilled cores or unique geological formations. However, imaging is often semi-destructive in practice, as most methods require the sample to be cut, cored, or polished to specific dimensions suitable for the imaging apparatus.

Micro-computed tomography (μCT) uses X-rays to produce high-resolution three-dimensional reconstructions of a material's internal structure. During scanning, the sample is rotated incrementally between an X-ray source and a detector, producing a series of radiographic projections at different angles. These 2D images are then reconstructed using algorithms to yield a 3D volumetric dataset, where each voxel represents the local X-ray attenuation, which correlates to material density and composition. In geomechanics, μCT is widely used to examine pore architecture, grain arrangement, microcracks, and cementation features, allowing for direct quantifica-

tion of properties such as porosity, pore-size distribution, tortuosity, and coordination number. µCT systems offer a resolution already higher than regular CT (typically 1–10 µm).

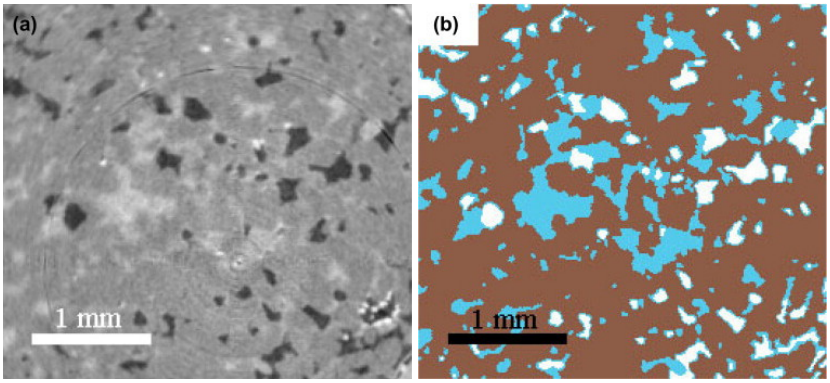

Figure 2: µCT images of supercritical CO2 clusters after waterflooding with CO2 saturated brine. (a) A raw grey-scale image (b) The same slice with phases segmented. Supercritical CO2 is white, brine light blue and rock is brown. [BBD+13].

Precise microstructure measurements on µCT-scans require to distinguish pore space from the solid matrix with a clear definition of the pore-grain interface. The process used named segmentation consist into converting the grayscale X-ray attenuation data into a binary or multi-phase image in which each voxel is assigned to a specific material phase (e.g., pore, grain, cement, or fluid), see Fig. 2. For many geomaterials, this step is non-trivial due to the partial volume effect, low contrast between phases, and noise inherent to imaging. Simple thresholding methods may suffice for well-separated attenuation histograms, such as in dry sandstones, but are often inadequate for finer-grained or chemically heterogeneous rocks like carbonates or shales. In such cases, advanced segmentation approaches such as watershed algorithms are employed to better capture complex interfaces. More recently, the use of machine learning has become the state-of-the-art with numerous studies [WBAM21] addressing the limitations of resolution, contrast, and manual thresholding by training models to recognize complex features and material boundaries that are otherwise difficult to distinguish using traditional methods.

For higher-resolution studies – especially for fine-grained rocks like shales – synchrotron-based µCT offers a significant advantage, providing sub-micron resolution and improved contrast due to the intense, collimated, and tunable X-ray beam produced by particle accelerators. Synchrotron facilities also enable fast time-lapse imaging under in-situ conditions (e.g., mechanical loading or fluid flow), making them a powerful tool for observing dynamic processes such as fracture propagation, pore collapse, or fluid invasion in real time.

High resolution can also be obtained by Scanning Electron Microscopy (SEM) which

is restricted however to two-dimensional images of the surface microstructure of geomaterials. It operates by scanning a focused beam of electrons across the sample surface and detecting secondary or backscattered electrons emitted from the interaction between the beam and the material. SEM provides detailed information on grain morphology, surface roughness, microcracks, pore textures, and cementation features, often at sub-micron to nanometre resolution — far beyond that of conventional optical microscopy. When combined with energy-dispersive X-ray spectroscopy (EDS), SEM can also reveal elemental composition and mineralogical variations, see Fig. 3, which are critical for understanding chemical heterogeneity and reactivity. To overcome the two-dimensional limitation of SEM, recent studies have combined SEM and µCT data using machine learning techniques, enabling the propagation of high-resolution SEM information throughout the three-dimensional digital rock volume obtained from µCT scans.

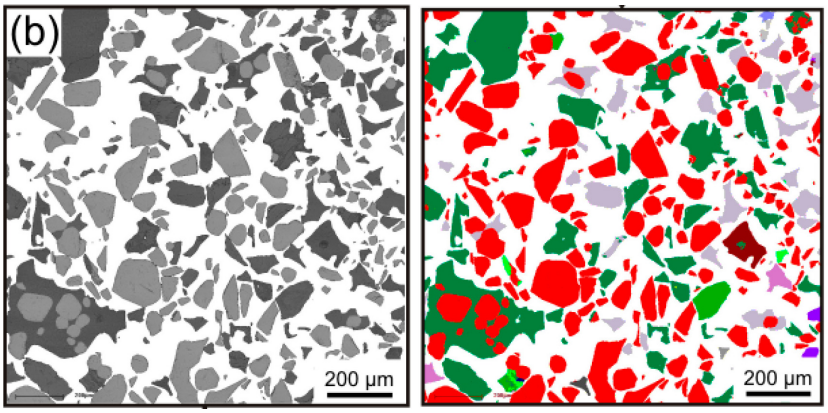

Figure 3: SEM Automated Mineralogy measurement methods on a backscattered electron image (left) and the classified EDS image (right) [SSG20].

2.2 Microscale geomechanics experiments

Beyond imaging, laboratory experiments at the microscale offer direct insights into the physical processes that govern geomechanical behavior, enabling controlled observation and measurement of deformation, flow, and interfacial phenomena at the grain and pore scale.

Microfluidics is a powerful tool to study pore-scale flow mechanisms under well-controlled conditions using transparent micromodels that replicate the geometry of porous media, see Fig. 4. These micromodels, typically fabricated in glass or polymer, allow real-time visualization of single-phase and multiphase fluid displacement, capillary trapping, viscous fingering, and wettability effects. Fluids can be injected at precise rates while imaging systems capture the evolution of the fluid–solid interface, allowing quantification of parameters such as residual saturation, displacement effi-

ciency, and pore-scale contact angle hysteresis. Microfluidics is particularly useful for studying dynamic processes relevant to CO2 and hydrogen injection, where interfacial tension and wettability strongly influence flow behavior.

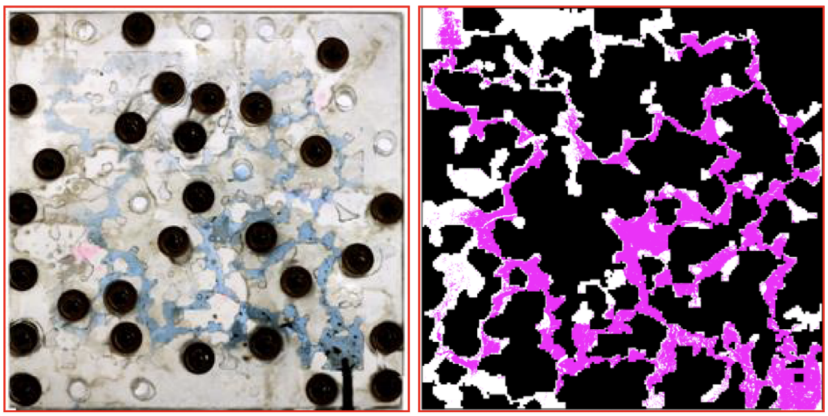

Figure 4: Experiment on a microfluidic chip of miscible flow (left) and segmented image (right) [MSO21].

Micromechanical testing methods aim to characterize the mechanical response of geomaterials at small scales, providing data on local stiffness, strength, fracture behavior, and grain-scale interactions. Techniques such as nanoindentation in Fig. 5 enable measurement of elastic modulus and hardness at the scale of individual grains or cement phases, revealing mechanical contrasts between mineral constituents. In addition, single grain experiments of compression and crushing allow investigation of grain strength, contact mechanics, and intergranular friction. These tests are critical for understanding the mechanics of granular assemblies and validating contact laws used in numerical models like the Discrete Element Method (DEM). In syntethic setups, force chains and load transfer mechanisms can be observed by compressing or shearing 2D granular packings while tracking individual grain behavior through digital image correlation techniques.

3 Numerical simulation of microscale geomechanics

As much as they are invaluable, microscale experiments are rare. Based on specialised equipments as described in the previous section, tests on real microstructures are therefore limited and replicating in situ conditions of pressure and temperature is particularly challenging. For these reasons, numerical simulations have become a powerful tool to understand and model the physical behaviour of geomaterials from a microscale perspective.They allow for the reconstruction of realistic microstructures, often based on imaging data, and simulate physical processes under controlled conditions, that would even be occurring over geological timescales.

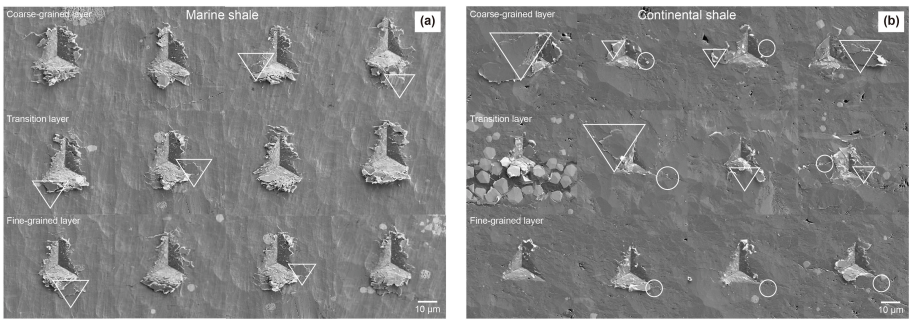

Figure 5: Microscopic indentation morphology of (a) Longmaxi marine shale and (b) Qingshankou continental shale (the ellipse region and the triangle region are the irregular cracks and protrusions caused by indentation, respectively) [GSC+24].

3.1 Domain decomposition and microstructure generation

Numerical simulations at the microscale begin with the definition of the computational domain. Different physical processes may only be applicable to different phases of the domain. For example, solid mechanics has to be solved in the grains while hydraulic flow applies to the pore space. After the domain has been restricted to the phase of interest, two general strategies are used to generate the microstructure; image-based and synthetic.

Image-based domains rely on stack of images – obtained most commmonly by μCT scanning. Segmentation is used to separate the pore from the grain space or even more mineral phases. Relying on pixelised images, the grid are therefore formed of voxels which can be used directly for lattice Boltzmann or Finite Volume solvers or converted one to one in structured meshes for Finite Element analysis. As a trade off for its simplicity, stair-stepping artifacts in those voxel-based representations appear which can be dealt with extra preprocessing such as unfitted boundary methods.

Synthetic microstructures offer a flexible alternative when imaging data are unavailable, incomplete, or difficult to process. These are typically generated through particle packing algorithms that simulate the deposition and rearrangement of individual grains. Such methods include isotropic compaction or gravity settling, often followed by consolidation steps where grains are allowed to rearrange under a prescribed confining stress until a mechanically stable and isotropic packing is achieved. These packings are designed to reproduce target properties such as grain size distribution, coordination number, and porosity, which must often be prescribed as an input measured in lab test or through imaging. Those computational domains often serve for inputs to Discrete Element Method (DEM) simulations. By adjusting packing density, grain shapes, or boundary conditions during generation, users can explore how structural features influence bulk mechanical behavior. Although synthetic packings lack the full complexity of real geomaterials obtained in image-based domains, they

offer the advantage of controlled generation, making them well suited for sensitivity analyses, parametric studies, or testing contact laws in DEM frameworks.

3.2 Numerical methods

Flow

Microscale fluid flow in porous geomaterials is governed by Navier-Stokes equations, where local velocity, pressure, and saturation fields evolve in response to the pore-scale structure. As the core exercise of Digital Rock Physics, several numerical approaches were developed to resolve these dynamics, each with its own trade-offs in terms of accuracy, computational cost, and geometric requirements.

While most classical, Finite Volume and Finite Element Methods (FVM/FEM) are the most accurate and versatile. They can be solved on pore geometries directly coming from μCT scan data, making them well suited for applications requiring high fidelity, including benchmark studies. These methods are particularly valued for their flexibility. They can accommodate complex geometries (structured or unstructured meshes in Fig. 7), a wide range of boundary conditions (Dirichlet, Neumann, periodic), and are easily extended to include coupled processes such as heat transport, solute transport, reactive flow, or mechanical deformation. However, this level of accuracy and generality comes at a computational cost. Solving systems of equations on high-quality meshes of large, high-resolution microstructures is resource intensive.

Lattice Boltzmann Method (LBM) exist as an alternative for modeling pore-scale fluid flow in complex, voxel-based geometries. Without explicit meshing and effective for both single and multiphase flow, it is a popular choice of simulator in Digital Rock Physics. You can see some multiphase flow results in Fig. 6.

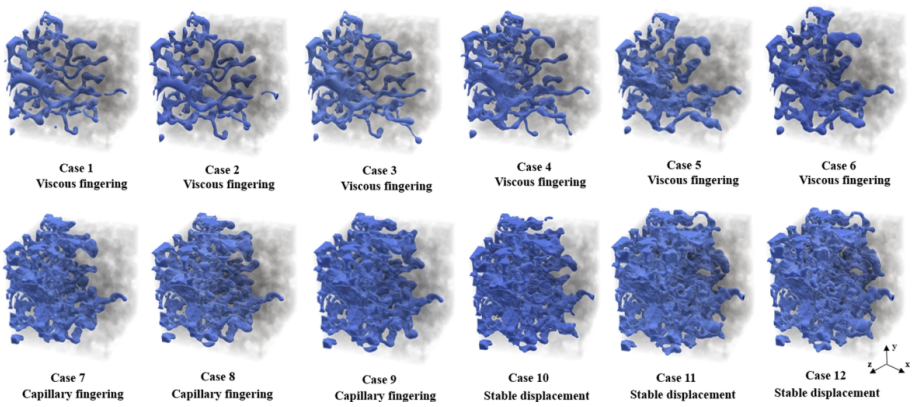

Figure 6: Two-phase flow behaviour in heterogeneous porous media (sandstone) solved with LBM, for different viscosity ratios and capillary numbers. [BHS19].

For faster analysis, Pore-Network Modeling (PNM) allows to simplify the geometry into an idealized graph of interconnected pores and throats, see Fig. 7, which can be extracted from imaging data or generated synthetically. While it sacrifices detailed spatial resolution, it offers significant computational efficiency and is widely used for upscaling flow properties such as relative permeability.

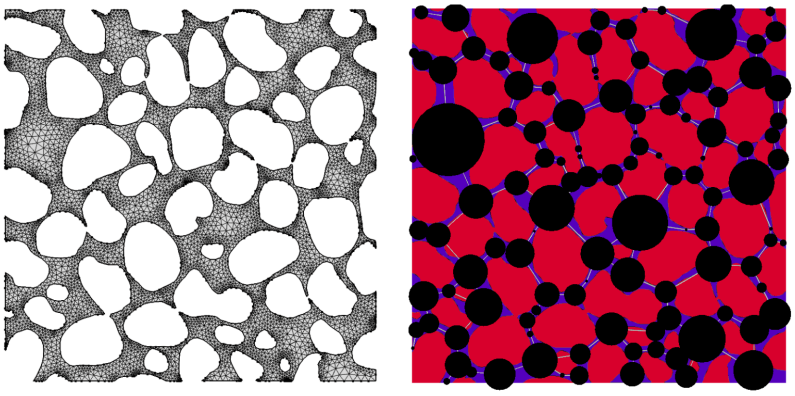

(a) FEM mesh (b) Equivalent PNM

Figure 7: Visualisation of a PNM of the pore space (right), in comparison to a standard unstructured FEM mesh (left) [GAH+16].

Mechanics

Mechanical behavior at the microscale is often dominated by interactions at grain contacts, making Discrete Element Method (DEM) particularly adequate. DEM explicitly models individual grains as rigid or deformable bodies and tracks their interactions through contact laws. These contacts can include normal and tangential stiffness, friction, cohesion. DEM is especially effective for simulating granular materials, where macroscopic behavior such as shear strength, strain localization, dilation, and compaction emerges from grain-scale rearrangement and force transmission. Outputs from DEM, such as force chains, contact networks, and kinematic fields, offer insight into the grain-scale origins of bulk constitutive behavior. DEM domains are typically initialized using particle packing algorithms, as discussed previously, and can incorporate particle shape effects via clumps or polyhedral elements. Recent advances using the Level-Set Method have enabled the development of LS-DEM [KAVA18], which allow for the explicit incorporation of image-based microstructures into DEM by accurately capturing complex grain shapes and interfaces extracted from imaging data.

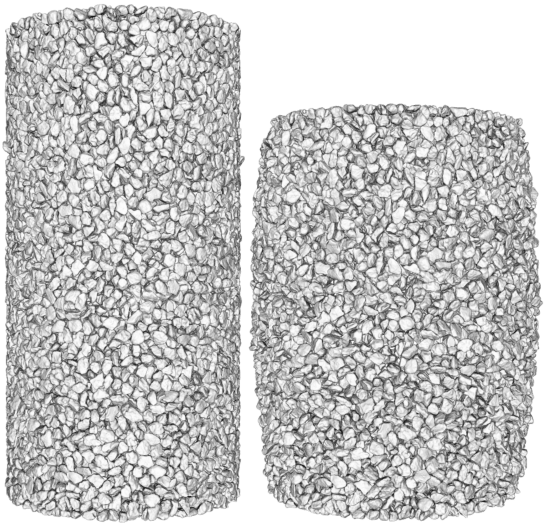

Figure 8: Results of triaxial compression of 22,351 grains sand specimen solved with LS-DEM. Before and after images [AK16].

3.3 Multiphysics couplings

Many of the critical geomechanical processes of renewable energy technologies involve interactions between multiple physical phenomena from the thermo-hydro-mechanical-chemical (THMC) phenomena that operate concurrently at the microscale. The different existing laws of physics are encompassed into the conservation of three main quantities; momentum, mass and energy in which the primary variables are respectively displacement, pressure and temperature. A multiphysics coupling is represented by a physical phenomenon interacting with another. One example is thermal advection where heat is transported by the motion of the fluid (in contrast with diffusion):

$$\frac{\partial T}{\partial t} + v \cdot \nabla \mathrm{T} = \alpha \nabla^2 T + \frac{q}{\rho c_p} \tag{1}$$

As observed, the multiphysics coupling is characterized by the presence of a physical variable other than the primary one in a governing physical law. At a more indirect level, multiphysics couplings can express themselves in the equations of state where physical properties such as material properties can depend on different physical variables. One example is fluid viscosity that is influenced by both temperature and pressure which in turns influences fluid flow, in the Navier-Stokes equations.

Because of domain decomposition, multiphysics coupling at the microscale often reduces to a transfer of variables across the pore–grain interface, where distinct physical processes interact. This interface plays a central role in fluid–structure interaction, governing how flow, deformation, and chemical reactions influence each other. For ex-

ample, fluid pressure acting on grains can induce mechanical deformation, leading to grain rearrangement and thus changes in pore geometry and connectivity. Conversely, grain displacements can alter local flow pathways, see both implemented in Fig. 9. In chemically active systems, reactive fluids may dissolve or precipitate material at the pore–grain interface, dynamically reshaping the microstructure. These feedbacks are essential to capture in simulations, as the microstructure alterations directly influence the structure-properties relationship.

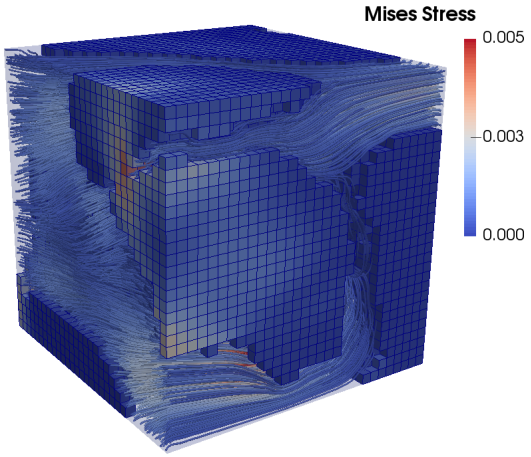

Figure 9: Fluid-structure interaction solved in FEM on a digital sandpack sample. Fluid velocity streamlines are generated in the pore space and concentration of stresses are visualised in the grains [LCVP17].

4 Upscaling principles

Separation of scales occurs when the macroscopic length scale is larger than the microscopic length scale by more than 3 orders of magnitude which the case when considering bulk behaviour of rocks with regards to their microstructure. To percolate information of the micro-scale to the macro-scale, we perform an upscaling using a homogenization method. The upscaled macroscopic response is called effective. Those multiscale methods are meant to couple the micro-scale and macro-scale models.

4.1 laws of mixtures

Different types of methods can be used to upscale. We can resort for example to simple empirical relationships which are the laws of mixtures. The first one from Voigt assumes that the effective medium is under a constant strain. For a two-phase

medium, the effective value of the property is equivalent to setting two springs in parallel, and is expressed as:

$$X_{eff} = \phi_1 X_1 + (1 - \phi_1) X_2 \tag{2}$$

Where ϕ_1 is the volume fraction of phase 1. For Reuss law, the assumption is constant force and similarly, the effective value of the property for a two-phase medium is equivalent to two springs in series and is expressed as

$$\frac{1}{X_{eff}} = \frac{\phi_1}{X_1} + \frac{1 - \phi_1}{X_2} \tag{3}$$

Those two formulas correspond respectively to kinematic or traction condition. Kinematic condition pushes the system to its maximal entropy and corresponds therefore to an upper bound of the effective property estimation, while the traction condition is oppositely the minimum. An illustrative example is plotted in Fig. 10. These simple methods quickly show limitations given the complexity of microscale. When trying to consider the exact microstructure, we need to resort instead to REV-based methods

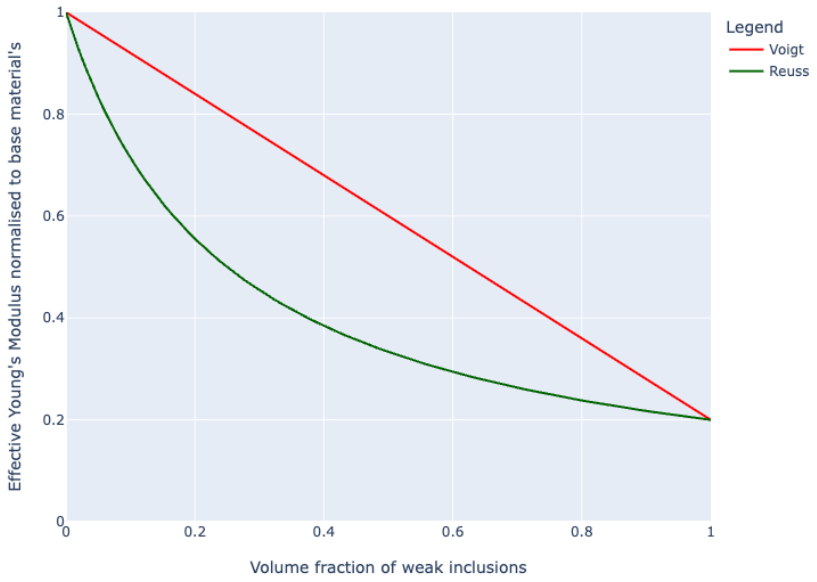

Figure 10: Laws of mixtures for Young's modulus of a porous medium with ratio between the base material and the weak inclusions of 0.2.

4.2 Representative Elementary Volume

While the micro-scale is heterogeneous whether in structure or in property distribution, upscaling can only be valid when the large scale is statistically homogeneous.

We define as such a Representative Elementary Volume (REV) above which size the effective property of interest does not fluctuate, see the cone of convergence in Fig. 11. The REV is defined for the property to upscale and the length scale considered. When focusing on upscaling the rock microstructure, the length scale is the average grain size. And studies show that the REV size for hydraulic conductivity of a rock is often larger than for its geometrical properties such as specific surface area or porosity [MBB12]. As we consider a natural material, non-periodic, the REV size needs to be sufficiently large enough to eliminate boundary effects.

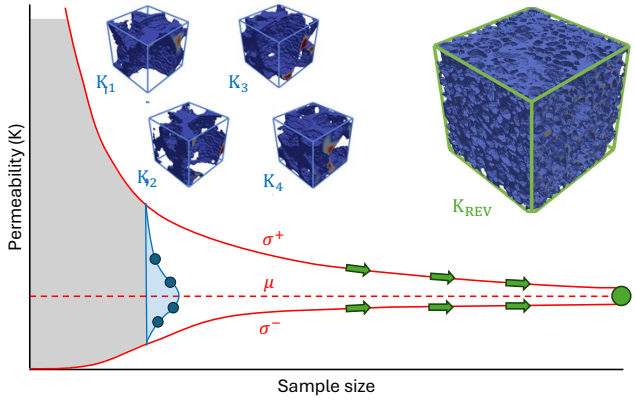

Figure 11: Schematic of a REV cone of convergence for permeability, illustrated with results on samples of different sizes [ZL24].

4.3 Averaging theorem

Effective quantities are obtained by averaging the microscopic fields. The average of the quantity X over the domain Ω is defined as:

$$\langle X \rangle = \overline{X} = \frac{1}{V_\Omega} \int_\Omega X dV \tag{4}$$

For the relationship macro to micro, we obtain:

$$X_M = \overline{X_m} \tag{5}$$

This relation is derived from the Hill-Mandel condition which expresses an irrefutable principle of thermodynamics. Hill's lemma states that the energy has to be conserved across scales. As a consequence, the macroscopic work has to be equal to the average of the microscopic work. From this condition, the averaging of other quantities can be derived similarly.

At the microscopic scale, any quantity can be expressed as a fluctuating field around the averaged value:

$$X_m = \overline{X_m} + \widetilde{X_m} \tag{6}$$

Where $\widetilde{X}$ is the fluctuation. Therefore we have:

$$X_M = \overline{\overline{X_m} + \widetilde{X_m}} = \overline{X_m} + \overline{\widetilde{X_m}} \tag{7}$$

This expression implies that the fluctuations need to average out on the domain for Eq. 6 to be valid. This is indeed the case when considering the domain size above REV, as per its definition. It showcases once more the need to consider a domain above the REV size for upscaling.

4.4 Upscaling

To obtain an effective property, we refer to the macroscopic constitutive law. The law is inverted to compute the property using the macroscopic fields values obtained from our simulation. Not all fields need to be averaged because the value of the boundary condition imposed on the system to close it corresponds directly to the macroscopic value of this variable. The other macroscopic variables are obtained by homogenizing the microscopic fields heterogeneously distributed in the simulation result.

To give an example, we go through the steps of upscaling the rock Young's modulus from its microstructure :

1. Set up a numerical experiment of uniaxial mechanical test with displacement-control of the digital rock sample above the REV size. The simulation solves for elasticity at the micro-scale. The macroscopic constitutive law for elasticity – Hooke's law – reads as:

$$\sigma = E \cdot \epsilon \tag{8}$$

2. The macroscopic axial strain can be directly calculated from the prescribed displacement at the boundary.
3. The macroscopic axial stress is averaged from the microscopic axial stress over the full sample.
4. The effective Young's modulus is calculated from Eq. 8.

In some instances, standalone upscaling like this is not possible. It is the case for complex systems where the macroscopic constitutive law cannot be directly defined. Instead of upscaling the effective property, the upscaled macroscopic variables are directly transferred. This allows to not make any constitutive assumption about the

material behaviour. It is also the case when the process to upscale is path- or history-dependent, such as irreversible processes like plasticity or. The micro-scale system requires therefore information from the macro-scale about the macroscopic state variables as the system evolves. Only then can the upscaled properties be fed to the macro-scale that can advance the simulation. The two scales are now coupled. When both scales are solved with finite element, these multiscale methods are called FE^2.

5 Perspective

Microscale geomechanics provides essential insights into the physical processes that govern reservoir-scale behaviour during subsurface operations. Developing predictive models grounded in these microscale mechanisms enhances our ability to assess the long-term feasibility, efficiency, and safety of emerging sustainable energy technologies.

The challenge lies for the most part in the inherent complexity of natural systems, arising not only by the heterogeneous microstructure but also from the multiphysics nature of subsurface processes, which are stimulated by the subsurface operations. One of the most persistent challenges is the incorporation of geochemical reactions, whether involving native fluids that become reactive under elevated thermal conditions–as in geothermal systems or radioactive waste storage–or injected fluids such as CO2 and H2, which can react with the rock matrix. Increasingly, engineered fluids with tailored chemical properties are also used for enhanced resource recovery, introducing further layers of reactive behaviour that must be captured at the microscale.

Additional complexity stems from the mechanical and dynamic nature of stimulation strategies. Unlike conventional reservoir operations, sustainable energy technologies can involve cyclic or transient loading, such as in seasonal hydrogen storage or the vibratory installation of offshore wind farm foundations. Understanding and modelling the grain-scale rearrangement is essential for these cases. Similarly, the initiation and propagation of fractures – whether mechanically induced before geothermal operations or thermally triggered by radioactive waste storage – is at the forefront of the micromodelling research tasks.

On the experimental front specifically imaging, several trends are progressing rapidly. The quest for higher resolution remains central and recent contributions increasingly focus on enhancing image quality and interpretability through advanced postprocessing techniques based on machine learning [WBAM21] to achieve super-resolution and multi-mineral classification/segmentation. Meanwhile, imaging under realistic conditions is gaining traction, with efforts to conduct in situ experiments within the imaging devices, producing valuable 4D datasets that capture the evolution of microstructure over time under mechanical, hydraulic, thermal, or chemical loading.

Looking ahead, bridging the gap between microscale observations and engineering-scale decisions remains an open frontier. Integrating detailed microstructural data into robust, scalable models will be key to designing resilient technologies. As the global

energy transition advances, microscale geomechanics will continue to play a foundational role in developing safe, efficient, and adaptive renewable energy technologies.

References

[AK16] Jose E. Andrade and Reid Kawamoto. LS-DEM: A New Paradigm for Discrete Element Simulations. In G. Viggiani, D. Salciarini, F. Silvestri, C. Tamagnini, and G. M. B. Viggiani, editors, *IV International Workshop on Modern Trends in Geomechanics*, Assisi, Italy, 2016. Abstract.

[BBD+13] Martin J. Blunt, Branko Bijeljic, Hu Dong, Oussama Gharbi, Stefan Iglauer, Peyman Mostaghimi, Adriana Paluszny, and Christopher Pentland. Pore-scale imaging and modelling. *Advances in Water Resources*, 51:197–216, January 2013.

[BHS19] Sahar Bakhshian, Seyyed A. Hosseini, and Nima Shokri. Pore-scale characteristics of multiphase flow in heterogeneous porous media using the lattice boltzmann method. *Scientific Reports*, 9(1), March 2019.

[Dan17] Karen E. Daniels. The role of force networks in granular materials. *EPJ Web of Conferences*, 140:01006, 2017.

[dSdRCVM22] Marly Terezinha Quadri Simões da Silva, Marianna do Rocio Cardoso, Caterina Maria Pabst Veronese, and Wellington Mazer. Tortuosity: A brief review. *Materials Today: Proceedings*, 58:1344–1349, 2022.

[GAH+16] Jeff Gostick, Mahmoudreza Aghighi, James Hinebaugh, Tom Tranter, Michael A. Hoeh, Harold Day, Brennan Spellacy, Mostafa H. Sharqawy, Aimy Bazylak, Alan Burns, Werner Lehnert, and Andreas Putz. Openpnm: A pore network modeling package. *Computing in Science & Engineering*, 18(4):60–74, July 2016.

[GSC+24] Ming-Zhe Gu, Mao Sheng, Shi-Zhong Cheng, Fan-Hao Gong, and Gen-Sheng Li. Influences of shale microstructure on mechanical properties and bedding fractures distribution. *Petroleum Science*, 21(3):1944–1954, June 2024.

[KAVA18] Reid Kawamoto, Edward Andò, Gioacchino Viggiani, and José E. Andrade. All you need is shape: Predicting shear banding in sand with ls-dem. *Journal of the Mechanics and Physics of Solids*, 111:375–392, February 2018.

[LCVP17] Martin Lesueur, Maria Camila Casadiego, Manolis Veveakis, and Thomas Poulet. Modelling fluid-microstructure interaction on elasto-

visco-plastic digital rocks. *Geomechanics for Energy and the Environment*, 12:1–13, December 2017.

[MBB12] Peyman Mostaghimi, Martin J. Blunt, and Branko Bijeljic. Computations of absolute permeability on micro-ct images. *Mathematical Geosciences*, 45(1):103–125, December 2012.

[MSO21] Seyed Mahdi Mousavi, Saeid Sadeghnejad, and Mehdi Ostadhassan. Evaluation of 3d printed microfluidic networks to study fluid flow in rocks. *Oil & Gas Science and Technology – Revue d'IFP Energies nouvelles*, 76:50, 2021.

[SSG20] Bernhard Schulz, Dirk Sandmann, and Sabine Gilbricht. Sem-based automated mineralogy and its application in geo- and material sciences. *Minerals*, 10(11):1004, November 2020.

[WBAM21] Ying Da Wang, Martin J. Blunt, Ryan T. Armstrong, and Peyman Mostaghimi. Deep learning in pore scale imaging and modeling. *Earth-Science Reviews*, 215:103555, April 2021.

[Wen22] Chester K. Wentworth. A scale of grade and class terms for clastic sediments. *Journal of Geology*, 30(5):377–392, 1922.

[ZL24] Sijmen Zwarts and Martin Lesueur. Predicting the representative elementary volume by determining the evolution law of the convergence cone. *Geomechanics for Energy and the Environment*, 40:100594, December 2024.

Cyclic behavior of geomaterials for energy applications

Luc Simonin, Hadrien Rattez

Institute of Mechanics Materials and Civil Engineering, UCLouvain, Louvain-la-Neuve, Belgium

The transition to sustainable energy systems introduces new challenges for engineering, particularly in the context of cyclic loading experienced by subsurface materials. Offshore wind turbines, geothermal systems, and underground energy storage, all impose repetitive mechanical, thermal, or hydraulic loads on geomaterials, from a few to millions of cycles. This chapter presents a comprehensive overview of the fundamental mechanisms governing cyclic behavior in soils and rocks, and emphasizes their dependence on loading path, frequency, and drainage conditions. A suite of experimental tools, from element testing to centrifuge and large-scale field modeling, is introduced alongside numerical strategies for simulating cyclic behavior using advanced constitutive frameworks. Special attention is given to the modeling limitations at high cycle counts and the importance of using explicit accumulation strategies. Real-world applications, focusing on offshore wind turbine foundations and installation techniques highlight how cyclic loading is a current challenge in both academia and industry. The chapter concludes with a call for deeper integration of material memory, and multiphysical modeling to advance both academic understanding and engineering practice.

1 Introduction

Energy solutions such as offshore wind farms, geothermal systems, or underground hydrogen storage involve an interaction with the ground in the presence of cyclic and multi-physical loading. Cyclic loading refers to the repeated application of stress or strain over time, with possible variations of amplitude, frequency, mean value, and direction. Unlike motonic loading, cyclic loading involves fluctuating forces - such as those induced by waves, wind, machinery, earthquakes, or thermal cycles - that can lead to gradual accumulation of deformation and stress, progressive damage, or pore pressure changes in saturated soils. Understanding the effects of such loading is critical for the design and the long-term performance assessment of energy-related

geo-structures.

The cyclic response of geomaterials can differ significantly depending on the characteristics of the cyclic loading, its duration, and the presence of fluid. Classical cyclic phenomena such as accumulation of plastic strains, pore pressure evolution, stiffness and damping changes are further complicated by the variety of material types, pressure and temperature conditions, but also due to the intrinsic heterogeneity of the tested material. As such, developing adequate laboratory tests and procedures to characterize soil behavior under cyclic loading, as well as constitutive models to predict these phenomena is an essential area of active research in geotechnical engineering.

In this chapter, the fundamentals of cyclic behavior will be further explained, testing procedures and modeling frameworks and strategies presented, and a series of examples related to energy structures will illustrate the challenges of cyclic loading and current areas of research within the geomechanics community.

2 Fundamentals of cyclic behavior

Cyclic loading in geomechanics arises when geomaterials are subjected to time-varying actions, whether mechanical, thermal, or hydraulic. Unlike monotonic loading, which applies a continuously increasing load, cyclic loading involves repeated or fluctuating stress or strain paths, potentially leading to long-term degradation or stabilization of the material. These loadings may originate from environmental conditions (waves, tides, earthquakes, temperature variations), operational cycles (wind turbine rotation, injection/withdrawal of fluids), or installation processes (impact or vibratory driving).

2.1 Vocabulary of cyclic loading

Cyclic loading is characterized and governed by the following parameters:

- Amplitude (A): The magnitude of stress or strain cycles which influences whether the response is plastic or leads to instability.
- Mean value (L_{av}): Non-zero average stress which leads to ratcheting (see 2.2) and directional deformation.
- Number of cycles (N): Critical in determining fatigue life, and varies widely from a few cycles (earthquakes) to tens of millions (offshore wind turbine lifecycle).
- Frequency (f): Influences drainage conditions (with increasing frequency and decreasing drainage length: drained $\rightarrow$ partially-drained $\rightarrow$ undrained) and dynamic response.
- Loading path: uniaxial or multi-directional cyclic loading paths have different implications for material behavior.

- Cyclic type: Regular harmonic loading is often studied in laboratories, while real field loading is pseudo-random, variable in frequency, amplitude and mean value. Capturing this complexity is essential in modern analysis.
- Origin of cycles: The mechanical, thermal, or hydraulic nature of the cycles governs the active coupling mechanisms.

Figure 1 presents on the left a sinusoidal loading characterized by its constant frenquency, mean value and amplitude, and on the right is an example of a pseudo-random loading.

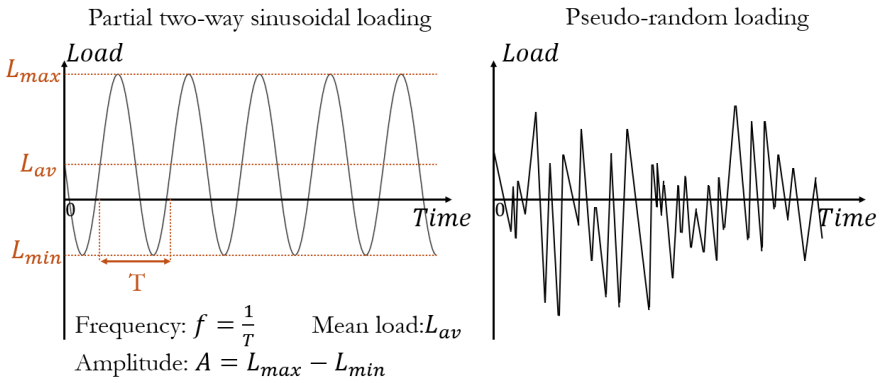

Figure 1: Harmonic cyclic loading (left) and pseudo-random cyclic loading (right).

Cyclic loadings, with reference to Figure 1, can be designated as:

- Two-way loading: $L_{av} = 0$.
- One-way loading: $L_{min} = 0$ (and $L_{av} = L_{max}/2$).
- Partial two-way loading: $L_{av} \neq 0$, $L_{min} < 0$ and $L_{max} > 0$.
- Partial one-way loading: $L_{av} \neq 0$, $L_{min} > 0$ and $L_{max} > 0$.

2.2 Key mechanisms in cyclic behavior

Geomaterials subjected to cyclic loading can exhibit several complex, often competing, phenomena:

- Ratcheting: Under asymmetric or biased cycles (one way, or partial two-way, see Figure 2), materials may accumulate permanent deformation with each cycles, a process referred to as ratcheting. This is common in sands and clays under unidirectional cyclic shearing. This can be observed in element tests on clay[WASB13] and sand [WT16b], small-scale tests [LHB10], or medium-scale

field tests [BMB+20]. Wichtmann lists a number of case studies where structures suffered accumulated settlements [Wic16].

- Changes of strength, stiffness, damping: the evolution of the strength, stiffness and energy dissipation with cycle of the material or, with a broader view, of the geo-structure, depends on the nature of the material. For example in clean sand, it has been observed in laboratory tests on reduced-model of offshore wind turbine foundations that the strength was not affected by cycles, while the secant stiffness increased with cycles and the energy dissipation reduced [Ric19], but some other studies had conflicting conclusions. For clays, cyclic loading impacts the materials by generally reducing their strength and stiffness, primarily due to structural breakdown [LMNS20]. Similarly, in rocks or cemented soils, cyclic loading causes progressive degradation of stiffness and strength. The causes for those materials are microcracks initiation and coalescence that can lead to fatigue failure under mechanical or thermal cycling [Bur63, GFOK18].

  A theoretical illustration of ratcheting, change of stiffness and damping in sand are provided in Figure 2. Intermediate cycles are omitted for clarity: the ratcheting rate diminishes with the number of cycles, the secant stiffness and the damping here respectively increases and decreases (but there are conflicting observations in the literature).

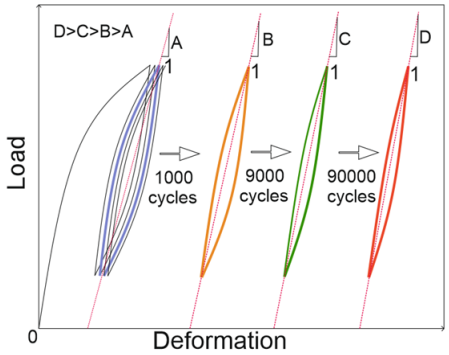

Figure 2: Idealized accumulation of deformation, change of stiffness, and damping with cycles under one-way cycling.

- Pore pressure evolution: In saturated soils, cyclic loading in undrained or partially-drained conditions can lead to a build-up of pore pressure with stress or strain cycles in sand [WT16a, WT16b] and clay [WT18]. The reduction in effective stress as a result of this pore pressure build-up leads to a reduction in shear strength and stiffness. Pushed to the extreme, the mean effective stress, and thus the shear strength, can vanish: this is called liquefaction, where the material behaves as a liquid and very large deformation can thus occur. This is illustrated in Figure 3 for an undrained two-way cyclic stress-controlled test on

medium dense Karlsruhe fine sand [WT16b]: in part (a), depicting deviatoric stress against mean effective stress, the mean effective stress progressively decreases with cycles until it reaches 75kPa where it enters the cyclic mobility phase and its characteristic butterfly-shaped loops in which the soil liquefies; in the matching part (b), depicting deviatoric stress against deviatoric strain, the cycles before cyclic mobility are overlaid in the center of the figure because their strain amplitude is little, but large strains develop during the cyclic mobility phase.

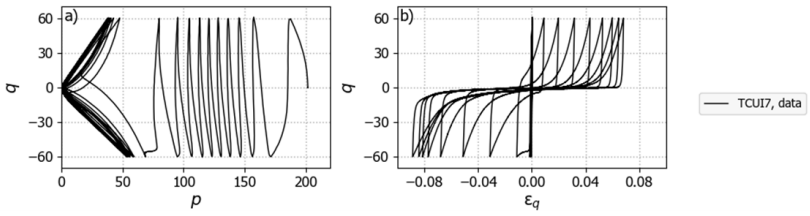

Figure 3: Undrained triaxial test on medium dense Karlsruhe fine sand, data from [WT16b].

- Shakedown: In saturated clays, low-amplitude cyclic loading initially induces plastic strain accumulation, but this accumulation progressively diminishes and eventually stabilizes, leading to a state where no further permanent deformation occurs, see for example [GLW$^+$20].

Cyclic loading of geomaterials is thus governed by a wide combination of interrelated mechanisms, each strongly dependent on the specific loading path and the characteristics of the geomaterial. These phenomena are inherently multiphysical, involving mechanical, hydraulic, and sometimes thermal processes, and their interactions remain only partially understood. Our experimental capabilities allow us to observe some of these mechanisms in isolation or under controlled boundary conditions, but reproducing and generalizing their behavior to full-scale geo-structures remains a challenge. Consequently, constitutive models and design methods are, by necessity, simplifications based on limited experimental evidence. In section 3, we present the current tools available to explore and model these behaviors.

2.3 Difference between soil and rock behaviour

The response of soils and rocks are governed by fundamentally different mechanisms:

- Soils, particularly granular or fine-grained saturated soils, exhibit volume change, pore pressure evolution, and fabric rearrangement. Their cyclic behavior involves an accumulation of shear strain in the average loading direction, as well as a contractive or dilative behavior, that depend on the drainage rate.

- Rocks respond primarily through the initiation and propagation of microcracks, and their failure depends on the amplitude of the loading relative to their tensile or fatigue strength [CC18].

2.4 Material memory and fabric effects

Cyclic loading affects and is affected by the evolving microstructure of geomaterials. Soils tend to realign their particles and contacts, leading to anisotropy and evolving stiffness, while rocks may develop oriented fracture networks. The concept of material memory, the influence of past stress and strain paths on current behavior, is especially relevant in cyclic loading and must be accounted for in both experimental interpretation and constitutive modeling.

3 Testing and modeling cyclic behavior

Understanding and predicting the cyclic response of soils and rocks for energy-related geotechnical systems requires an understanding of the material behavior and of the structure across scales. Element testing must capture essential material behavior at the meso-scale, allowing the exploration of well-defined stress and strain paths. Small- to medium-scale experiments aim to reproduce large-scale structures to recreate and observe large-scale phenomena involving large domains of geomaterial and complex boundary conditions. Numerical models must make use of the element testing in the definition of the material behavior, use the experiments as benchmarks, and be a tool to translate this into reliable predictions for full-scale complex structures subjected to prolonged and variable cyclic loading. This section presents cyclic element testing, physical modeling, constitutive frameworks, and computational strategies for large-scale, often coupled, simulations.

3.1 Element testing: Laboratory Tools for Cyclic Loading

Cyclic element testing provides the basis for quantifying the response of geomaterials under controlled loading paths. The most commonly used devices, illustrated in Figure 4, include:

- Cyclic triaxial testing: This device allows a soil element to be tested under axisymmetric conditions. This test can be controlled with stress or strain, and it allows control of the amplitude, frequency and mean stress, as well as taking into account history of the material with, for example, initial anisotropic stress state. In addition, bender elements can be installed to measure the small strain properties of the specimen. Uniaxial testing (used widely for rocks) is taken into account as a particular case of triaxial tests (no confining pressure).
- True triaxial testing: This triaxial test on cubical samples allows to apply three different principal stresses, instead of the two in classical triaxial testing.

- Cyclic simple shear testing: The sample is laterally sheared under a constant vertical stress, allowing for more realistic stress conditions and the possibility of multi-directional shear loading patterns.
- Torsional shear and hollow cylinder tests: These devices offer multi-axial loading capabilities and control over principal stress rotation, essential for simulating complex load paths such as those in offshore foundations.
- Resonant column test: A cylindrical soil specimen is subjected to torsional vibration and its resonant frequency is found. Shear wave velocity, shear modulus and damping are then calculated. This device allows to determine small strain characteristics of a soil

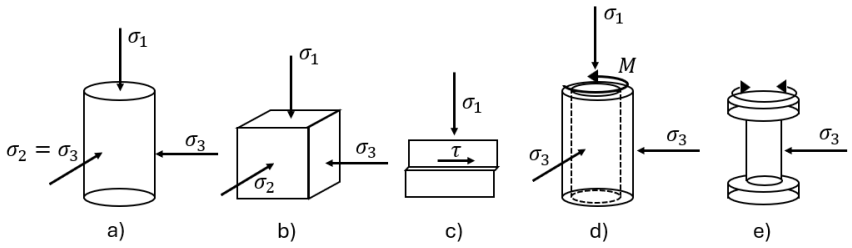

Figure 4: Different element testings: a) Triaxial test, b) True triaxial test, c) Direct shear test, d) Hollow cylinder torsional test, e) Resonant column test

Depending on the geo-structure, these element tests should be conducted at representative pressure levels, take into account site specificity (e.g. partial drainage with inflow by [AA24]), and site history (e.g. effect of pre-shearing and isotropic pre-loading by [IO78]). In addition, the stress and strain paths around the geostructure should be identified to carry out adequate element testing. For example, cyclic stress-controlled tests will be interesting for lateral loading of offshore wind turbine foundation where the loading is defined by the forces applied by the waves and the wind (see4.1, while cyclic strain-controlled tests might be more interesting for vibratory installation of piles (see 4.2) where the amplitude of the shearing at the pile-soil interface is the focus.

Large database of cyclic triaxial tests are available for sand from [WT16b, WT16a, DRM$^+$23], and for clay from [WT18, DRMN22]. These database are available from the SoilModels website [Soi].

3.2 Reduced-Scale Modeling

While element testing is indispensable for characterizing the fundamental cyclic behavior of geomaterials, it does not capture the complex interactions between soils, rocks, and geotechnical structures subjected to cyclic loading. Conversely, full-scale

field data, whether from instrumented structures, operational monitoring, or post-event observations, provides the most realistic insight into system behavior. However, such data is often unavailable for novel or yet-to-be-constructed systems, or may be inaccessible due to proprietary restrictions or lack of instrumentation and observation. Large-scale field experiments, though highly valuable, are logistically demanding and economically prohibitive. In this context, reduced-scale physical modeling serves as a critical intermediary, offering practical and controlled means to investigate soil–structure interaction under representative cyclic conditions. It remains a cornerstone of experimental geotechnical research, particularly for validating numerical models and informing design methodologies where full-scale data is lacking. Challenges in reduced-scale modeling include:

- Boundary conditions: Proper simulation of in-situ stress states, drainage conditions, and load transmission is critical. For example, rigid boundaries can affect energy dissipation in dynamic testing.
- Scaling laws: When thermal, hydraulic, or mechanical effects are coupled, scaling becomes non-trivial. Centrifuge modeling addresses gravity-induced stress representativeness (see the chapter "Physical model experiments in geomechanics for the energy transition").
- Material representativeness: Use of reconstituted samples, scaling of particle size, or substitute materials may distort cyclic response.

Despite limitations, reduced-scale models have been successfully used to study cyclic loading of offshore wind turbine monopile foundations by, for example, [Aba15], providing important validation for numerical models.

3.3 Constitutive Modeling of Cyclic Behavior

In parallel with experimental approaches, numerical modeling plays a central role in predicting the response of geotechnical structures under cyclic loading, particularly in applications where direct testing is not feasible or where parametric exploration is required. However, accurately representing the behavior of soils and rocks under cyclic loading is inherently challenging. It demands constitutive models that can reproduce the key features of cyclic response (see 2.2). These phenomena are often strongly influenced by loading history, amplitude, frequency, and drainage conditions, requiring models that incorporate memory effects, stress-path dependency, and in many cases, multi-physical couplings.

In soil mechanics, no consensus on a framework to model cyclic loading has been reached, but the following classes of models are used and under constant development:

- Original contributions in the "classical" elasto-plasticy with models by [MP83, PZL85, OYS$^+$94, IMRC05] for sand, for clay by [RB68, WD93], or [PW99] for sand and clay.
- Bounding surface [DH80] models, such as the SANISAND family of mod-

els [DM04, PDP20, RTD25] or models by [Hir87, WDS90, CD21] for sand, [DMP06, RTP16] for clay, and [BZ19] for clay and silt. Bounding surface plasticity allows plastic strains to develop even within the yield surface, by defining a bounding surface that encloses all admissible stress states. The stress point maps to an image point on this surface via a mapping rule, and the degree of plasticity depends on the distance between the two, thus capturing smooth transitions between elastic, plastic, and cyclic behaviors.

- Hypoplastic [KH05] models, such as [WB94, GTTK20] for sand, [Ma4, TT20, MTB$^+$24] for clay, or [TT23] for silt. Hypoplasticity is a constitutive framework that directly relates stress rate to the current stress and strain rate, without separating elastic and plastic components. It captures the inherently nonlinear, pressure-sensitive, and rate-independent behavior of soils through tensorial equations. Although standard hypoplastic models reproduce hysteresis and large strain loops, they lack memory effect, limiting their accuracy under small cyclic paths, but extensions such as intergranular strain have been developed to address this.
- Multi-surface plasticity originally developed by [Mr7, Iwa67] and adapted to soil mechanics by Prévost [Pr8], with models for sand by [Sim23]. Multi-surface plasticity models cyclic behavior by defining multiple yield surfaces in stress space, each governing a portion of the plastic response. As loading progresses, surfaces are activated sequentially, enabling the capture of phenomena such as kinematic hardening, hysteresis, and the Bauschinger effect. This framework offers a relatively simple yet effective way to simulate complex cyclic responses, especially when surface properties are systematically distributed.

Another original consitutive modelling approach is barodesy [KOL15].

Interested readers can refer to the ALERT doctoral school [MTH21].

3.4 Modeling strategies for geo-structures

Advanced numerical approaches, such as finite element (FEM), discrete element (DEM and FEM–DEM), or material-point (MPM) methods, allow detailed simulation of soil–structure interaction under cyclic loading, granted that adequate constitutive models are used. Also, the discrete element method (DEM, or coupled with FEM: FEMxDEM) can be an effective tool to address cyclic loading at the micro-level, and the material-point method (MPM) or Coupled-Eulerian–Lagrangian (CEL) schemes are potent tools to study large deformations. While powerful, these methods are generally limited to simulating a relatively small number of cycles. This is sufficient for seismic or some foundation installation analyses but inadequate for applications subjected to high-cycle loading (e.g., offshore wind turbine foundations life cycle, where millions of cycles are expected). For such large number of cycles, alternatives to model the lifetime of the geo-structure have to be found. Taking the example of offshore wind turbine foundations, modeling strategies can consist in:

- using empirical relationship to predict the behavior of the structure at a macro-level, such as in [LHB10].
- simplifying the foundation to a macro-element or one dimensional system to enable the simulations of many cycles at a lower calculation cost. This can take the form of HARM by [Aba15] or Redwin by [PGEJ18], or their combination [AP25].
- using cyclic contour diagrams [And15] to interpret the response under cyclic loading of a structure by interpreting the cyclic loading into equivalent packets of constant amplitude cycles for which the response is directly inferred from a cyclic contour diagram.
- using advanced finite element analysis for characteristic cycles, and then extrapolating the behavior for large number of cycles. For example, the high-cycle accumulation (HCA) model by [NWT05] uses full-cycle simulation for the first few cycles to capture key amplitudes, then applies an explicit accumulation rule for large cycle counts.

Coupled thermo-hydro-mechanical (THM) FEM or finite difference models have been specifically developed and utilized to simulate the impact of cyclic heat transfer and water flow on the mechanical behavior of geomaterials mostly in the context of energy piles and more recently for Hydrogen storage. For energy piles, models have explicitly considered cyclic effects, with plastic deformations being captured through the constitutive models of the soil or the soil-pile interface [LMNS20].

4 Examples for offshore wind turbines

4.1 Cyclic Loading During the Lifetime of Offshore Wind Turbine Foundations

Offshore wind turbine (OWT) foundations are subjected to millions of loading cycles over their operational lifespan due to the combined effects of wind, waves, rotor-nacelle-tower dynamics, and operational events such as installation and decommissioning (discussed in the following subsection). These cycles vary in amplitude and frequency, leading to complex loading paths that affect both the structural and geotechnical response of the foundation system.

Several foundation types exist depending on water depth and site conditions, including fixed-bottom (e.g., monopiles, jackets, gravity-based, suction caissons) and floating solutions, each with different cyclic loading profiles. For instance, monopiles are primarily subjected to lateral cyclic loading, jackets to axial loads in their different piles, and floating systems to combined loading on anchors, including shared anchoring systems. These foundation types are detailed in the dedicated chapter on offshore wind systems.

This subsection focuses on the most commonly used solution for fixed-bottom off-

shore wind in intermediate water depths: the monopile foundation. Monopiles are large-diameter hollow steel piles driven into the seabed, typically with low length-to-diameter (L/D) ratios, often behaving more rigidly compared to the slender piles used in traditional offshore oil and gas platforms.

Historically, the design of offshore piles relied on the $p - y$ method, wherein the monopile is modeled as a one-dimensional beam discretized into finite elements, with the soil resistance represented by non-linear springs relating lateral soil pressure (p) to lateral displacement (y). Early $p - y$ curve formulations [Mat70] formed the basis for industry standards, including those issued by the American Petroleum Institute [Ins07]. These models assumed slender, flexible piles and therefore often underestimate the influence of base resistance and side friction for the stiffer, shorter monopiles used in wind energy applications.

To address these limitations, the PISA (Pile Soil Analysis) joint industry project [BHB$^+$20] introduced a more rigorous approach using advanced 3D finite element analysis to derive site-specific and geometry-consistent soil reaction curves. The PISA framework improved monotonic design fidelity and led to optimized foundation sizing. The progressive improvement of monopile geotechnical design over the last 20 years is further illustrated in [MWT25], who reported a 32% reduction in steel tonnage for a typical monopile due to improved geotechnical characterization and design procedures.

While these advances have matured the design under monotonic loading, they have shifted the design focus toward cyclic loading, where existing standards, such as [Ver14], remain limited. For example, cyclic degradation is often treated via a simplistic reduction of ultimate strength (see Figure 5), ignoring ratcheting, stiffness and damping evolution, which are key mechanisms that can alter foundation performance over time. These mechanisms are particularly important for dynamic systems such as OWTs, where shifts in foundation stiffness may lead to changes in the natural frequency of the structure, potentially moving it closer to excitation frequencies from waves, wind, or rotor-blade harmonics, thus increasing the risk of resonance. Cyclic loading is central in a number of current joint-industry projects such as PICASO [BBB$^+$25] or MIDAS-CLAY [KKC$^+$25]. These projects make use of all the available tools presented in section 3:

- element testing to develop adequate constitutive models that feed into numerical models,
- numerical models that are bench-marked against medium-scale field testing and small-scale laboratory testing,
- numerical models that are then used to model more complex full-scale scenarios,
- numerical strategies and engineering processes are developed to address the cyclic loading of monopiles in order for the industry to optimize their design.

Recent research has proposed several advanced modeling strategies to overcome these limitations, as outlined in the previous section 3.4. Explicit cyclic modeling strate-

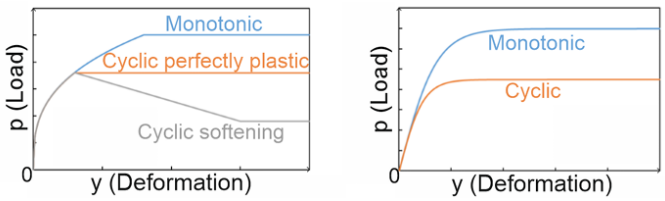

Figure 5: Historical simplified consideration of cyclic loading for clay (left) and sand (right), to be compared to Figure 2.

gies are particularly promising for long-term applications, as they enable extrapolation of long-term response from selected representative loading scenarios. For example, while it remains computationally infeasible to simulate millions of load cycles directly, one can model the most critical storm events and then use extrapolation techniques, to infer accumulated effects from the smaller, less impactful cyclic loads. This approach helps mitigate errors due to constitutive model drift or numerical artifacts that may accumulate over long simulations.

4.2 Cyclic Loading During Installation and Decommissioning of Wind Turbine Foundations

As discussed in Section 2.2 of the "Geotechnical Challenges for Offshore Wind Turbine Foundations" chapter, the conventional installation method for monopiles, impact hammering, is increasingly challenged by multiple factors. These include regulatory restrictions on underwater noise emissions, the risk of uncontrolled pile penetration (pile run), and the technical difficulty of scaling up impact hammer systems to accommodate XXL monopiles.

Impact driving is, by nature, a cyclic loading process. Typically operating at a rate of approximately 40 blows per minute, each hammer strike generates large displacements, stress redistribution around the pile, and significant pore pressure fluctuations. Although this method has a long history of practical use, predictive driving models remain relatively crude, and the accurate simulation of this process using numerical methods is an ongoing research challenge. These models are critical not only for improving driveability predictions, but also for assessing the effect of installation-induced changes on the subsequent lateral response of the pile.

An emerging area of research for offshore wind is vibratory pile driving, in which a vibratory hammer applies vertical vibrations, typically in the 10–40 Hz range, via a system comprising counter-rotating eccentric masses attached to the pile head. This technique, with a long onshore history for sheet-piles and smaller piles, is generally quieter and potentially faster than impact hammering. However, existing driving models such as GRL-WEAP and HyperVIB [HW17] were not developed with offshore or large-diameter monopile applications in mind, leading to uncertainty in their predic-

tive capabilities for these cases.

In addition to modeling driveability, a central question concerns how vibratory installation influences the long-term lateral behavior of monopiles compared to those driven by impact. During vibratory driving, vertical pile oscillations appear to reduce skin friction along the shaft, but the underlying mechanisms remain poorly understood. Significant research efforts are therefore underway, employing a range of experimental and numerical approaches discussed throughout this chapter, including:

- Medium- and laboratory-scale field testing within the SIMOX project [PdSPE+23].
- Small-scale centrifuge modeling [MBB+25, SROV+25].
- Discrete Element Method (DEM) simulations [FBC+].
- Coupled Euler–Lagrangian modeling approaches [SMSW21].
- Element testing under cyclic undrained strain-controlled conditions [WT16a], which provide insight into material response but require improved understanding of vibration transmission mechanisms to connect to full-scale pile behavior.

Looking ahead, decommissioning will become an increasingly relevant challenge as the earliest offshore wind farms approach the end of their design life. Vibratory driving is considered a promising technique for pile extraction, particularly for retrieving the embedded portions of monopiles. Research in this area is gaining momentum, as efficient, low-impact decommissioning will be essential for the lifecycle sustainability of offshore wind infrastructure.

5 Conclusions and Perspectives

Cyclic loading is a defining challenge in the geotechnical design of energy-related infrastructures. Across different energy sectors, geomaterials are subjected to highly variable and repeated loadings that can induce complex mechanical responses including strain accumulation, stiffness degradation, pore pressure buildup, and, in extreme cases, liquefaction or failure. These responses are controlled not only by the amplitude and frequency of the loading, but also by the specific nature of the geomaterial, the drainage conditions, and thermal or hydraulic couplings.

This chapter has outlined the wide range of physical phenomena observed under cyclic loading and the corresponding tools available to investigate and model them. From laboratory-scale element testing to physical modeling in geotechnical centrifuges and advanced finite element simulations, a multi-scale, multi-disciplinary approach is necessary to make progress. Special emphasis was placed on the selection and development of constitutive models that can capture key cyclic features and the modeling strategies suitable for either low-cycle (e.g., seismic or installation events) or high-cycle (e.g., operational loading of offshore wind turbines) regimes.

Looking forward, a number of research directions are emerging. These include:

- Real-time field monitoring of cyclic performance using distributed sensors and fiber optics.
- Development of digital twins integrating sensor feedback with advanced numerical modeling.
- AI-driven forecasting tools that can assimilate large datasets of cyclic loading to anticipate long-term deformations or failure.
- Cross-disciplinary approaches incorporating materials science, mechanics, and data science to develop next-generation predictive models.

In conclusion, cyclic loading must be approached as a multiphysical, multiscale problem that connects laboratory insights to full-scale, real-world performance. Its mastery is essential for the long-term reliability, safety, and sustainability of energy transition infrastructure.

References

[AA24] Orestis Adamidis and Ioannis Anastasopoulos. Cyclic liquefaction resistance of sand under a constant inflow rate. *Géotechnique*, 74(10):1019–1032, 2024.

[Aba15] C.N. Abadie. *Cyclic lateral loading of monopile foundations in cohesionless soils*. PhD thesis, University of Oxford, 2015.

[And15] K. H. Andersen. Cyclic soil parameters for offshore foundation design. In *Proceedings of the 3rd International Symposium on Frontiers in Offshore Geotechnics (ISFOG). Oslo, Norway*, 2015.

[AP25] C.N. Abadie and A.M. Page. Clap - simplified model for multidirectional cyclic loading on offshore piles. In *Proceedings of the 5TH INTERNATIONAL SYMPOSIUM ON FRONTIERS IN OFFSHORE GEOTECHNICS Nantes, France — June 9-13 2025*, 2025.

[BBB+25] Byron W. Byrne, Roisin M. Buckley, H.J. Burd, J. Crispin, G.T. Houlsby, I. Kamas, R. Keane, S. Malhotra, S. Martin, V. Nardelli, Z.H. Qiu, M. Rasmussen, A. Shonberg, L.E.J. Simonin, V.S. Cunha, E. Vaitkune, K.Z. Wen, and K-.W. Wu. Picaso: Cyclic loading of wind turbine monopiles. In *Proceedings of the 5th International Symposium on Frontiers in Offshore Geotechnics (ISFOG2025)*, 2025.

[BHB+20] Byron W. Byrne, Guy T. Houlsby, Harvey J. Burd, Kenneth G. Gavin, David J. P. Igoe, Richard J. Jardine, Christopher M. Martin, Ross A. McAdam, David M. Potts, David M. G. Taborda, and Lidija Zdravković. Pisa design model for monopiles for offshore wind turbines: application to a stiff glacial clay till. *Géotechnique*, 70(11):1030–1047, 2020.

[BMB+20] Byron W. Byrne, Ross A. McAdam, William J.A.P. Beuckelaers, Harvey J. Burd, Kenneth Gavin, Guy T. Houlsby, David John Paul Igoe, Richard Jardine, and Martin Chris M. Cyclic laterally loaded medium scale field pile testing for the pisa project. In *4th International Symposium on Frontiers in Offshore Geotechnics (ISFOG 2020 in 2022)*, pages 1323–1332, 2020.

[Bur63] N.T. Burdine. Rock failure under dynamic loading conditions. *Society of Petroleum Engineers Journal*, 3(01):1–8, 03 1963.

[BZ19] Ross W. Boulanger and Katerina Ziotopoulou. A constitutive model for clays and plastic silts in plane-strain earthquake engineering applications. *Soil Dynamics and Earthquake Engineering*, 127:105832, 2019.

[CC18] Benjamin Cerfontaine and Frédéric Collin. Cyclic and fatigue behaviour of rock materials: review, interpretation and research perspectives. *Rock mechanics and rock engineering*, 51(2):391–414, 2018.

[CD21] Z. Cheng and C. Detournay. Formulation, validation and application of a practice-oriented two-surface plasticity sand model. *Computers and Geotechnics*, 132, 2021.

[DH80] Y.F. Dafalias and L.R. Herrmann. A bounding surface soil plasticity model, 1980.

[DM04] Y. F. Dafalias and M. T. Manzari. Simple plasticity sand model accounting for fabric change effects. *Journal of Engineering Mechanics*, 130:622–634, 2004.

[DMP06] Yannis F. Dafalias, Majid T. Manzari, and Achilleas G. Papadimitriou. Saniclay: simple anisotropic clay plasticity model. *International Journal for Numerical and Analytical Methods in Geomechanics*, 30(12):1231–1257, 2006.

[DRM+23] J. Duque, J. Roháč, D. Mašín, J. Najser, and J. Opršal. The influence of cyclic preloadings on cyclic response of zbraslav sand. *Soil Dynamics and Earthquake Engineering*, 166:107720, 2023.

[DRMN22] J. Duque, J. Roháč, D. Mašín, and J. Njser. Experimental investigation on malaysian kaolin under monotonic and cyclic loading: inspection of undrained miner's rule and drained cyclic preloading. *Acta Geotechnica*, 17:4953–4975, 2022.

[FBC+] L.Q. Fang, M.J. Brown, M.O. Ciantia, M. Previtali, and W. Wang. In *Proceedings of the 5th International Sympozium on Frontiers in Offshore Geotechnics ISFOG2025), title = Optimisation of tensile capacity of vibro-installed floating offshore anchor piles using DEM simulation, year = 2025.*

[GFOK18] Rashid Geranmayeh Vaneghi, Behnam Ferdosi, Achola D. Okoth, and Barnabas Kuek. Strength degradation of sandstone and granodiorite under uniaxial cyclic loading. *Journal of Rock Mechanics and Geotechnical Engineering*, 10(1):117–126, 2018.

[GLW+20] Lin Guo, Liguo Liu, Jun Wang, Hongxu Jin, and Yuan Fang. Long term cyclic behavior of saturated soft clay under different drainage conditions. *Soil Dynamics and Earthquake Engineering*, 139:106362, 2020.

[GTTK20] Carlos Eduardo Grandas Tavera, Theodoros Triantafyllidis, and Lukas Knittel. A constitutive model with a historiotropic yield surface for sands. In Theodoros Triantafyllidis, editor, *Recent Developments of Soil Mechanics and Geotechnics in Theory and Practice*, pages 13–43, Cham, 2020. Springer International Publishing.

[Hir87] H. Hirai. An elastoplastic constitutive model for cyclic behaviour of sands. *Int. J. Numer. Anal. Meth. Geomech.*, 11:503–520, 1987.

[HW17] A. Holeyman and V. Whenham. Critical review of the hypervib1 model to assess pile vibro-drivability. *Geotechnical and Geological Engineering*, 35:1933–1951, 2017.

[IMRC05] R. Imam, N. Morgenstern, P. Robertson, and D. Chan. A critical-state constitutive model for liquefiable sand. *Canadian Geotechnical Journal*, 42:830–855, 2005.

[Ins07] API (American Petroleum Institute). Api rp2a: Recommended practice for planning, designing and constructing fixed offshore platforms., 2007.

[IO78] Kenji Ishihara and Shigeru Okada. Effects of stress history on cyclic behavior of sand. *Soils and Foundations*, 18(4):31–45, 1978.

[Iwa67] W. D. Iwan. On a class of models for the yielding behavior of continuous and composite systems. *Journal of Applied Mechanics*, 34(3):612–617, 09 1967.

[KH05] D. Kolymbas and I. Herle. *Hypoplasticity as a Constitutive Framework for Granular Soils*, pages 257–289. 2005.

[KKC+25] E. Kementzetzidis, M. Konstantinou, C. Cengiz, R. Zwaan, A. Sharma, A.S.K Elkadi, F. Pisano, H. Wang, H.P. Jostad, G. Christopoulos, and D. Mohapatra. Centrifuge testing and numerical modelling of cyclically loaded monopiles in clay: Setup and early findings of the midasclay project. In *Proceedings of the 5th International Symposium on Frontiers in Offshore Geotechnics (ISFOG2025)*, 2025.

[KOL15] D. KOLYMBAS. Introduction to barodesy. *Géotechnique*, 65(1):52–65, 2015.

[LHB10] Christian Leblanc, Guy T. Houlsby, and Byron W. Byrne. Response of stiff piles in sand to long-term cyclic lateral loading. *Géotechnique*, 60(2):79–90, 2010.

[LMNS20] Fleur Loveridge, John S McCartney, Guillermo A Narsilio, and Marcelo Sanchez. Energy geostructures: a review of analysis approaches, in situ testing and model scale experiments. *Geomechanics for Energy and the Environment*, 22:100173, 2020.

[Mat70] *Correlation for Design of Laterally Loaded Piles in Soft Clay*, volume Offshore Technology Conference of *OTC Offshore Technology Conference*, 04 1970.

[Ma4] D. Mašín. Clay hypoplasticity model including stiffness anisotropy. *Géotechnique*, 64(3):232–238, 2014.

[MBB+25] J. H. Mazutti, B. Bienen, M. F. Bransby, M. F. Randolph, and G. Wager. Development of a mini vibro-driver for pile testing in the centrifuge. *International Journal of Physical Modelling in Geotechnics*, 25(1):34–48, 01 2025.

[MP83] Z. Mróz and S. Pietruszczak. A constitutive model for sand with anisotropic hardening rule. *Int. J. Numer. Anal. Meth. Geomech.*, 7:305–320, 1983.

[Mr7] Z. Mróz. On the description of anisotropic workhardening. *Journal of the Mechanics and Physics of Solids*, 15(3):163–175, 1967.

[MTB+24] G. Medicus, M. Tafili, M. Bode, W. Fellin, and T. Wichtmann. Clay hypoplasticity coupled with small-strain approaches for complex cyclic loading. *Acta Geotechnica*, 19:631–650, 2024.

[MTH21] David Mašín, Claudio Tamagnini, and Ivo Herle. *ALERT Doctoral School 2021, Constitutive Modelling in Geomaterials*. 10 2021.

[MWT25] A. Muir Wood and C.L. Thilsted. Evolving offshore wind: Technical advances and commercial realities. In *Proceedings of the 5TH INTERNATIONAL SYMPOSIUM ON FRONTIERS IN OFFSHORE GEOTECHNICS Nantes, France — June 9-13 2025*, 2025.

[NWT05] A. Niemunis, T. Wichtmann, and Th. Triantafyllidis. A high-cycle accumulation model for sand. *Computers and Geotechnics*, 32(4):245–263, 2005.

[OYS+94] F. Oka, A. Yashima, T. Shibata, M. Kato, and R. Uzuoka. Fem-fdm coupled liquefaction analysis of a porous soil using an elasto-plastic model. *Applied Scientific Research*, 52:209–245, 1994.

[PDP20] A.L. Petalas, Y.F. Dafalias, and A.G. Papadimitriou. Sanisand-f: Sand constitutive model with evolving fabric anisotropy. *International Journal of Solids and Structures*, 188-189:12–31, 2020.

[PdSPE+23] A. Peccin da Silva, M. Post, A. S. Elkadi, E. Kementzetzidis, and F. Pisanò. A laboratory study of the effect of installation parameters on the lateral behaviour of monopiles in sand. In *Proceedings of the Symposium on Energy Geotechnics 2023, Delft, The Netherlands*, 2023.

[PGEJ18] Ana M. Page, Gustav Grimstad, Gudmund Reidar Eiksund, and Hans Petter Jostad. A macro-element pile foundation model for integrated analyses of monopile-based offshore wind turbines. *Ocean Engineering*, 167:23–35, 2018.

[Pr8] Jean-Hervé Prévost. Anisotropic undrained stress-strain behavior of clays. *Journal of the Geotechnical Engineering Division*, 104(8):1075–1090, 1978.

[PW99] J.M. Pestana and A.J. Whittle. Formulation of a unified constitutive model for clays and sands. *Int. J. Numer. Anal. Meth. Geomech.*, 23:1215–1243, 1999.

[PZL85] M. Pastor, O.C. Zienkiewicz, and K.H. Leung. Simple model for transient soil loading in earthquake analysis. ii. non-associative models for sands. *International Journal for Numerical and Analytical Methods in Geomechanics*, 9:477–498, 1985.

[RB68] K. Roscoe and J. B. Burland. On the generalized stress-strain behaviour of wet clay. In *J. Heyman, F. Leckie (Eds.), Engineering plasticity, Cambridge University Press, Cambridge*, pages 535–609, 1968.

[Ric19] I Richards. *Monopile foundations under complex cyclic lateral loading*. PhD thesis, University of Oxford, 2019.

[RTD25] Andrés Reyes, Mahdi Taiebat, and Yannis F. Dafalias. Modification of sanisand-msf model for simulation of undrained cyclic shearing under nonzero mean shear stress. *Journal of Geotechnical and Geoenvironmental Engineering*, 151(7):04025051, 2025.

[RTP16] Mohammad Rezania, Mahdi Taiebat, and Elisa Poletti. A viscoplastic saniclay model for natural soft soils. *Computers and Geotechnics*, 73:128–141, 2016.

[Sim23] L.E.J. Simonin. *Development of an effective stress model for sand under cyclic loading in the hyperplastic framework*. PhD thesis, University of Oxford, 2023.

[SMSW21] P. Staubach, J. Machaček, J. Skowronek, and T. Wichtmann. Vibratory pile driving in water-saturated sand: Back-analysis of model tests using a hydro-mechanically coupled cel method. *Soils and Foundations*, 61(1):144–159, 2021.

[Soi] Soilmodels website, accessible from soilmodels.com.

[SROV+25] L.E.J Simonin, H. Rattez, W.F. Ovalle Villamil, M.A. Cabrera, G. Anoyatis, and S. Francois. Influence of vibro-driver frequency on pile penetration in dry sand in a geotechnical centrifuge. In *Proceedings of the 5th International Symposium on Frontiers in Offshore Geotechnics (ISFOG2025)*, 2025.

[TT20] M. Tafili and T. Triantafyllidis. Avisa: anisotropic visco-isa model and its performance at cyclic loading. *Acta Geotechnica*, 15:2395–2413, 2020.

[TT23] Merita Tafili and Theodoros Triantafyllidis. Cyclic and monotonic response of silts and clays: experimental analysis and constitutive modelling. *European Journal of Environmental and Civil Engineering*, 27(6):2303–2312, 2023.

[Ver14] Det Norske Veritas. Adnv-os-j101: Design of offshore wind turbine structures may 2014., 2014.

[WASB13] T. Wichtmann, K.H. Andersen, M.A. Sjursen, and T. Berre. Cyclic tests on high-quality undisturbed block samples of soft marine norwegian clay. *Canadian Geotechnical Journal*, 50(4):400–412, 2013.

[WB94] Wei Wu and Erich Bauer. A simple hypoplastic constitutive model for sand. *International Journal for Numerical and Analytical Methods in Geomechanics*, 18(12):833–862, 1994.

[WD93] G. W. Wathugala and C. S. Desai. Constitutive model for cyclic behavior of clays. i: Theory. *Journal of Geotechnical Engineering*, 119(4):714–729, 1993.

[WDS90] Z. Wang, Y. Dafalias, and C. Shen. Bounding surface hypoplasticity model for sand. *Journal of Engineering Mechanics*, 116:983–1001, 1990.

[Wic16] Torsten Wichtmann. *Soil behaviour under cyclic loading-experimental observations, constitutive description and applications*. Th. Triantafyllidis, 2016.

[WT16a] Torsten Wichtmann and Theodoros Triantafyllidis. An experimental database for the development, calibration and verification of constitutive models for sand with focus to cyclic loading: part ii—tests with strain cycles and combined loading. *Acta Geotechnica*, 11(4):763–774, 2016.

[WT16b] Torsten Wichtmann and Theodoros Triantafyllidis. An experimental database for the development, calibration and verification of constitutive models for sand with focus to cyclic loading: part i—tests with monotonic loading and stress cycles. *Acta Geotechnica*, 11(4):739–761, 2016.

[WT18] Torsten Wichtmann and Theodoros Triantafyllidis. Monotonic and cyclic tests on kaolin: a database for the development, calibration and verification of constitutive models for cohesive soils with focus to cyclic loading. *Acta Geotechnica*, 13:1103–1128, 2018.

©ALERT Geomaterials
Laboratoire 3SR / Bâtiment Galilée
CS 40700
38 058 Grenoble cedex 9
France

Fon: +33 (0) 456 528 621
Fax: +33 (0) 476 827 043
president@alertgeomaterials.eu
https://alertgeomaterials.eu

ALERT Doctoral School 2025

The Role of Geomechanics in the Energy Transition

Editors: A. Dieudonné, M. Lesueur, J. Pereira, H. Rattez & M. Veveakis